CENTRO DE INVESTIGACIONES EN ÓPTICA, A.C.

POLARIMETRY OF IMAGES USING CLASSICAL ENTANGLEMENT OF LIGHT

(Final version. Changes suggested by advisors are included)

MAESTRÍA EN CIENCIAS (ÓPTICA)
(MASTER OF SCIENCE (OPTICS))

Adviser: **Dr. Rafael Espinosa Luna**

Student: **BSc. Phys. Jacqueline Isamar Muro Ríos**

July, 2017
León, Guanajuato, México

POLARIMETRY OF IMAGES USING CLASSICAL ENTANGLEMENT OF LIGHT

by

Jacqueline Isamar Muro Ríos

Submitted in partial fulfillment of the requirements for the degree of
Master in Science (Optics)

Reviewers:

Dr. Rafael Espinosa Luna
(*Adviser*)

Dr. Moisés Cywiak Garbarcewicz
(*Internal Synodal*)

Dr. Gelacio Atondo Rubio
(*External Synodal*)

CENTRO DE INVESTIGACIONES EN ÓPTICA, A.C.

July 2017

To my family, friends and all the people who have supported me at different aspects and stages in my life. I hope someday I can give back some of the much that I have been given.

Set your sights high, the higher the better.
Expect the most wonderful things to happen,
not in the future but right now.
Realize that nothing is too good.
Allow absolutely nothing to hamper you
or hold you up in any way.
Eileen Caddy

Acknowledgments

Abstract

Act as if what you do makes a difference. It does.

William James

The study of the polarization of light nowadays is conceived within two main branches: conventional and unconventional polarization. Conventional polarization is the term assigned to the spatially homogeneous amplitude and phase associated to the electric field distributions. On the other hand, the spatially non-homogeneous amplitude and phase electric field distributions are termed as unconventional polarization. From all the possible unconventional polarization states, there exist a very special kind of states which can not be expressed as a single product of a spatial and a polarization distribution. Such kind of polarization states are nonseparable or entangled, because the electric field can be represented only by the use of two coordinate-independent Jones vectors and two independent scalar fields. This type of entanglement is denoted as classical entanglement, because occurs in a single light beam (intra-system), contrary to the case of quantum entanglement, which occurs between two separated photons (inter-system entanglement). Two of the main unconventional polarization states, radial and azimuthal, are classically entangled.

The Mueller matrix represents the linear responses associated to optical materials and it contains all the available polarimetric information. Usually, it can be determined by using at least 4 incident conventional polarization states. In this work, a single incident polarization is employed: an azimuthal polarization state is generated and used as a classical entangled beam for the experimental determination of the Mueller matrix associated to birefringent, transparent samples. The procedure developed here shows the way the entangled degrees of freedom of the beam (the spatial or mode distributions, represented as Hermite-Gauss and Laguerre-Gauss modes, and the polarization states) can be analyzed independently. Based in two previous works (Töppel et al. (2014) and Aguilar (2017)) an experimental setup is proposed and improved. The experimental setup consists of a complex set of modules: a polarization state generator, an unconventional or entangled polarization state generator, the sample under study, a mode converter, a modified Mach-Zehnder interferometer, a conventional polarization state analyzer, and a spatially-resolved detection system. An analysis of each module is realized, in order to test the optical alignment and expected functionality.

The Mueller matrices associated to air, to a half-wave plate and to a quarter-wave plate retarders, are determined by applying the relationships reported by Töppel et al. (2014) and the relationships obtained by the ideal polarimetric arrangement (IPA), reported by Atondo-Rubio et al. (2005).

Results are reported by using both, images and the spatial average symmetry (SAS), which show to be consistent with the expected responses. To our knowledge, this is the first study associated to the experimental determination of the Mueller matrix of transparent objects under open space conditions, using the classical entangled azimuthal polarization state as a single incident polarization state.

Table of Contents

Index of Figures

Chapter 1

Introduction

There's a way to do it better – find it.

Thomas A. Edison

SUMMARY: In this Chapter, we give a brief introduction to the key concept on which this thesis work is based. We expose the general and particular objectives that we have proposed and finally, we give an overview on the organization of this thesis document.

1.1. Introduction

Unconventional polarization is a term used to refer to a very special kind of beams that are characterized by having non homogeneous distributions of intensity and phase along the cross section of the beam (Zhan, 2009). These non homogeneous distributions lead to the need of using 2 degrees of freedom in order to be able to describe them: One for the spatial distribution, which we will call "the mode" and can be described through a Hermite-Gauss, Laguerre-Gauss or any other function that satisfies the wave equation; and the other used to deal with the polarization of the mode, which can be horizontal, vertical, at $\pm 45°$, circular right handed, circular left handed or any other of the known "conventional" polarization states. We refer to them as beams with unconventional polarization because we have different electric field vectors (associated to different conventional polarizations) depending on which part of the beam cross section we are. Furthermore, it is said that these beams are "classically entangled" because "one needs two coordinate independent Jones vectors and two independent scalar fields (modes) to represent the electric field", as stated by Töppel et al. (2014). This classical entanglement fundamentally differs from the quantum entanglement because it occurs between two degrees of freedom in the same beam (intra-system entanglement) and not between two separate beams (inter-system entanglement) as is the case for quantum entanglement. This inherent relationship between modes and polarization opens the possibility to many applications for which the entangled feature of the beam can be exploited and for which the use of the non locality feature can be omitted (Töppel et al., 2014).

1.2. Background

Unconventional polarization is a new field which has generated an increasing scientific and technological interest around the world. According to Zhan (2009), the early works in this topic

started with the studies of optical imaging such as optimal concentration of electromagnetic radiation in the focal region, in 1997. Ever since, there have been several proposals that range among the methods and techniques to generate, manipulate, detect them and also their potential application to high resolution imaging, plasmonic, and nanoparticle manipulation (Zhan, 2014). However, to the best of our knowledge, none experimental work on the use of unconventional polarization for determining the Mueller matrix of a sample has been reported, being the only existing one of purely theoretical character (Töppel et al., 2014).

1.3.   Justification

The peculiar characteristics of the unconventional polarization have led to propose its implementation in polarimetric arrangements with the objective of presenting a measurement scheme faster and alternative to the existing one (conventional polarimetry). Nevertheless, for being a too recent field of study, the unconventional polarization concept is little known. For this reason there exists too little reported work on the study and characterization of beams of light with this type of polarization, being the most of them of theoretical character. This is why, the design and implementation of an optical arrangement that allows to handle with this kind of beams and to probe that they can be of great utility in important and well-established areas such as polarimetry, is a promising work in this emergent area.

1.4.   Scope and objectives of this work

1.4.1.   General objective

In this thesis work we aim to exploit the classical entanglement property of an azimuthally polarized beam of light to extract useful information of transparent, non depolarizing samples. The study is made by numerical, image processing and experimental methods.
The optical arrangement, even though based on an already existing purely theoretical proposal [Töppel et al. (2014)], will be adapted to the GIPYS lab materials and modified to be experimentally more robust and hence easier to work with.

1.4.2.   Particular objectives

- To modify and set up the theoretical optical arrangement to be used in the GIPYS lab with azimuthally polarized light.

- To obtain the Mueller matrix of a transparent, non depolarizing sample by means of an image based analysis.

1.5.   Outline

The thesis document is disposed as follows: In Chapter 2 it is presented the theoretical framework needed to understand the concepts, optical phenomena and methods addressed here.
In Chapter 3 it is shown the experimental arrangement, its characteristics and implementation.
In Chapter 4, the computational and experimental results are exhibited, together with their analysis and corresponding discussion.
In Chapter 5 the Conclusions and future work are exposed.
Finally, the developed algorithms are included in the Appendix section.

Chapter 2

Theoretical Framework

Nothing in life is to be feared, it is only to be
understood. Now is the time to understand more, so
that we may fear less.

Marie Curie

Summary: In this Chapter we give a brief resume about the theoretical framework on which this thesis work is based. We start with the generalities of conventional polarization, the mathematical tools used to describe it and the way to produce it and detect it. Then, the unconventional polarization is introduced along with the main stages of the experimental arrangement. Finally, we explain how each individual stage is handled in order to have the complete arrangement working as a unity.

2.1. Conventional polarization

Polarization is one of the 4 needed parameters to fully describe a light beam. So that, it is necessary to take it into account if we want to understand what happens when a beam of light interacts with matter. In fact, the change in polarization can bring sufficient data to fully determine the polarization characteristics of a sample. This is known as polarimetry. In polarimetry we can be interested in knowing the polarization characteristics of the beam of light (Stokes polarimetry) or on how a sample changes the polarization of the incident light (Mueller polarimetry). In this way, we can design and implement optical arrangements which allow us to make useful observations about an optical phenomena, only analyzing how the state of polarization of a light beam has changed after the interaction.

We can say that **polarization** is the term used to describe how the electric field of a beam of light (electromagnetic wave) is oscillating in both, space and time, while the propagation occurs. The electric field is mathematically described by an oscillating function, like a cosine or sine function, an amplitude (dependent on time and space, generally), an angular frequency, and an exponential term that describes how the beam is propagating in time. Taking into account that, in order to describe a physically realizable wave, it has to be described by a real quantity, what was said above can be expressed as [*]:

---

[*] This equations comes up from solving the wave equation at vacuum without sources or currents, in Cartesian coordinates $\nabla^2 E = \frac{1}{c^2} \frac{\partial^2 E}{\partial t^2}$.

$$\mathfrak{Re}\{\mathbf{E}(\mathbf{r},t) = \mathbf{A}(\mathbf{r},t)\exp(i(\omega t - \mathbf{k}\cdot\mathbf{r} + \phi))\} \tag{2.1}$$

Where $\mathfrak{Re}$ means the real part of the expression, $\mathbf{r}$ is the position vector, t is time, $\mathbf{A}$ is the amplitude of the wave, i is the imaginary number, $\mathbf{k}$ is the wavevector, ω is the angular frequency (related with the period, T, by $\omega = 2\pi/T$) and ϕ is a phase term used to stablish how many radians has travelled the wave from the origin of our reference system (of course it can be arbitrarily settled to zero by the proper election of a reference system and time of observation). If we could put a marker at the end of the electric field vector, the figure described by the marker at the end of a cycle (one spatial or temporal period) could be a set of points randomly disposed or could be a well known geometric figure (ellipse, circle or line). In the first case we would say that the beam is **non polarized**, because the electric field does not has an specific orientation preference. The Sun is a source of non polarized light, where the amplitude, phase and orientation of the electric field associated to each emitted wavelength change randomly.

In the opposite case, when the electric field vector has a preference to vibrate in an specific orientation, thus describing one of the previously cited figures, we say that the light is **completely polarized** (elliptically, circularly or linearly, respectively).

Of course the intermediate case is also possible, which could be thought as the combination of polarized and non polarized light. Then we would say the light is **partially polarized** and hence we can start to think in a way to know "how much" of the beam is polarized and "how much" is not. For this, we use the Degree of Polarization (**DoP**), defined as:

$$DoP = \frac{I_{pol}}{I_{tot}} \tag{2.2}$$

Where I_{pol} is the intensity of the polarized light and I_{tot} is the total intensity of the beam of light. Here we take the intensity of the beam defined as [Goldstein (2011)] $I = \mathbf{E}\cdot\mathbf{E}^*$. With $*$ indicating the complex conjugate operation.

2.1.1. Polarization ellipse

The fact that the light can or can not be polarized is related with the amplitude and phase of the constituent waves. We know that any vector can be expressed as a linear combination of two orthogonal vectors, say E_x and E_y, which propagate along the same direction. In our case these two vectors represent two monochromatic plane waves and will form our base. In general, these two plane waves will have different amplitudes, frequencies and phases. But, in the case that some of these characteristics are related, then we can obtain the mathematical expression of the mentioned figures.

Now we will investigate the resultant wave formed by the superposition of two plane monochromatic waves travelling in the z direction (in this way $\mathbf{r} = \mathbf{z}$ and $\mathbf{k}\cdot\mathbf{r} = kz$) and same frequency. Such as:

$$\mathbf{E}(z,t) = E_x(z,t)\hat{\boldsymbol{e}}_x + E_y(z,t)\hat{\boldsymbol{e}}_y \tag{2.3}$$

With $\hat{\boldsymbol{e}}_x$, $\hat{\boldsymbol{e}}_y$ being the unitary vectors in the x, y directions and

$$E_x = E_{0x}\cos(wt - kz + \phi_x) = E_{0x}\cos(\theta + \phi_x) \tag{2.4}$$

and

$$E_y = E_{0y}\cos(wt - kz + \phi_y) = E_{0y}\cos(\theta + \phi_y) \tag{2.5}$$

Where we have taken the convention $\mathfrak{Re}\{\exp(i\theta)\} = \cos(\theta)$, with $\theta = \omega t - kz$. E_{0x}, E_{0y} are the amplitudes of the x, y components of the electric field.

Our objective now is to obtain a function that is not dependent on space and time, i.e. we want to get rid of the term $\theta = \omega t - kz$. We begin dividing the equation 2.4 by E_{0x}, which results in an expression for $\cos\theta$ that we can substitute in the equation 2.5 divided by E_{0y} once we have used the trigonometric identity $\cos(\theta + \phi) = \cos(\theta)\cos(\phi) - \sin(\theta)\sin(\phi)$. Subtracting both results and rearranging terms we obtain [Cywiak (2016)]:

$$\frac{E_y}{E_0 y} - \frac{E_x}{E_0 x}\cos(\phi) = -\sin(\theta)\sin(\phi) \tag{2.6}$$

Note that we have set the phase relative to ϕ_x such that $\phi_y - \phi_x = \phi$.
Squaring the expression 2.6, changing $\sin^2(\theta) = 1 - \cos^2(\theta)$ in the right hand side of the result in order to substitute again $cos(\theta) = \frac{E_x}{E_{0x}}$, we can group common terms and reduce factors using again the trigonometrical identity $\cos^2(\theta) + \sin^2(\theta) = 1$. Multiplying by $E_{0y}^2 E_{0x}^2$ to get rid of the denominator and rearranging we obtain [Cywiak (2016)]:

$$E_{0y}^2 E_x^2 - 2E_{0x}E_{0y}E_x E_y \cos(\phi) + E_{0x}^2 E_y^2 = E_{0x}^2 E_{0y}^2 \sin^2(\phi) \tag{2.7}$$

Which is easier to interpret if we adopt the following notation [Cywiak (2016)]:

$$A \equiv E_{0y}^2$$
$$B \equiv -E_{0x}E_{0y}\cos(\phi)$$
$$C \equiv E_{0x}^2$$
$$D \equiv E_{0x}^2 E_{0y}^2 \sin^2(\phi)$$

Hence expression 2.7 rewrites as [Cywiak (2016)]:

$$AE_x^2 + 2BE_x E_y + CE_y^2 = D \tag{2.8}$$

Which remind us of the general equation of a conic. We notice that, from our definitions, $A \neq C$, $AC > 0$ and $B^2 - 4AC < 0$ then we are dealing with the equation of an ellipse; rotated since $B \neq 0$. This is known as the **polarization ellipse** and a schematic diagram of it is shown in figure 2.1. It is characterized by the two angular parameters [Goldstein (2011)] Ψ, the orientation angle, and χ, the ellipticity angle. These two parameters are related with the electric field amplitudes by [Cywiak (2016)]:

$$\tan 2\Psi = \frac{2E_{0x}E_{0y}\cos\phi}{E_{0x}^2 - E_{0y}^2} \qquad (0 \leq \Psi \leq \pi) \tag{2.9}$$

$$\sin 2\chi = \frac{2E_{0x}E_{0y}\sin\phi}{E_{0x}^2 + E_{0y}^2} \qquad (\frac{-\pi}{4} \leq \chi \leq \frac{\pi}{4}) \tag{2.10}$$

From the above derivation we conclude that the most general form of a completely polarized beam of light is an ellipse. Now we can make some other considerations in order to obtain the particular cases of circularly and linearly polarized light. For example, when $E_{0x} = E_{0y} = E_0$ and $\pm\phi = \pi/2$, then equation 2.7 reads:

$$E_x^2 + E_y^2 = E_0^2 \tag{2.11}$$

Which is the equation for a circle. Note that from this expression we can not tell if the phase difference was $-\pi/2$ or $\pi/2$. Knowing the phase difference value is important because it tell us if the electric field is rotating in time in the clockwise sense or in the counter-clockwise sense. In the first case we say that the light is **right-handed** polarized and we say that it is **left-handed** polarized in the opposite case. This convention applies also for elliptically polarized light. The
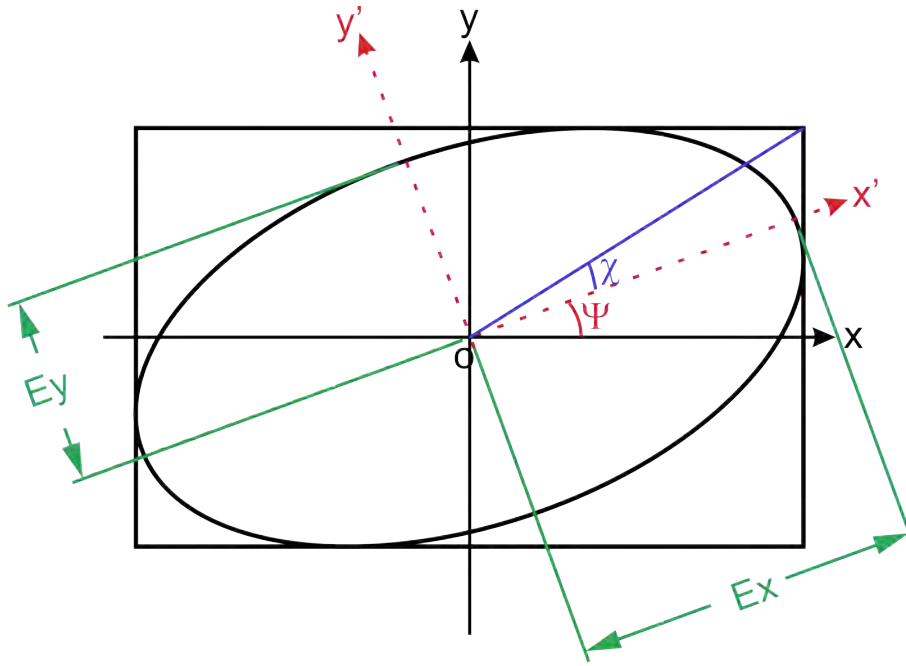
Figure 2.1: Polarization ellipse. Ψ corresponds to the orientation angle and χ to the ellipticity angle.

way to know the sense of rotation of the electric field is evaluating the corresponding expression, say 2.11 for this case, for several times at specific position (say z=0 for example). Doing this analysis we arrive to we have right-hand circular polarization when $\phi = \pi/2$ and left-hand circular polarization when $\phi = -\pi/2$. This holds for the "looking to the source" convention adopted here. Now for $E_{0x} = E_{0y} = E_0$ and $\phi = 0$ or $\phi = \pi$ then we arrive to

$$Ey = \pm \frac{E_{0y}}{E_{0x}} E_x \tag{2.12}$$

Which corresponds to the equation of the straight line with slope $\pm \frac{E_{0y}}{E_{0x}}$.

2.1.2. Mathematical representations for polarized light

As we can notice, to represent a beam of light by an expression like equation 2.4 would not be a practical way of working if we have to consider the superposition of several waves. For this reason it was seek the way to express the same wave as a column vector, in order to work with matrix algebra. Here we introduce the Jones formalism, which consists in represent the monochromatic plane wave at a particular instant t as:

$$E = \begin{bmatrix} E_x \\ E_y \end{bmatrix} = \begin{bmatrix} E_{0x} \exp(i\phi_x) \\ E_{0y} \exp(i\phi_y) \end{bmatrix} \tag{2.13}$$

A beam of light expressed as in equation 2.13 is known to be in the form of a **Jones vector**. This representation is useful only for work with completely polarized light, since there is not a representation for non- polarized or partially-polarized light. It is a common practice to consider a system where $\phi_x = 0, \phi_y = \phi$ or to define $\phi = \phi_y - \phi_x$. In addition, the vector is "normalized"

with respect of the first term and the normalization factor is not taken into account. In this form we can easily determine if the obtained Jones vector corresponds to linearly, circularly or elliptically polarized beam of light and also the sense of rotation of the electric field.

Another formalism that does not suffer of this limitation is the Stokes formalism, which describes the polarization of a beam of light by means of 4 quantities, known as the **Stokes parameters**, which, when disposed in a column vector form, constitute the so-called **Stokes vector** (Goldstein, 2011).

$$S = \begin{bmatrix} E_x E_x^* + E_y E_y^* \\ E_x E_x^* - E_y E_y^* \\ E_x E_y^* + E_x^* E_y \\ i(E_x E_y^* - E_x^* E_y) \end{bmatrix} = \begin{bmatrix} < E_{0x}^2 + E_{0y}^2 > \\ < E_{0x}^2 - E_{0y}^2 > \\ 2 < E_{0x} E_{0y} \cos(\phi) > \\ 2 < E_{0x} E_{0y} \sin(\phi) > \end{bmatrix} \tag{2.14}$$

The Stokes vector can also be expressed in terms of the orientation and ellipticity angles as (Goldstein, 2011):

$$\begin{bmatrix} S_0 \\ S_1 \\ S_2 \\ S_3 \end{bmatrix} = S_0 \begin{bmatrix} 1 \\ \cos(2\chi)\cos(2\Psi) \\ \cos(2\chi)\sin(2\Psi) \\ \sin(2\chi) \end{bmatrix} \tag{2.15}$$

The normalization factor S_0 is usually not taken into account when doing calculations. A set of Jones and Stokes representations for the most used polarization states of light in polarimetry is given in Table 2.1.

2.1.3. Generation and detection of polarized light

Now that we have a mathematical representation for polarized light, we will focus our attention on the tools needed to generate it. These tools are polarizing optical elements, such as polarizers and phase retarders, which are described by matrices. These matrices act over the input fields expressed as vectors. According to the formalism in which the electric fields are written, the corresponding representations for the polarizing elements can be stated as Jones matrices (for the Jones formalism) or as Mueller matrices (for the Stokes formalism).

In this work we will be specially interested in generate and detect 6 specific polarization states, since their detection will allow us to determine the Stokes vector of any input beam of light, as we will see later in this section. These polarization states are: Linear horizontal (H or p) [*], linear vertical (V or s)[*], linear at $+45°$ ($+45$ or $+$), linear at $-45°$ or equivalently at $135°$ (135 or $-$), circular right (R or r) and circular left (L or l), respectively.

The way to generate and detect the linear states is through a **linear polarizer**. This is a device that only allows the transmission of the light whose polarization direction coincides with the direction of the transmission axis of the polarizer. Any other component of the beam with different polarization is rejected (absorbed or deviated). Therefore, we can generate any linear polarization just rotating the transmission axis of the polarizer to the desired orientation.

Equations 2.16 and 2.17 show the Jones and the Mueller matrices, respectively, for the ideal linear polarizer with its transmission axis rotated to an angle θ with respect to the horizontal orientation, when the source is associated to unpolarized light.(Goldstein, 2011).

$$\mathbf{J_P}(\theta) = \begin{bmatrix} \cos^2(\theta) & \cos(\theta)\sin(\theta) \\ \cos(\theta)\sin(\theta) & \sin^2(\theta) \end{bmatrix} \tag{2.16}$$

---

[*]The letter p is used to represent the component of the electric field which is *parallel* to the plane of incidence and s is used for the *perpendicular* one. In this work, when generating and detecting states of polarization, the parallel component,p, will coincide with the horizontal, and the perpendicular,s, with the vertical.

Polarization State	Stokes Vector	Jones Vector
Linear horizontal	$\begin{bmatrix} 1 \\ 1 \\ 0 \\ 0 \end{bmatrix}$	$\begin{bmatrix} 1 \\ 0 \end{bmatrix}$
Linear vertical	$\begin{bmatrix} 1 \\ -1 \\ 0 \\ 0 \end{bmatrix}$	$\begin{bmatrix} 0 \\ 1 \end{bmatrix}$
Linear $+45°$	$\begin{bmatrix} 1 \\ 0 \\ 1 \\ 0 \end{bmatrix}$	$\frac{1}{\sqrt{2}} \begin{bmatrix} 1 \\ 1 \end{bmatrix}$
Linear $-45°$	$\begin{bmatrix} 1 \\ 0 \\ -1 \\ 0 \end{bmatrix}$	$\frac{1}{\sqrt{2}} \begin{bmatrix} 1 \\ -1 \end{bmatrix}$
Right circular	$\begin{bmatrix} 1 \\ 0 \\ 0 \\ 1 \end{bmatrix}$	$\frac{1}{\sqrt{2}} \begin{bmatrix} 1 \\ +i \end{bmatrix}$
Left circular	$\begin{bmatrix} 1 \\ 0 \\ 0 \\ -1 \end{bmatrix}$	$\frac{1}{\sqrt{2}} \begin{bmatrix} 1 \\ -i \end{bmatrix}$
Unpolarized light	$\begin{bmatrix} 1 \\ 0 \\ 0 \\ 0 \end{bmatrix}$	-

Table 2.1: Stokes and Jones vectors for most common used polarization states in conventional polarimetry. For the complete derivation of these expressions see for example, Goldstein (2011).

$$\mathbf{M_P}(\theta) = \frac{1}{2} \begin{bmatrix} 1 & \cos(2\theta) & \sin(2\theta) & 0 \\ \cos(2\theta) & \cos^2(2\theta) & \cos(2\theta)\sin(2\theta) & 0 \\ \sin(2\theta) & \cos(2\theta)\sin(2\theta) & \sin^2(2\theta) & 0 \\ 0 & 0 & 0 & 0 \end{bmatrix} \quad (2.17)$$

The next element to consider is the **linear retarder**. Usually, it is made from a birefringent element whose fast and slow axis are made to be orthogonal. The direction of the fast axis is marked in the plate and is taken as the reference from where the angle of rotation θ of the device, with respect to the horizontal, is measured. When settled to 0, the fast axis will coincide with our x direction. The polarization direction of the incident beam is decomposed with respect to the fast and slow directions of the plate, causing a delay in the fraction of the beam that travels through the slow axis and an advance in the part that travels through the fast axis. The emergent beam, thus, acquires a total phase retardation δ between its orthogonal components. The Jones and Mueller matrices for a linear retarder with fast axis at an angle θ and retardation of δ are

(Goldstein, 2011):

$$\mathbf{J_R}(\delta, \theta) = \begin{bmatrix} e^{i\delta}\cos^2(\theta) + \sin^2(\theta) & (e^{i\delta} - 1)\sin(\theta)\cos(\theta) \\ (e^{i\delta} - 1)\sin(\theta)\cos(\theta) & e^{i\delta}\sin^2(\theta) + \cos^2(\theta) \end{bmatrix} \tag{2.18}$$

$$\mathbf{M_R}(\delta, \theta) = \frac{1}{2} \begin{bmatrix} 1 & 0 & 0 & 0 \\ 0 & \cos^2(2\theta) + \sin^2(2\theta)\cos(\delta) & (1 - \cos(\delta))\sin(2\theta)\cos(2\theta) & -\sin(2\theta)\sin(\delta) \\ 0 & (1 - \cos(\delta))\sin(2\theta)\cos(2\theta) & \sin^2(2\theta) + \cos^2(2\theta)\cos(\delta) & \cos(2\theta)\sin(\delta) \\ 0 & \sin(2\theta)\sin(\delta) & -\cos(2\theta)\sin(\delta) & \cos(\delta) \end{bmatrix} \tag{2.19}$$

There are two linear retarders that are of special interest: The **half wave-plate** (**HWP**) and the **quarter wave-plate** (**QWP**). The first introduces a phase of π (which is half the spatial period, $\lambda = 2\pi$, of the wave, hence its name. This device is also represented as $\lambda/2$ WP) between the orthogonal components of the electric field. When applied to a linearly polarized field, the HWP rotates the direction of polarization by twice the angle between the direction of polarization and the fast axis of the wave-plate. The sense of rotation occurs towards the direction of the fast axis of the plate. The matrices for the half wave-plate with fast axis rotated an angle θ are obtained from equations 2.18 and 2.19 when substituting $\delta = \pi$:

$$\mathbf{J_R}(\frac{\lambda}{2}, \theta) = \begin{bmatrix} \cos(2\theta) & \sin(2\theta) \\ \sin(2\theta) & -\cos(2\theta) \end{bmatrix} \tag{2.20}$$

$$\mathbf{M_R}(\frac{\lambda}{2}, \theta) = \frac{1}{2} \begin{bmatrix} 1 & 0 & 0 & 0 \\ 0 & \cos(4\theta) & \sin(4\theta) & 0 \\ 0 & \sin(4\theta) & -\cos(4\theta) & 0 \\ 0 & 0 & 0 & -1 \end{bmatrix} \tag{2.21}$$

Where a $-$ sign was factored out from equation 2.20 and the trigonometric identities $2\sin(\theta)\cos(\theta) = \sin(2\theta)$ and $\cos^2(\theta) - \sin^2(\theta) = \cos(2\theta)$ were used to simplify the final expressions.
From here, we can obtain the Jones and Mueller matrices of the HWP when its fast axis is at $0°$:

$$\mathbf{J_R}(\frac{\lambda}{2}, 0°) = \begin{bmatrix} 1 & 0 \\ 0 & -1 \end{bmatrix} \tag{2.22}$$

$$\mathbf{M_R}(\frac{\lambda}{2}, 0°) = \frac{1}{2} \begin{bmatrix} 1 & 0 & 0 & 0 \\ 0 & 1 & 0 & 0 \\ 0 & 0 & -1 & 0 \\ 0 & 0 & 0 & -1 \end{bmatrix} \tag{2.23}$$

From the properties of rotation of the HWP explained above, it is possible to see that the rotated linear states can also be generated with a horizontal polarizer (polarizer with its transmission axis at $0°$) followed by a half wave-plate with its fast axis at $\theta/2$, being θ the angle of the desired polarization direction. The matrices for the horizontal linear polarizer are obtained when doing $\theta = 0$ on equations 2.16 and 2.17, (Goldstein, 2011):

$$\mathbf{J_P}(0°) = \begin{bmatrix} 1 & 0 \\ 0 & 0 \end{bmatrix} \tag{2.24}$$

$$\mathbf{M_P}(0°) = \frac{1}{2} \begin{bmatrix} 1 & 1 & 0 & 0 \\ 1 & 1 & 0 & 0 \\ 0 & 0 & 0 & 0 \\ 0 & 0 & 0 & 0 \end{bmatrix} \tag{2.25}$$

The other special case of linear retarder that we will be interested in, is the **quarter wave-plate** (**QWP**). The quarter wave-plate is an element that introduces a retardation of $\pi/2$ (which is a quarter of the spatial period of the wave, hence its name. This device is also represented as $\lambda/4$ WP) between the orthogonal components of the electric field. When we use a polarizer with its transmission axis at 0° followed by a quarter wave-plate with its fast axis at ±45°, we can generate circular right and left polarizations, respectively (in the "looking to the source convention"). The Jones and Mueller matrix for this specific orientation of the QWP can be obtained from equations 2.18 and 2.19 when placing $\delta = \pi/2$ and $\theta = \pm 45°$:

$$\mathbf{J_R}(\frac{\lambda}{4}, \pm 45°) = \begin{bmatrix} 1 & \pm i \\ \pm i & 1 \end{bmatrix} \tag{2.26}$$

$$\mathbf{M_R}(\frac{\lambda}{4}, \pm 45°) = \begin{bmatrix} 1 & 0 & 0 & 0 \\ 0 & 0 & 0 & \mp 1 \\ 0 & 0 & 1 & 0 \\ 0 & \pm 1 & 0 & 0 \end{bmatrix} \tag{2.27}$$

While the corresponding matrices for the QWP with its fast axis at 0° are:

$$\mathbf{J_R}(\frac{\lambda}{4}, 0°) = \begin{bmatrix} i & 0 \\ 0 & 1 \end{bmatrix} \tag{2.28}$$

$$\mathbf{M_R}(\frac{\lambda}{4}, 0°) = \begin{bmatrix} 1 & 0 & 0 & 0 \\ 0 & 1 & 0 & 0 \\ 0 & 0 & 0 & 1 \\ 0 & 0 & -1 & 0 \end{bmatrix} \tag{2.29}$$

At this stage, we can see that any of the desired states can be generated just with a linear polarizer and a quarter wave-plate. These two elements conform what we call the **"Polarization State Generator"** (PSG) and placed in the mirrored configuration (first the quarter wave plate, then the linear polarizer), they give rise to the **"Polarization State Analyzer"** (PSA). The latter needing also a detector, which is a camera in our case. Notice when analyzing linear polarization we use only the polarizer and when analyzing circular polarizations we use the QWP at ±45° followed by the horizontal polarizer to analyze circular left and right polarizations, respectively.

2.1.3.1.   Determination of the Stokes vector

Earlier we said that the generation and detection of 6 specific polarization states ({*horizontal*, *vertical*, ±45°, *circular right* and *circular left*}, respectively), would allow us to determine the polarization of any beam of light. In order to achieve this, we use the ideal polarimetric arrangement (IPA) method (Espinosa-Luna and Zhan, to be published in 2017) which consists of measuring the intensity of the beam when the transmission axis of the polarizer is horizontal (measurement registered as I_0), vertical (registered as I_{90}), at +45° (registered as I_{+45}), at 135° (registered as I_{135}), at 0 again when preceded by a quarter wave plate with fast axis at ±45° (the measured intensity will be called I_L and I_R, respectively).

When having all these measurements, the Stokes vector of the analyzed beam will be given by (Espinosa-Luna and Zhan, to be published in 2017):

$$S = \begin{bmatrix} I_0 + I_{90} \\ I_0 - I_{90} \\ I_{45} - I_{135} \\ I_R - I_L \end{bmatrix} \tag{2.30}$$

The determination of the Stokes vector of the beam at different stages on the experimental setup is needed in this work in order to assure that we are working with the desired polarizations and also as a way of checking that our experimental arrangements work as expected.

2.1.3.2.   Determination of the Mueller matrix

Going further, it is possible to determine all the Mueller matrix elements following a procedure similar to the one described in the previous section. In this case, the sample under study is illuminated with one of the polarizations of the set $\{horizontal, vertical, +45°, circular\ right\}$ and then, the intensity of the emerging beam is registered when it is analyzed for each of the 4 polarization states. In this case, we use two index to label each intensity: The first one corresponds to the polarization of the incident beam over the sample,(p→horizontal, s→ vertical, $+ \rightarrow +45°$, r→circular right) and the second one to the polarization state being analyzed. For example, the intensity registered when the beam is illuminated with horizontal polarization and analyzed by circular right, will be labelled as I_{pr}. Finally, we can compute each element of the Mueller matrix with the next expressions (Atondo-Rubio et al., 2005):

$$
\begin{aligned}
m_{00} &= \frac{1}{2}(I_{pp} + I_{ps} + I_{sp} + I_{ss}) \\
m_{01} &= \frac{1}{2}(I_{pp} + I_{ps} - I_{sp} - I_{ss}) \\
m_{02} &= I_{+p} + I_{+s} - \frac{1}{2}(I_{pp} + I_{ps} + I_{sp} + I_{ss}) \\
m_{03} &= I_{rp} + I_{rs} - \frac{1}{2}(I_{pp} + I_{ps} + I_{sp} + I_{ss}) \\
m_{10} &= \frac{1}{2}(I_{pp} - I_{ps} + I_{sp} - I_{ss}) \\
m_{11} &= \frac{1}{2}(I_{pp} - I_{ps} - I_{sp} + I_{ss}) \\
m_{12} &= I_{+p} - I_{+s} - \frac{1}{2}(I_{pp} - I_{ps} + I_{sp} - I_{ss}) \\
m_{13} &= I_{rp} - I_{rs} - \frac{1}{2}(I_{pp} - I_{ps} + I_{sp} - I_{ss}) \\
m_{20} &= I_{p+} + I_{s+} - \frac{1}{2}(I_{pp} + I_{ps} + I_{sp} + I_{ss}) \\
m_{21} &= I_{p+} - I_{s+} - \frac{1}{2}(I_{pp} + I_{ps} - I_{sp} - I_{ss}) \\
m_{22} &= 2I_{++} - I_{+p} - I_{+s} - I_{p+} - I_{s+} + \frac{1}{2}(I_{pp} + I_{ps} + I_{sp} + I_{ss}) \\
m_{23} &= 2I_{r+} - I_{rp} - I_{rs} - I_{p+} - I_{s+} + \frac{1}{2}(I_{pp} + I_{ps} + I_{sp} + I_{ss}) \\
m_{30} &= I_{pr} + I_{sr} - \frac{1}{2}(I_{pp} + I_{ps} + I_{sp} + I_{ss}) \\
m_{31} &= I_{pr} - I_{sr} - \frac{1}{2}(I_{pp} + I_{ps} - I_{sp} - I_{ss}) \\
m_{32} &= 2I_{+r} - I_{+p} - I_{+s} - I_{pr} - I_{sr} + \frac{1}{2}(I_{pp} + I_{ps} + I_{sp} + I_{ss}) \\
m_{33} &= 2I_{rr} - I_{rp} - I_{rs} - I_{pr} - I_{sr} + \frac{1}{2}(I_{pp} + I_{ps} + I_{sp} + I_{ss})
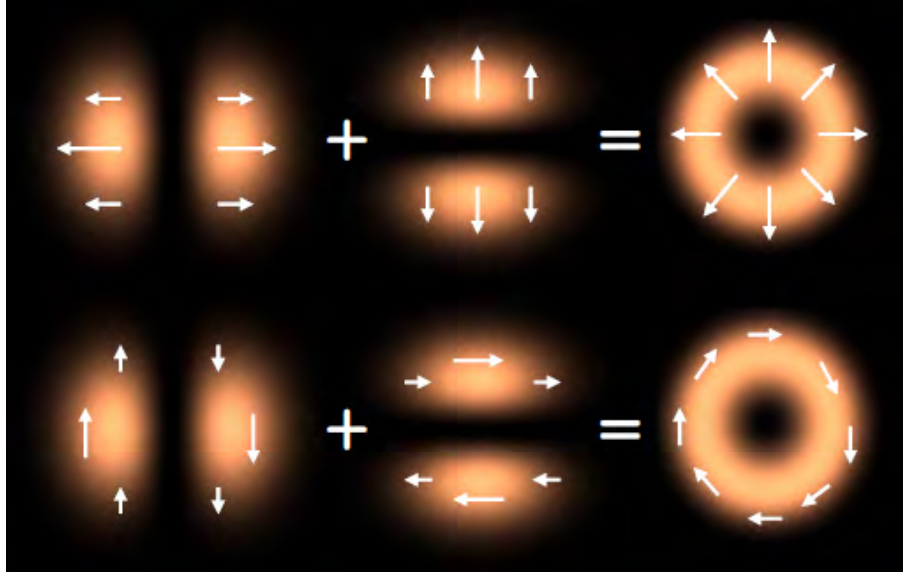\end{aligned}
\tag{2.31}
$$

Figure 2.2: Radial and azimuthal polarization modes graphically expressed as the linear combination of two orthogonally polarized HG modes, where the arrows represent electric field components. Taken from Zhan (2009).

2.2. Unconventional polarization

The unconventional polarization is distinguished from the conventional one for the fact that it has a non uniform spatial and phase distribution across the beam transversal section (Zhan, 2014). This means that each point on the transverse section has associated its own electric field vector with different orientation one from another, in contrast with the conventional polarized beam, where all the electric field vectors associated to each point are identical among them. The orientation and phase of these electric field vectors along with its localization at the transverse section of the beam leads to different modes of polarization, say **radial** ($\mathbf{E_r}$), **azimuthal** ($\mathbf{E}_\phi$) or a combination of them.

The geometries of radially and azimuthally polarized beams are shown in figure 2.2. The radial and azimuthal modes can be obtained through a combination of the 1st order horizontal and vertical Hermite-Gaussian beams, (Ψ_{10} and Ψ_{01}, respectively, that also will be represented indistinctly throughout this work as HG_{10} and HG_{01}, respectively) with the appropriate polarization distribution,Töppel et al. (2014):

$$\mathbf{E_r} = \frac{1}{\sqrt{2}}(\Psi_{10}\hat{\mathbf{e}}_x + \Psi_{01}\hat{\mathbf{e}}_y) \tag{2.32}$$

$$\mathbf{E}_\phi = \frac{1}{\sqrt{2}}(-\Psi_{01}\hat{\mathbf{e}}_x + \Psi_{10}\hat{\mathbf{e}}_y) \tag{2.33}$$

With $\hat{\mathbf{e}}_x$ and $\hat{\mathbf{e}}_y$ being the unitary vectors in the x and y directions, respectively. The Ψ_{10} and Ψ_{01} (or HG_{10} and HG_{01}) modes are the first order solutions in Cartesian coordinates for the scalar Helmholtz equation, (Zhan, 2009):

$$(\nabla^2 + k^2)E = 0 \tag{2.34}$$

With ∇^2 being the Laplace operator, $k = 2\pi/\lambda$ the wave number and E the amplitude of the electric field.

Mathematically, the Hermite-Gauss solution HG_{mn} modes have the following form (Zhan, 2009):

$$u(x,y,z) = E_0 H_m(\sqrt{2}\frac{x}{w(z)}) H_n(\sqrt{2}\frac{y}{w(z)}) \frac{w_0}{w(z)} exp[-i\phi_{mn}(z)] exp[i\frac{k^2}{r}2q(z)] \qquad (2.35)$$

Where $H_m(x)$ denotes the Hermite polynomials, E_0 is a constant electric field amplitude, w(z) is the beam size, w_0 is the beam size at beam waist, $z_0 = \pi w_0^2/\lambda$ is the Rayleigh range, $q(z) = z - iz_0$ is the complex beam parameter and $\phi_{mn}(z) = (m+n+1)tan^{-1}(z/z_0)$ is the Gouy phase shift. Of course other representations for the azimuthal and radial polarizations are also possible. For example, choosing a base constituted by the HG diagonal modes (represented here by $\Psi_\pm$) with $\pm 45°$ linear polarization(Töppel et al., 2014)[*]:

$$\mathbf{E_r} = \frac{1}{\sqrt{2}}(\Psi_+ \hat{\mathbf{e}}_+ + \Psi_- \hat{\mathbf{e}}_-) \qquad (2.36)$$

$$\mathbf{E_\phi} = \frac{1}{\sqrt{2}}(\Psi_- \hat{\mathbf{e}}_+ - \Psi_+ \hat{\mathbf{e}}_-) \qquad (2.37)$$

With $\Psi_\pm = (\Psi_{10} \pm \Psi_{01})/\sqrt{2}$ and $\hat{\mathbf{e}}_\pm = (\hat{\mathbf{e}}_x \pm \hat{\mathbf{e}}_y)/\sqrt{2}$.
Another representation is obtained when choosing the Laguerre-Gaussian (LG) modes, (that are the solutions in cylindrical coordinates to the equation 2.34 and will be represented also as Ψ_R and Ψ_L) with circular polarizations (Töppel et al., 2014):

$$\mathbf{E_r} = \frac{1}{\sqrt{2}}(\Psi_L \hat{\mathbf{e}}_R + \Psi_R \hat{\mathbf{e}}_L) \qquad (2.38)$$

$$\mathbf{E_\phi} = \frac{i}{\sqrt{2}}(\Psi_L \hat{\mathbf{e}}_R - \Psi_R \hat{\mathbf{e}}_L) \qquad (2.39)$$

With $\Psi_R = (\Psi_{10} - i\Psi_{01})/\sqrt{2}$, $\Psi_L = (\Psi_{10} + i\Psi_{01})/\sqrt{2}$, $\hat{\mathbf{e}}_R = (\hat{\mathbf{e}}_x - i\hat{\mathbf{e}}_y)/\sqrt{2}$ and $\hat{\mathbf{e}}_L = (\hat{\mathbf{e}}_x + i\hat{\mathbf{e}}_y)/\sqrt{2}$. The Laguerre-Gauss solution LG_{pl} modes are given by(Zhan, 2009):

$$u(r,\phi,z) = E_0(\sqrt{2}\frac{r}{\omega})^l L_p^l(2\frac{r^2}{\omega^2})\frac{w_0}{w(z)} exp[-i\phi_{pl}(z)] exp[i\frac{k}{2q(z)}r^2] exp(il\phi) \qquad (2.40)$$

Where $\phi_{pl}(z) = (2p+l+1)tan^{-1}(z/z_0)$ is the Gouy phase shift and ω the angular frequency of the wave.
An image with these 3 different representations for the radial polarization is shown in Figure 2.3. Equations (2.32, 2.33, 2.36-2.39) are a special kind of unconventional polarization: they represent classical entangled polarization states (Töppel et al., 2014). In this case, the entangled degrees of freedom are the polarization states and the spatial distributions (Hermite-Gauss or Laguerre-Gauss modes). As pointed out clearly by Töppel,et al., they are nonseparable or clasically entangled, because "one needs two coordinate-independent Jones vectors and two independent scalar fields (modes) to represent the electric field". This is an intra-system or classical entanglement, because occurs at a single beam of light; contrary to the inter-system or quantum entanglement, which occurs between two different beams.
There are several ways to generate unconventional polarization. They can be grouped in active and passive methods. In the active methods the generation is made inside the laser cavity, while in the passive methods the generation is obtained outside of it (Zhan, 2009). In this thesis work, we use a passive method to obtain azimuthal polarization.

---

[*]Notice that from here, all the equations corresponding to azimuthal polarization were obtained following the convention presented by (Töppel et al., 2014), since they are not explicitly stated in their article.
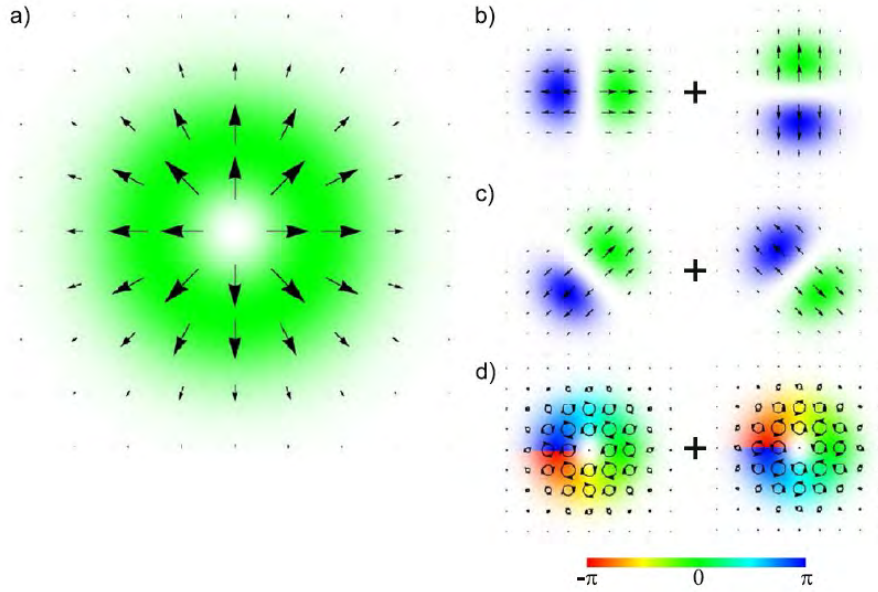
Figure 2.3: a) Radial polarization and its representation as the linear combination of two orthogonally polarized modes in 3 different basis: b) horizontal and vertical HG modes (Ψ_{10} and Ψ_{01}), c) diagonal HG modes (Ψ_+ and Ψ_-), d) Laguerre-Gaussian modes (Ψ_R and Ψ_L). Taken from Töppel et al. (2014).

2.3. Description of the main stages of the experimental arrangement

2.3.1. Generation of azimuthally polarized light: The S-waveplate

In order to generate an azimuthally polarized beam of light, it is used a commercial, passive plate converter, known as S-waveplate (Altechna (2013)). This device was developed at the group of Optoelectronics Research Centre at Southampton University, by Prof. Peter G. Kazansky. It is a single optical element, produced by direct laser writing technique that uses ultra-short (femto-second) pulses of light to form birefringence self-assembled nano gratings in a transparent material (BK7). The period of the grating is smaller than the wavelength of a visible light. The configuration of nano gratings occupies a space of 6 mm and its distribution is shown in figure 2.4a.

The device we have employed operates at 532.8 nm and converts horizontally linear polarized light into azimuthally polarized light when the mark in the plate is oriented at $-45°$ with respect to the horizontal. A radially polarized beam is obtained when the mark is oriented at $45°$ for the same incident polarization. These facts differ from the manual´s specifications and were observed and experimentally determined for several of our group members (see for example Aguilar (2017)). A photograph of the S-waveplate between crossed polarizers can be found in Altechna web page: [http://www.altechna.com/product_details.php?id=1048] and is shown in Figure 2.4b.

2.3.2. Mode converter

We use here the proposal by Beijersbegen et al. (1992) to construct a mode converter by the use of two identical cylindrical lenses of focal length of f_{cyl}, separated a distance of $2f_{cyl}$ (π **mode**

Figure 2.4: a)Geometrical disposition of the nano gratings in the s-wave converter. Taken from Beresna and Kazansky (2014). b) Photograph of the S-waveplate between crossed polarizers. Taken from the web-page of Altechna.

converter, which transforms $HG_{45°}$ and $HG_{-45°}$ into HG_{10} and HG_{01}, respectively) or $f_{cyl}\sqrt{2}$ ($\pi/2$ **converter** which transforms LG_{10} and LG_{01} modes into HG_{10} and HG_{01}, respectively). They begin by showing that a conversion is possible from the fact that a LG mode and a HG mode whose principal axes make an angle of 45° with the (x,y) axes, can be both decomposed in the same constituent set (Beijersbegen et al., 1992):

$$u_{nm}^{LG}(x,y,z) = \sum_{k=0}^{N} i^k b(n,m,k) u_{N-k,k} HG(x,y,z) \tag{2.41}$$

with real coefficients (Beijersbegen et al., 1992)

$$b(n,m,k) = \left(\frac{(N-k)!\,k!}{2^N n!\,m!}\right)^{1/2} \frac{1}{k!}\frac{d^k}{dt^k}[(1-t)^n(1+t)^m]_{t=0} \tag{2.42}$$

The factor in equation 2.41 corresponds to a $\pi/2$ relative phase difference between successive components. While for the HG mode described before:

$$u_{nm}^{HG}\left(\frac{x+y}{\sqrt{2}}, \frac{x-y}{\sqrt{2}}, z\right) = \sum_{k=0}^{N} b(n,m,k) u_{N-k,k}^{HG}(x,y,z) \tag{2.43}$$

With the same real coefficients b(n,m,k) as above. In this expansion, however, the successive components are in phase. The authors point out that a conversion between these two modes is possible by adding the adequate phase and they propose to use the **Gouy phase** $\psi(z)$ of a Gaussian mode, i.e. "the phase shift that the beam undergoes when going through a waist compared to that of a plane wave" (Beijersbegen et al., 1992). Therefore, the idea is just to make astigmatic a beam in a confined region only and isotropic outside that region. In this way, the HG components oriented along the axes of astigmatism will gain a phase difference while passing through this region. If a cylindrical lens is placed at the position where the two transverse radii of astigmatic beam are equal, the radii of curvature can be matched such that the beam outside the lens is no longer astigmatic. Going further, if an identical cylindrical lens is also placed on the other side of the waist and the beam is properly mode-matched, the beam is astigmatic only between the two lenses.

When doing the corresponding analysis, it is seen that, in order to obtain the desired phase, the distance between the lenses is $2f_{cyl}$ for the π converter and $f_{cyl}\sqrt{2}$ for the $\pi/2$ converter.

Notice that the π converter (U_π) acts as a HWP for modes and as such, it can be expressed through the Jones matrix for a HWP rotated an angle $\theta = \frac{\pi}{8}$ (Töppel et al., 2014)[*]:

$$U_\pi(\pi/8) = \frac{-i}{\sqrt{2}} \begin{bmatrix} 1 & 1 \\ 1 & -1 \end{bmatrix} \tag{2.44}$$

While the $\pi/2$ converter ($U_{\frac{\pi}{2}}$) acts as a QWP for modes and as such, can be expressed through the Jones matrix for a QWP rotated an angle $\theta = \frac{\pi}{4}$, (Töppel et al., 2014)*:

$$U_{\frac{\pi}{2}}(\pi/4) = \frac{1}{\sqrt{2}} \begin{bmatrix} 1 & -i \\ -i & 1 \end{bmatrix} \tag{2.45}$$

Notice that Töppel et al. (2014) describe the polarization along the propagation direction.

The $\pi/2$ converter has another restriction: the input beam must have a Rayleigh range, z_R, given by (Beijersbegen et al. (1992)):

$$z_R = (1 + 1/\sqrt{2})f_{cyl} \tag{2.46}$$

in order to fullfill the mode-matching condition, which corresponds to a beamwaist, ω_{02}, between the cylindrical lenses of (Padgett et al., 1996)

$$\omega_{02} = \sqrt{\lambda z_R / \pi} \tag{2.47}$$

From here we know that, experimentally, we can achieve the mode-matching condition using a lens of focal length $f \geq f_0$, with (Marcuse, 1982)

$$f_0 = \frac{\pi}{\lambda} \omega_{01} \omega_{02} \tag{2.48}$$

Where ω_{01} is the beamwaist of the incident available beam of light and ω_{02} is the desired beamwaist. The mode-matching lens will be placed at a distance, (Marcuse, 1982):

$$d_1 = f \pm \frac{\omega_{01}}{\omega_{02}} \sqrt{f^2 - f_0^2} \tag{2.49}$$

from the incident beamwaist and the desired beamwaist will be at a distance d_2 of the mode-matching lens, (Marcuse, 1982):

$$d_2 = f \pm \frac{\omega_{02}}{\omega_{01}} \sqrt{f^2 - f_0^2} \tag{2.50}$$

So, choosing the minimum required focal length of the mode-matching lens, $f = f_0$ we will put such a lens at a distance f_0 from the incident beamwaist and we will place the mode converter at a distance f_0 from the mode-matching lens, where the desired beamwaist is generated. All these quantities are represented in the Figure 2.5.

---

[*]These expressions were obtained following the Töppel et al. (2014) convention, since they are not explicitly stated in their article.
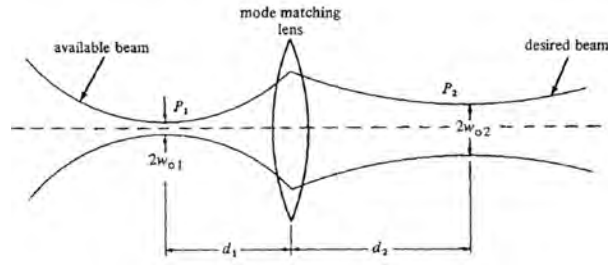
Figure 2.5: Mode-matching of a Gaussian beam by means of a lens. Taken from Marcuse (1982).
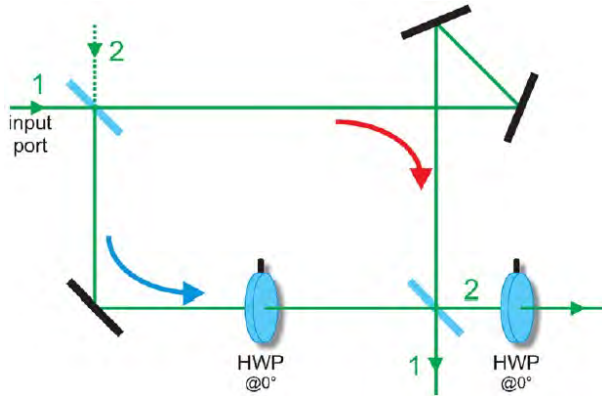

Figure 2.6: Physical implementation of the mode beam splitter. Taken from Töppel et al. (2014).

2.3.3.   Mode beam splitter

The mode beam splitter is an ingenious arrangement capable of divide any incident beam into its HG_{10} and HG_{01} components. It was first proposed by (Sasada and Okamoto, 2003) and consisted of a Mach-Zehnder interferometer with an extra mirror in one of its arms. The inclusion of this mirror allows to distinguish between the HG_{10} and the HG_{01} modes, taking advantage of its symmetry: the HG_{01} mode is symmetric under reflection through the y axis while the HG_{10} mode is anti-symmetric, thus after reflection the anti-symmetric modes get an extra-phase of π while the symmetric-modes continue unaffected. This setup worked as transverse mode-beam splitter when the input beam was linearly x or y polarized and acted as a polarizing beam splitter when the input beam was a HG_{10} or HG_{01} mode. (Sasada and Okamoto, 2003). However, for any other combination (say a diagonal HG_{10} mode with linear polarization at 45°), the output beam was an hybrid state, because the interferometer was not capable of distinguish between modes with the same parity, (Sasada and Okamoto, 2003). This means that, if we send an azimuthal beam, because its orthogonal components are odd bases, they would be sent to the same port. This arrangement was latter modified by (Töppel et al., 2014), who added 2 half wave plates with their fast axes horizontal in the other arm, as shown in the Figure 2.6. The outputs of this new arrangement are the orthogonal HG_{10} and HG_{01} modes that will appear in one or another port depending on the polarization of the constitute basis associated to the unconventional polarization state under study. Thus allowing to decompose the azimuthal beam into its HG_{01} x polarized and HG_{10} y polarized basis. In order that the modified Mach-Zehnder interferometer (**MMZI**) exhibits this behavior (acts as a mode-beam splitter), several conditions must be satisfied, (Töppel et al., 2014):

- The beam splitters used in the arrangement must be such that the phase acquired between the x and y polarization components in reflection through any of the input ports is π, (the same caused by the mirrors) and nothing in transmission.

Figure 2.7: Schematic diagram of the experimental process.

- The phase difference between the arms must be of π (this includes the phase caused by the difference in geometrical paths).

This setup has important implications because it allows to sorter the beam depending on its mode symmetry and polarization, thus having direct applications in quantum cryptography (Luda et al., 2014).

2.4.   Assembly of all components

Once we had reviewed each of the main components of the complete arrangement, we are now in position to explain how they are assembled in order to work as a whole. The process is explained in the schematic diagram of Figure 2.7. We follow a sequential process: The azimuthally polarized beam is generated and made to pass through the sample, then the beam (that we will call the sample beam) is redirected to mode converter A (MCA) and passed through the modified Mach-Zehnder interferometer (MMZI). Later, the resultant interferograms at each output port are analyzed using a polarization state analyzer (PSA) and registered as images using a camera. Once we have the information for MCA, we proceed to adequate MCA to obtain MCB, redirect the sample beam to pass through the MCB and repeat the steps from here. Once the data is collected, we redirect the light to pass through MCC and follow the previous procedure in order to obtain the images for this mode converter. Once we have all the necessary information, we process them using the algorithms shown in Appendix C.2 in order to obtain the Mueller matrix of the sample.

We point out here that our experimental process considerably differs from the original one (Töppel et al., 2014), which considers the use of 26 identical photodetectors (that could be reduced to a minimum of 16), for the Mueller matrix determination at a single shot. Taking into account our critical economical situation, the experimental implementation of the original proposal is outside of our possibilities. Instead, we have proposed to work with images (which provide us with spatially resolved intensity) and a single CMOS camera to detect the 16 measurements that will allow us to find the Mueller matrix of our samples.

In order to correctly identify which image provides which intensity data,i.e. in order to know which image will be our $I_{\mu\nu}$ data source, we present a diagram following the process that the beam undergoes when passing through the complete optical arrangement. This process is shown in Figure 2.8. The basic idea is as follows: We have a classically entangled beam of light; the azimuthal beam, which can be represented as a linear combination of the appropriate modes and polarizations (as was explained in Section 2.2). We work with 3 different basis: Linear horizontal/vertical, linear at $\pm 45°$ and circular right/left. After passing through a transparent, non depolarizing sample, (in the case shown in diagram of Figure 2.8, this sample is air), the original polarization is altered while the modes keep unchanged. Then, we make a change of mode

basis without altering the polarization through an appropriate mode converter: MCA for circu-
lar basis, which transforms Laguerre-Gaussian modes in Hermite-Gaussian modes; MCB which
converts diagonal Hermite-Gaussian modes in horizontal and vertical Hermite-Gaussian modes
and MCC which leaves the modes unaltered. Finally, a mode beam splitter (Modified Mach-
Zehnder interferometer) is used in order to separate the beam into its horizontal and vertical
Hermite-Gaussian mode components without changing the polarization of the beam. In this way,
we are able to independently identify how each of our conventional polarization basis elements
have been altered by the sample using a polarization state analyzer and a camera. The Mueller
matrix of the sample is obtained through an algorithm that processes the images following the
expressions derived by Töppel, which are shown in Appendix A.

With this diagram, it is very easy and instructive to compute the resultant Mueller matrix for
air, just taking into account that the normalized theoretical intensity measured at the output
ports of the interferometer will be 1 if the state of polarization being analyzed coincides with
the polarization of the output mode (for example I01 which is the intensity obtained when we
place a horizontal polarizer to measure the $\Psi_{01}\hat{e}_x$ mode); 0 if we are measuring the orthogonal
polarization (for example I11, which is the intensity obtained when we place a linear polarizer
with its transmission axis at 90° with respect to the horizontal to analyze the $\Psi_{01}\hat{e}_x$ mode) and
1/2 if the tested polarization can be decomposed in the analyzed polarization basis (for example
I21, which is the intensity obtained when we place the linear polarizer at 45° to analyze the
$\Psi_{01}\hat{e}_x$ mode).

Another remark has to be done: The relationships presented by Töppel et al. (2014) are obtained
following a different ordering (quantum ordering) for the Pauli matrices, which lead to different
ordering to the Stokes vectors and to the Mueller matrices. However, Töppel Mueller matrix and
the Mueller matrix we are used to (the matrices presented in Subsection 2.1.3 and which Aiello
refers to be in the Born-Wolf convention), are related through the simple expression(Aiello and
Woerdman, 2006):

$$M_{BW} = Q_{BW}^{-1} M Q_{BW} \tag{2.51}$$

With (Aiello and Woerdman, 2006)

$$\mathbf{Q_{BW}} = \begin{bmatrix} 1 & 0 & 0 & 0 \\ 0 & 0 & 1 & 0 \\ 0 & 0 & 0 & -1 \\ 0 & 1 & 0 & 0 \end{bmatrix} \tag{2.52}$$

and

$$\mathbf{Q_{BW}^{-1}} = \begin{bmatrix} 1 & 0 & 0 & 0 \\ 0 & 0 & 0 & 1 \\ 0 & 1 & 0 & 0 \\ 0 & 0 & -1 & 0 \end{bmatrix} \tag{2.53}$$

Where M_{BW} is the Mueller matrix as defined by Born and Wolf, Q_{BW} is the transformation
matrix between Born-Wolf and Töppel et. al. conventions, Q_{BW}^{-1} is the inverse matrix of the
matrix transformation Q_{BW} and M is the Mueller matrix as obtained by Töppel.

We added the equations 2.51-2.53 at the end of our code when obtaining the experimental Mueller
matrices of our samples when using azimuthal polarization in order to obtain the resultant
Mueller matrix in the optical convention.

When taking this into account, the reader can verify that the obtained and converted theoretical
Mueller matrices for a $\lambda/2$ WP @0° and a $\lambda/4$ WP @0° are the same as the ones presented in
equations 2.23 and 2.29, respectively. These procedures are explicitly shown in the corresponding
Results Section.

Also, for the diagram presented here, we can see that the Mueller matrix for air is the identity matrix, as can be verified following the preceding procedure.
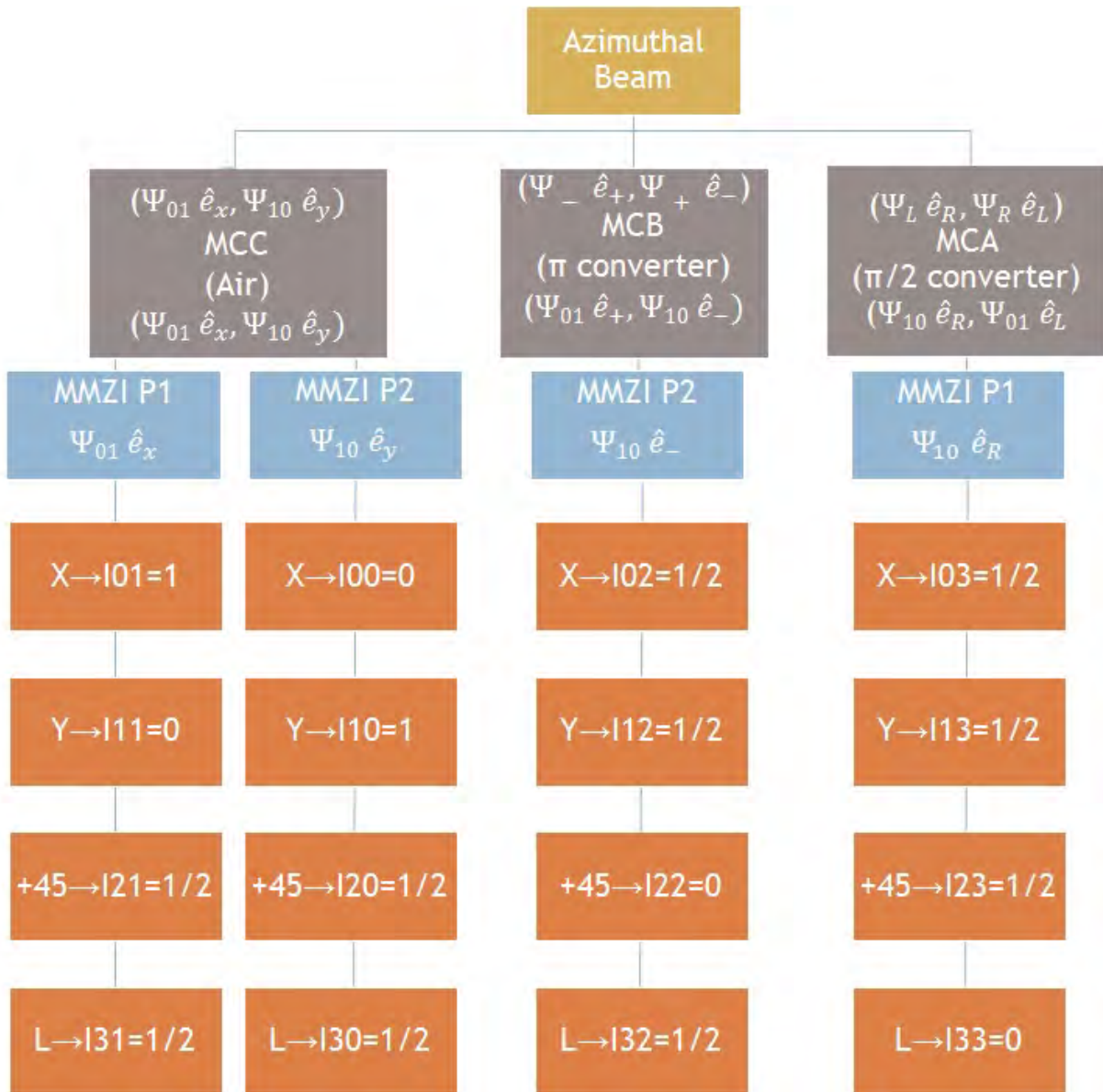
Figure 2.8: Diagram of the changes in polarization and spatial degrees of freedom that the azimuthal beam undergoes when passing through the experimental arrangement.

Chapter 3

Experimental Setup

*Success is going from failure to failure without
losing your enthusiasm.*

Winston Churchill.

Summary: This Chapter will cover the methodological procedure that was followed during
the experiments in order to properly handle each step of the complete arrangement. During
the process, we found several challenges to solve in order to get each individual part working
properly. We mention these challenges and how they were solved. Finally, we describe how
the system was used as a whole in order to obtain the images from which the Mueller matrix
of air and 2 waveplates samples were derived.

3.1.   Generation of the azimuthally polarized beam of light

The first step in the experimental setup consisted in generate the best azimuthal polarization
that can be provided by the S-waveplate. For this, it was necessary to filter and collimate the
beam provided by the Thorlabs CPS532 laser diode that was used as a light source, since it was
experimentally noticed that the cross-section intensity of this beam was not uniform; a key fact
to be take care of if we wish to achieve the characteristic symmetry of the azimuthal polarization
and of the modes that compose it.
For the spatial filtering process, we used the Newport 910A Spatial Filter, together with its
suggested M-10x Microscope Objective and 910PH-25 Pinhole. In order to collimate the beam
we used a biconvex lens of 50 mm focal length which provided us with a collimated beam of 5
mm in diameter.
For the linear polarization required by the S-waveplate, we used the CM1-PBS251 polarizing
beam splitter from Thorlabs, since we also wanted to split the beam in order to use it in other
experiments. Once the beam got linear horizontal polarization, it was sent to the S-waveplate
passing through an iris diaphragm in order to control the beam size. This is important for the
mode-matching process, as we will see later. The reference mark on the S-waveplate was oriented
to -45° with respect to the horizontal plane (parallel to the optical table) in order to generate
azimuthal polarization.
A schematic diagram of the elements needed for the generation of the azimuthally polarized
beam, is shown in Figure 3.1.
 In order to test the quality of the unconventional polarization generated, it was used a program
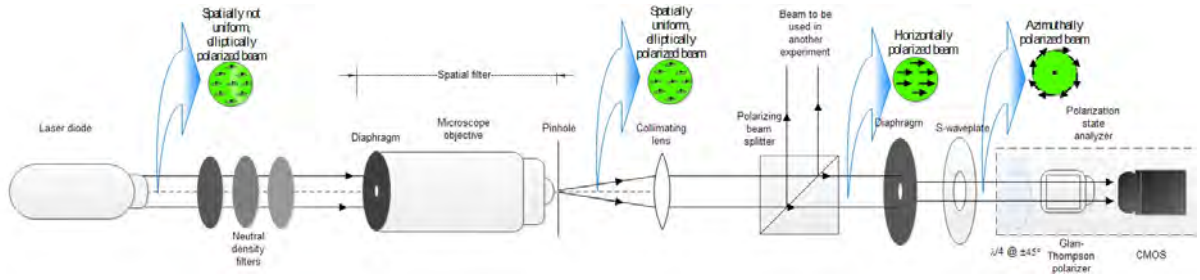
Figure 3.1: Schematic diagram showing the needed elements and its disposition in order to prepare the azimuthally polarized beam.

developed by our group (GIPYS at CIO, Mexico) that follows the Spatial Average Symmetry (SAS) metric, proposed by the head of our group (Espinosa-Luna et al., 2017). Basically, the SAS measures the spatial average values associated to each Stokes vector. If the beam has associated axially-symmetric polarization components, then the SAS associated to the beam provides a Stokes vector with values corresponding to the unpolarized light. On the other hand, if there is not axial-symmetry, the SAS numerical value indicates which polarization is predominant within the beam under analysis.

The computational algorithm, that was developed using the Matlab program, can be seen in Appendix C.3 and provide us the Stokes parameters in form of images and also as spatially averaged numerical values.

Once the Stokes parameters in images and numerical values were checked and considered the best we can obtain with our experimental resources, we proceed to the next step: the mode converters. The modes associated with each mentioned polarization for the azimuthally polarized beam generated can be seen in Figure 4.1 in Chapter 4. The corresponding Stokes parameters in images are shown in Figure 4.2 in the same Chapter.

3.2.   Implementation of the mode converters

As was explained in Chapter 2, besides the mode converter C (MMC), which is air, the system employs another two mode converters: one called π mode converter (which acts similar to a half-waveplate, rotating the $HG_{\pm 45°}$ modes to $HG_{10,01}$ modes) and one named $\pi/2$ mode converter (which acts similar to a quarter-waveplate, transforming LG modes to HG modes and vice versa). The three configurations affect only the spatial distribution of the mode, leaving the polarization unchanged. From these later two configurations, the one that is more troublesome is the $\pi/2$ configuration, since it also requires the beam to be mode-matched to the converter, unlike the π configuration, which works with a collimated beam of light.

For the mode-matching process, it was used a $f = 500$ mm doublet lens, which was the one that best matched our conditions. According to the theory presented in Chapter 2, when doing the calculations for our optical components, we needed a lens of focal length of about 1250 mm when the diameter of the input collimated beam was 5 mm ($\omega_{01} = 2.5$mm), but, when the beamwaist of the beam is reduced, the focal length of the needed mode-matching lens also decreases, as can be clearly seen from Equation 2.48 in Chapter 2.

For our optical components specifications, we found a perfect theoretical agreement between the minimum focal length of the mode-matching lens needed and the lens we had available when the beamwaist of the input collimated beam was 1 mm. The calculation of this parameter is shown in

Rayleigh Range, z_R	$z_R = (1 + 1/\sqrt{2})f_{cyl} = (1 + 1/\sqrt{2})24{,}93mm = 42{,}56mm$
Beamwaist produced at the $\pi/2$ mode converter, ω_{02}	$\omega_{02} = \sqrt{\lambda z_R/\pi} = \sqrt{532E^{-9}(42{,}558E^{-3})/\pi} = 84{,}893\mu m$
Minimum focal length required for the mode-matching lens, f_0	$f_0 = \frac{\pi}{\lambda}\omega_{01}\omega_{02} = \frac{\pi}{532E^{-9}}(1E^{-3})(84{,}90E^{-6}) = 500mm$

Table 3.1: Mode-matching related parameters for our optical system

Table 3.1, which also shows the Rayleigh range (z_R) and the beamwaist generated at the center of the $\pi/2$ converter (ω_{02}). The inclusion of the diaphragm help us to correct any small deviation in the theoretical values of the optical components by experimentally adjusting the radius of the input beam (the ω_{01} parameter) until we observe the best mode conversion.

The procedure to set the $\pi/2$ converter was the following:

- We placed and aligned the $f = 500$ mm doublet (mode-matching lens) after the S-waveplate, leaving a considerable space in order to be able to place temporal optical elements, like polarization state generators/analyzers and the camera. We need this space also to place the sample under test later on.

- Since we ran out of space in the optical table, we redirected the light with 2 auxiliary mirrors, as it is shown in the Figure 3.3.

- With the help of the camera, we determined experimentally the position of the focal length of the doublet.

- We measured the distance from the second auxiliary mirror to the camera sensor. At this distance will be positioned the center of the $\pi/2$ converter.

- We made a reference screen tool with millimeter paper taped on a cage plate. We used this very often in the alignment of the components of the system.

- The cylindrical lenses were placed in their rotatory mountings. Before securing them, we looked at our screen through the lens in order to align the plano axis vertically in the mounting (see Figure 3.2 for plano axis reference). The lens was then fixed. We did the same for both lenses.

- The mountings were placed into a post and then into a post holder. Then, 4 engraved bars were fixed to the mounting.

- The mounting was placed momentarily after the laser, which sends a collimated beam. We slide our screen through the engraved rods in order to find experimentally the focal distance of each lens. We established in a more precise way the direction of the plano axis of each lens also.

- Once we had fixed our references, we kept just one lens in its post holder and attached the other through the engraved rods.

- We adjusted the rotatory mountings at the desired distance ($f\sqrt{2}$) and the desired angle ($45°$) for this configuration.

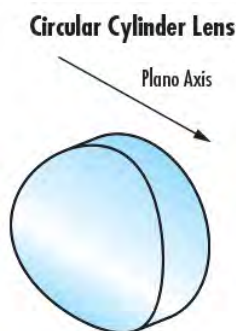- We placed the lenses so that the focal point of the doublet was at the center of the system.

Figure 3.2: Reference figure for the cylinder lens. Taken from Edmund optics page: [https://www.edmundoptics.com/resources/application-notes/optics/considerations-when-using-cylinder-lenses/]
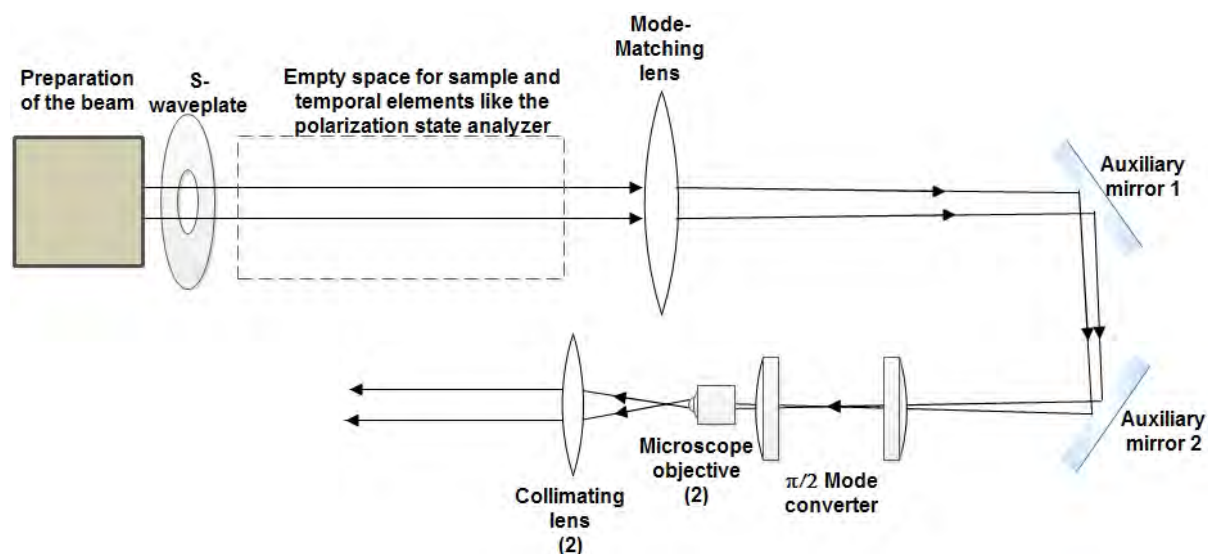

Figure 3.3: Schematic diagram showing the needed elements and its disposition in order to mount the $\pi/2$ mode converter. The preparation of the beam refers to Figure 3.1

- Carefully, we aligned the system so that the beam after the second mirror was impinging in and propagating through the center of the cylinder lens system. This step is very important and must be done precisely since any misalignment can cause, not only deviation of the beam but also important errors in the mode conversion.

- In order to probe the correct operation of the mode converter, we sent a Laguerre-Gaussian mode to the converter. To do this, we placed a $\lambda/4$ waveplate with its fast axis at $\pm45°$ with respect to the horizontal right after the S-waveplate and then a Glan-Thompson polarizer with its transmission axis at $0°$ with respect to the same reference. Notice the beam then had a donut shape and was horizontally polarized.

- If the process was correctly done, an HG_{10} or an HG_{01} mode can be seen after the converter.

- Finally, the converted beam was collimated with the use of a 10x Microscope Objective and a $f = 100$ mm doublet.

A schematic diagram showing the components for this stage is shown in Figure 3.3.

As previously discussed, this configuration of the mode converter is more difficult to assemble than the π configuration, since it requires more optical elements to work correctly. Any misalignment or error in any parameter selected can lead to an incorrect conversion or a non-conversion
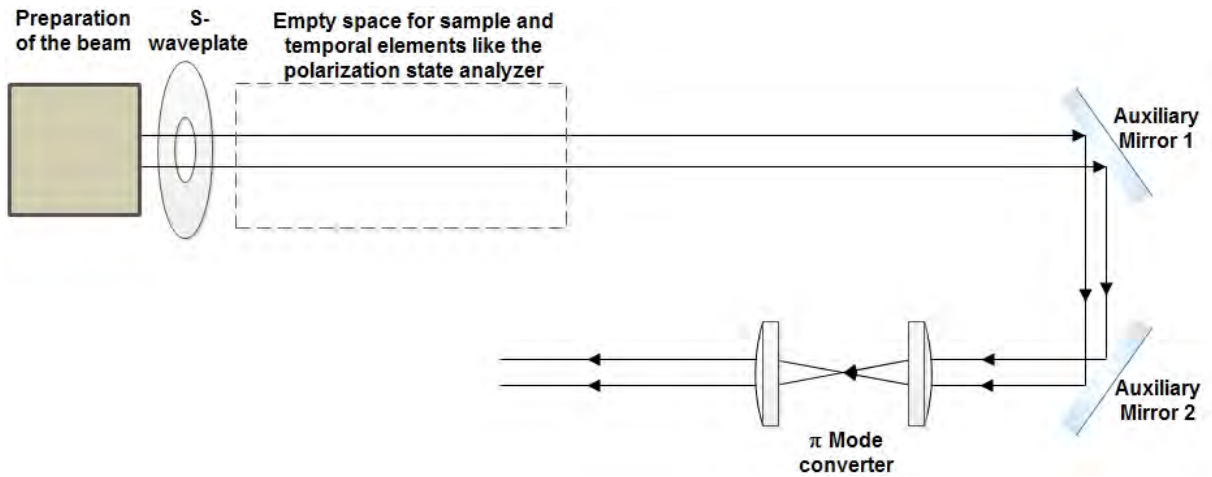
Figure 3.4: Schematic diagram showing the needed elements and their disposition in order to mount the π mode converter. The preparation of the beam refers to Figure 3.1

at all. Our best results are shown in Figure 4.3, Chapter 4 and our observations and conclusions about this process are discussed in Chapter 5.

For the π configuration, it is sufficient to take out the doublet (since this converter works with collimated light), change the distance between cylinder lenses to $2f$ and set their angles to 22,5°. Since the system of lenses now is in the $2f$ configuration, the emerging beam is collimated and there is no need for a collimation system, so we take out these components also leaving the rest of the components in their previous positions, as shown in Figure 3.4.

To check the correct performance of the π converter, we sent a HG diagonal beam with ±45° polarization to the system. When properly set, an HG_{10} or HG_{01} mode can be seen after the collimating system.

Notice neither the $\pi/2$ nor the π converter affect polarization; they just affect spatial distribution. So, another way to check for correct performance without the use of a polarization state selector after the s-waveplate, is to use a polarization state analyzer after the converter. We originally sent a donut-shape beam with azimuthal polarization, which has associated a Hermite-Gaussian shape horizontally and vertically oriented for vertical and horizontal polarizations, respectively, Hermite-Gaussian shape with ±45° orientation for ∓45° polarization and Laguerre-Gaussian (donut) shape for circular right and left polarizations, (as can be seen in the experimental images of Figure 4.1). So, after the π converter, we expect to see HG modes oriented at ±45° for horizontal and vertical polarization; HG modes horizontally and vertically oriented for the ±45° polarization and donut-shape for circular right and left polarizations.

When using the $\pi/2$ converter, we expect to see donut-shape for horizontal and vertical polarizations, the original Hermite-Gauss at ±45° for ∓45° and Hermite-Gaussian horizontally and vertically oriented for circular right and left polarizations.

These expected experimental results can be seen in Figure 4.3, Chapter 4.

3.3.   Implementation of the mode beam splitter

As explained in Chapter 2, in order to have the Modified Mach-Zehnder Interferometer (MM-ZI)working as mode-beam splitter, it is required to have a phase difference of π between the arms. Due to the low coherence of our laser source, (about 1.8 mm according to estimations of the Thor-
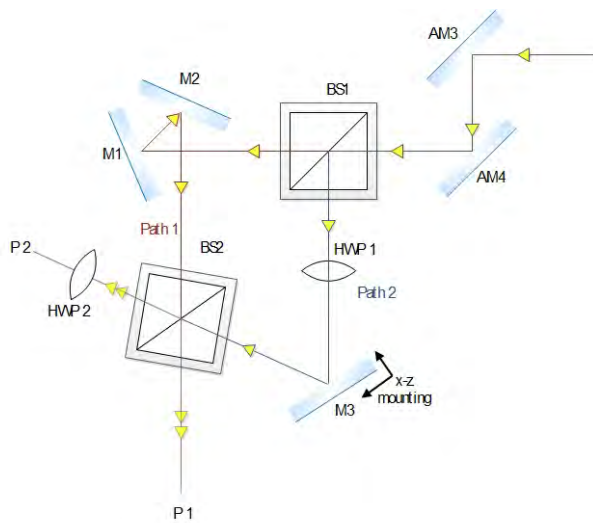
Figure 3.5: Schematic diagram of the mounted modified Mach-Zehnder interferometer (MMZI). BS≡Beam Splitter, M≡Mirror, AM≡Auxiliary Mirror, HWP≡Half waveplate, P≡Port.

labs technical support), it was necessary to compensate the geometrical path difference between paths. This was done displacing the single mirror from the 1rst beam splitter. This change made necessary to slightly rotate the 2nd beam splitter, in order to have both beams interfering. A schematic diagram of the mounted MMZI is shown in Figure 3.5.

As can be intuited, this configuration is even more complicated to assemble than the conventional one, because of the break of symmetry and the use of additional optical elements. So, in the process of its assembly, several things must be taken into account:

- The cube beam splitters (BS) introduce a slight deviation in height of the transmitted and reflected beams, being bigger the difference as more deviated is the entrance beam (say, it is tilted in any direction), even if the beam is entering at the center of the BS. In order to minimize this deviation, 2 auxiliary mirrors were placed at the entrance of the interferometer in order to assure a well aligned entrance beam.

- The position of the third mirror was fixed taken as reference the geometrical path of the arm with the two mirrors (Path 1), so we have approximately equal geometrical paths.

- Once the mirrors were placed and centered, the tilt of the single mirror was adjusted to conserve the height of the reflected beam constant. By tilting the 2 mirrors in the other arm, the height of the corresponding beam was adjusted to be the same. This helps to have beams without tilt between them; a necessary condition to have interferograms without fringes (thanks to Dr. Zacarías Malacara Hernández for his scientific support with technical aspects concerning the interferometer).

- The second beam splitter was centered and rotated in order to have the two beams interfering. The difference in height in the interfering beams was corrected with a tilt of the BS. Notice that, in order to have interferograms without fringes, the BS has to be placed accurately so both beams enter at the center of each side of the BS.

- Depending on the available mountings for each element, it can be easier to slightly displace and rotate the 3rd mirror in order to have no fringes. Once we have reached this condition, the two half wave-plates (HWP) are placed and aligned. In order to properly set the direction of their fast axis, a Glan-Thompson polarizer with its transmission axis at 0° was placed at the entrance of the interferometer and an identical Glan-Thompson polarizer was placed at one output port with its transmission axis at 90°. The HWP of that port was

rotated in order to have a minimum transmission. The procedure was repeated at the other port. This step help us to compensate minor changes in polarization caused by reflection in the mirrors, thus producing a better visibility of the interferograms.

- When doing all this steps correctly, the orthogonal modes HG_{10} and HG_{01} can be seen at the output ports when an azimuthal beam is entering the interferometer. Notice, because the split of the modes is done according to the phase difference between the paths, the modes can be seen in one or the other port and vary according to change in pressure, temperature or air flow in the interferometer. Even though, the outputs are stable enough in laboratory conditions, which make measurements possible when being careful not to cause variations during data collection.

Experimental images of the outputs obtained when sending an azimuthal beam to the interferometer, can be seen in Chapter 4 along with their Stokes parameters displayed as images and spatially averaged numerical values.

Chapter 4

Results, Analysis and Discussion

I was taught that the way of progress is neither swift nor easy.

Marie Curie

SUMMARY: We present the images obtained in each stage of the arrangement and their corresponding Stokes parameters, both in image and numerical representations, provided by the spatial average symmetry (SAS) code. Each set of images is analyzed in order to present the brief discussions that led us to the conclusions shown in Chapter 5.

4.1. Results for the generation process of the azimuthal beam

As mentioned in Chapter 3, the first big step in our experimental setup was to generate the best azimuthally polarized beam, since it will be our main tool to test our sample. Once the output from the laser diode was spatially filtered, collimated, horizontally polarized, passed trough the iris diaphragm and sent to the S-waveplate, we checked for its polarization. For this purpose, we employed a polarization state analyzer (described in Chapter 2) to obtain the polarimetric analysis of the azimuthally polarized beam of light, which is shown in Figure 4.1. The images correspond to a beam of 2 mm in diameter. We used 3 neutral density filters at the laser output and set the exposure time in the camera to 0.31 ms in order to avoid overexposure.

Observe the images obtained in Figure 4.1 when the polarization state analyzer (PSA) is used as a linear polarizer filter (Figures 4.1a-4.1d), it allows the transmission of the intensity distribution along its transmission axis and obstructs it along its extinction axis. For example, Figure 4.1a shows total attenuation occurs at the horizontal direction, where the incident electric field components are perpendicular to the analyzer´s transmission axis, while a maximum intensity is appreciated at the vertical direction, where the electric field components are parallel to the transmission axis. The previous reasoning explain why the Figure 4.1b is orthogonal to Figure 4.1a and also why Figures 4.1c and 4.1d are also orthogonal each to the other. The sense of the azimuthal polarization is determined through the analysis of both, circular right- and left-handed polarizations, respectively; in this case, Figures 4.1e and 4.1f show there exist a similar contribution from both polarizations.
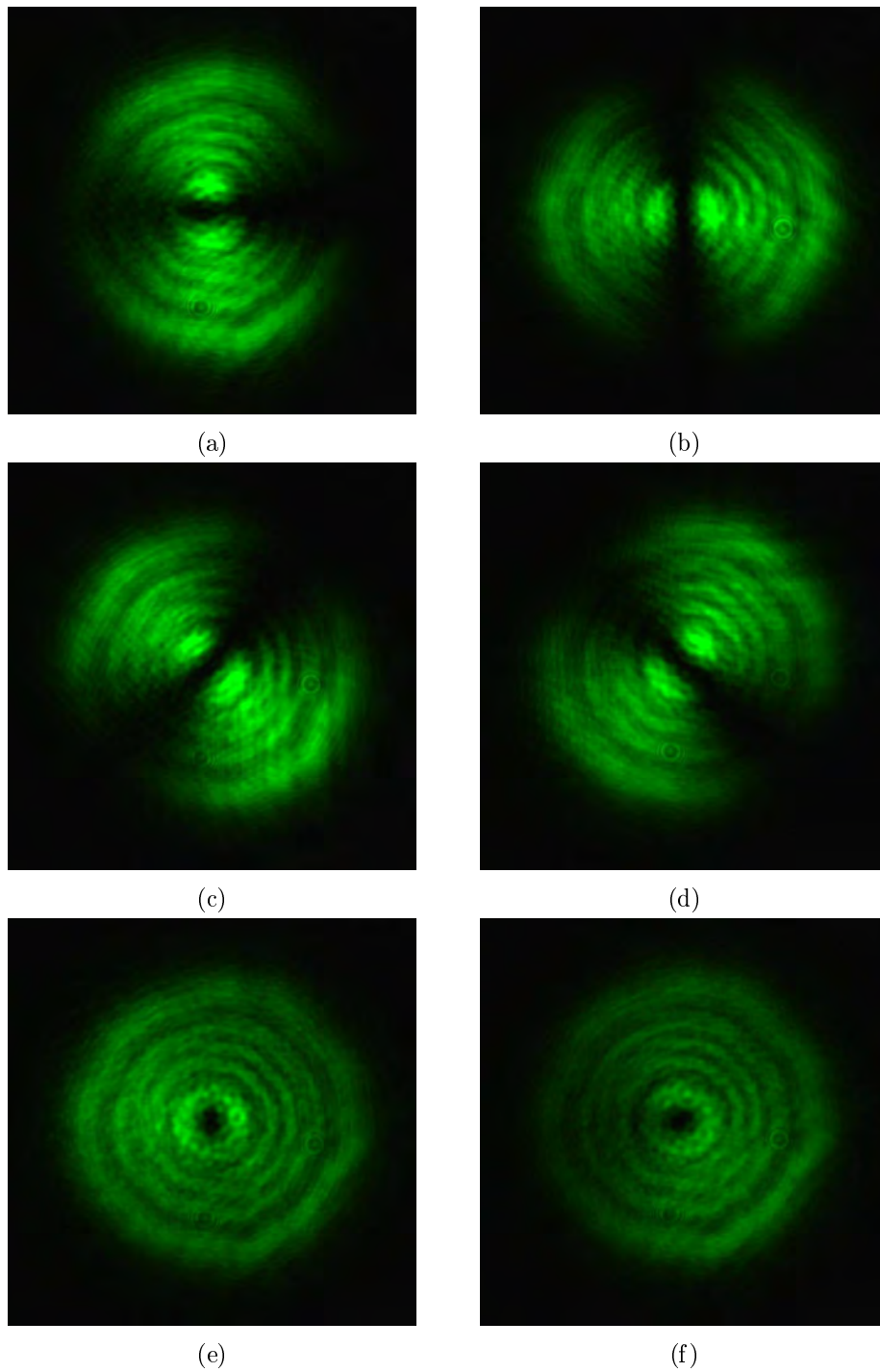
Figure 4.1: Modes obtained from the azimuthal beam when only a specific type of conventional polarization is selected. a)Linear Horizontal. b) Linear Vertical. c)Linear at 45°. d)Linear at −45°. e)Circular right and f)Circular left polarization states.

It is very important to take into account that the experimental images filtered with the polarization state analyzer (PSA) provide information of the type and spatial distribution of the polarization contained within the beam under study, where a complete analysis through the Stokes vector is required in order to determine the polarimetric and spatial behavior. In this sense, the application of the intensity measurements according to Equation 2.30 provides the most complete information, where I_0 is associated to Figure 4.1a, I_{90} to Figure 4.1b, I_{45} to Figure 4.1c, I_{135} to Figure 4.1d, I_R to Figure 4.1e, and I_L to Figure 4.1f. The images shown in Figure 4.2 are depicted by using varying color tabs, where the red is associated to positive values and the blue is associated to negative values. Even when Figure 4.2 provides spatially-resolved information of the Stokes parameters, it lacks from information related with the global or total tendency associated to the polarization state, as a whole. This means, in practice, Figure 4.2 provides only qualitative information. Fortunately, there exist a very simple and logic procedure to become quantitative the information provided by the image Stokes vector (Figure 4.2). The spatial average symmetry (SAS) metric, is a recently published proposal by our GIPYS Group, which provides a numerical value associated to each Stokes image (Espinosa-Luna et al., 2017); it is obtained by computing the spatial average value associated to each Stokes image. In this case, Figure 4.2 is associated to the best azimuthal beam generated in this work, and even when it is very close to the ideal expected result for a perfectly generated azimuthal beam (spatial average Stokes numerically equivalent to an unpolarized state)[*], the results obtained:[1 0.0455 0.0360 0.1187]$^\intercal$, show a slightly tendency to a global behavior similar to an elliptical right-handed polarization state.

After a lot of times trying to improve the quality of the beam generated, we have arrived at the conclusion this is the best result obtainable from the experimental conditions employed, including the own capability of the S-waveplate device.

---

[*]Due to the fact that the azimuthal polarization globally does not have a tendency for a specific conventional polarization, we expect the same Stokes vector as the one for unpolarized light: [1 0 0 0]$^\intercal$. Here $^\intercal$ means transpose.
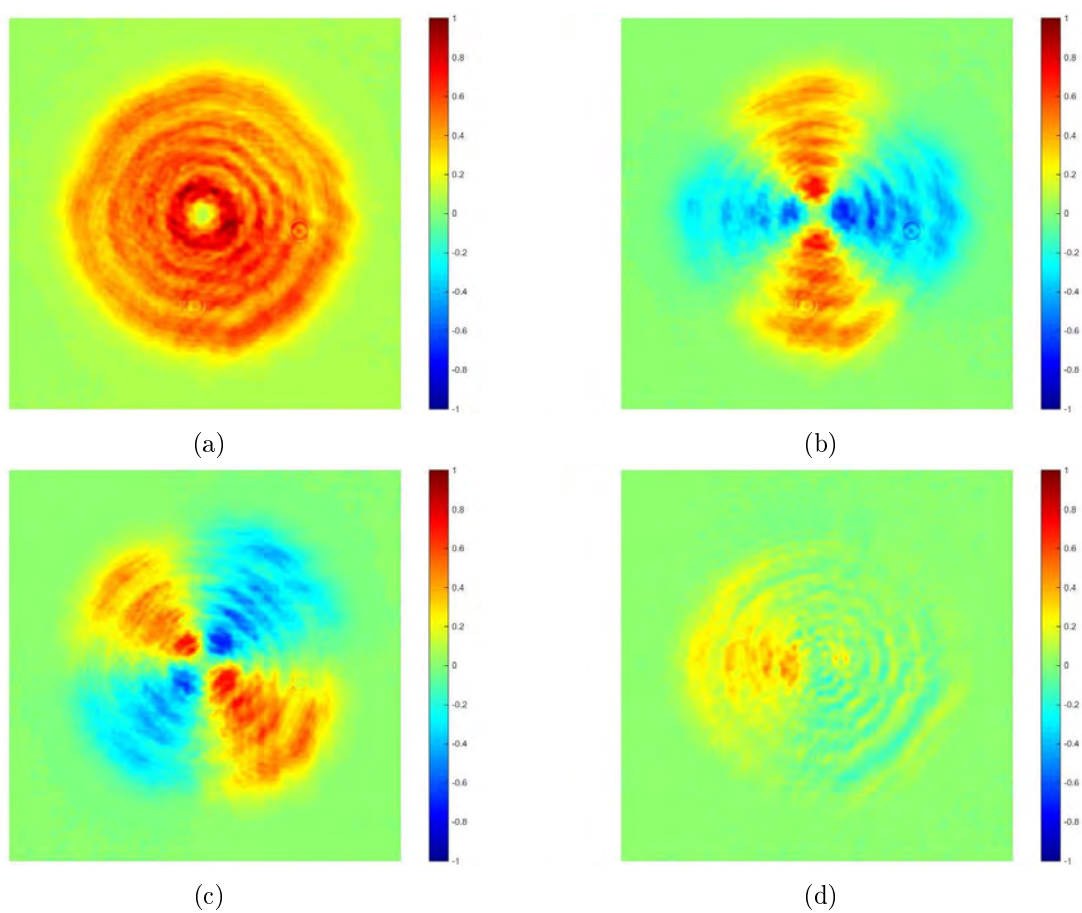
Figure 4.2: Stokes parameters in images for the azimuthally polarized generated beam. The Spatial Average Symmetry (SAS) provides the numerical values: $[1\ 0.0455\ 0.0360\ 0.1187]^{\intercal}$.

4.2.   Results for the mode converters

As explained in the Theoretical Section (2), the complete arrangement makes use of 3 mode converters:

- Mode converter A (**MCA**). $\pi/2$ converter. Cylinder lenses separated $f_{cyl}\sqrt{2}$, with their axis rotated at 45°.

- Mode converter B (**MCB**). π converter. Cylinder lenses separated a distance of $2f_{cyl}$ with their axis rotated at 22,5°.

- Mode converter C (**MCC**). Air.

We will show here the results obtained when the mode converters A and B are implemented and tested for our azimuthal beam, which is the second big step in our experimental procedure.

One helpful idea when mounting the mode converter A or B, is to select one specific mode from the azimuthal beam in order to directly check for the resultant conversion, this allows to make some fine adjustments if needed. For example, when placing the MCA, we select a LG mode from our probe beam and see if we obtain the corresponding HG mode. We can do this by placing a QWP with its fast axis at ±45° followed by a horizontal polarizer right after the S-waveplate.

When placing the MCB, we send a diagonal HG mode by placing a polarizer with its transmission axis at ±45° after the S-waveplate and then we verify the obtention of the HG horizontal or vertical modes at the output of the converter.

Once we have the best conversion, we remove the auxiliary polarizing elements and test the converters for the azimuthal beam. For this, we compute the Stokes parameters using the SAS method, employing the PSA explained before. The modes obtained when doing the polarimetric analysis are shown in Figure 4.3 for the $\pi/2$ converter and in Figure 4.5 for the π converter. The Stokes parameters in images are also shown in Figures 4.4 for the $\pi/2$ converter and in Figure 4.6 for the π converter.

4.2.1.   Results for the MCA: $\pi/2$ converter

From Figure 4.3, we can see clearly that, after passing through the $\pi/2$ converter, the modes originally associated with horizontal/vertical polarizations and the ones originally associated with circular right and circular left polarizations, are now interchanged, in complete concordance with the expected functioning of this converter. Even more, when computing the Stokes vector (Figure 4.4), we can see that the azimuthal polarization is maintained; since the beam still does not show a tendency to any specific polarization. In this way, we have managed to work with the spatial degree of freedom without change the polarization distribution of the beam.

Even though in Figure 4.3 it can be seen a markable degradation in the symmetry of the modes as compared with the original ones, from all our tested configurations (different mode-matching lenses, diaphragm apertures and tons of alignments), we consider these as our best results. In any other cases the geometry of the Hermite-Gaussian modes were departing too much from the lobes geometry and showed very distorted and rotated forms. In the worst cases the shape of the beam as seen right at the output of the converter was too far from the donut-shape, tending more to a prolate shape and getting more flattened with the propagation of the beam. This change in shape with beam propagation caught our attention and led us to investigate more about its possible causes. We found that any mistake in the mode-matching process can led to a mixing of modes of zero and 1rst order, as is shown in Anderson (1984). The resulting mixed beams are in general unstable, which causes the continuous change in shape.

Anderson in his article makes a separate analysis for 4 possible tiny maladjustments in the process: Transverse displacement in the x direction (i.e. the beam does not propagate through the center of the system but laterally displaced from it), tilt through an angle (i.e. the beam does not propagate parallel to the axis of the system, but it forms an angle with it), waist size mismatch (the input beam waist is a little bit larger than the system beam waist) and axial waist displacement (the input beam is not focused at the center of the system). In each of these cases, the result is a beam with coupled zero and first order modes. That is why we emphasize that this process must be done very carefully in order to achieve the searched results. Certainly, there are a lot of factors to take care to achieve proper mode-matching, and thus, the correct implementation of the $\pi/2$ converter. Aside from this fact, we can see from Figures 4.3 and 4.4 that we successfully converted a Hermite-Gaussian distribution to a Laguerre-Gaussian distribution (and vice versa) without altering its polarization state.

(a)

(b)

(c)

(d)

(e)

(f)
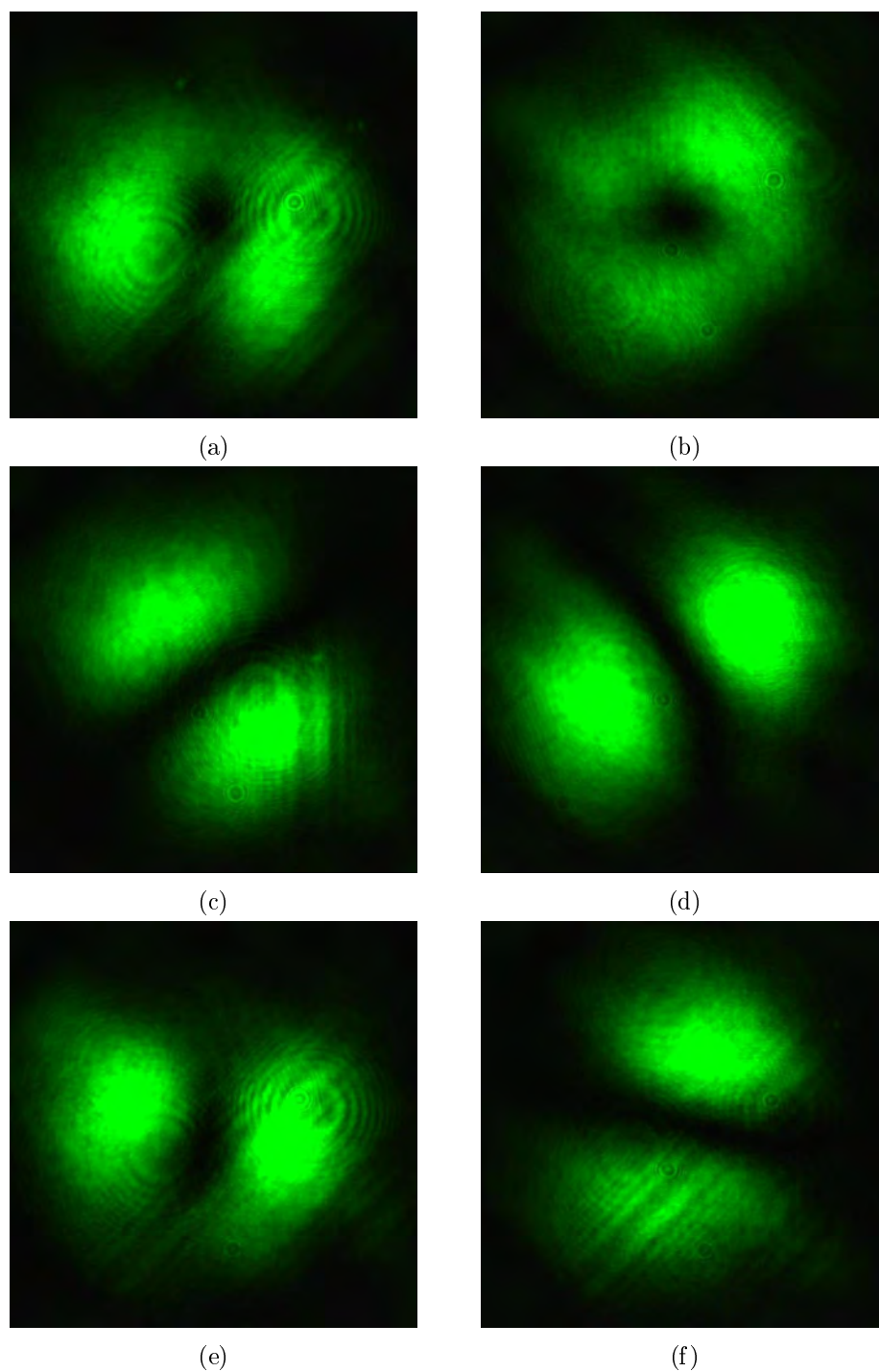
Figure 4.3: Modes obtained with a polarization state analyzer for the azimuthal beam after passing through the $\pi/2$ mode converter and the collimation system. The polarization states shown are: a)Linear Horizontal. b) Linear Vertical. c)Linear at $45°$. d)Linear at $-45°$. e)Circular right and f)Circular left polarization states. Exposure time of 1ms.
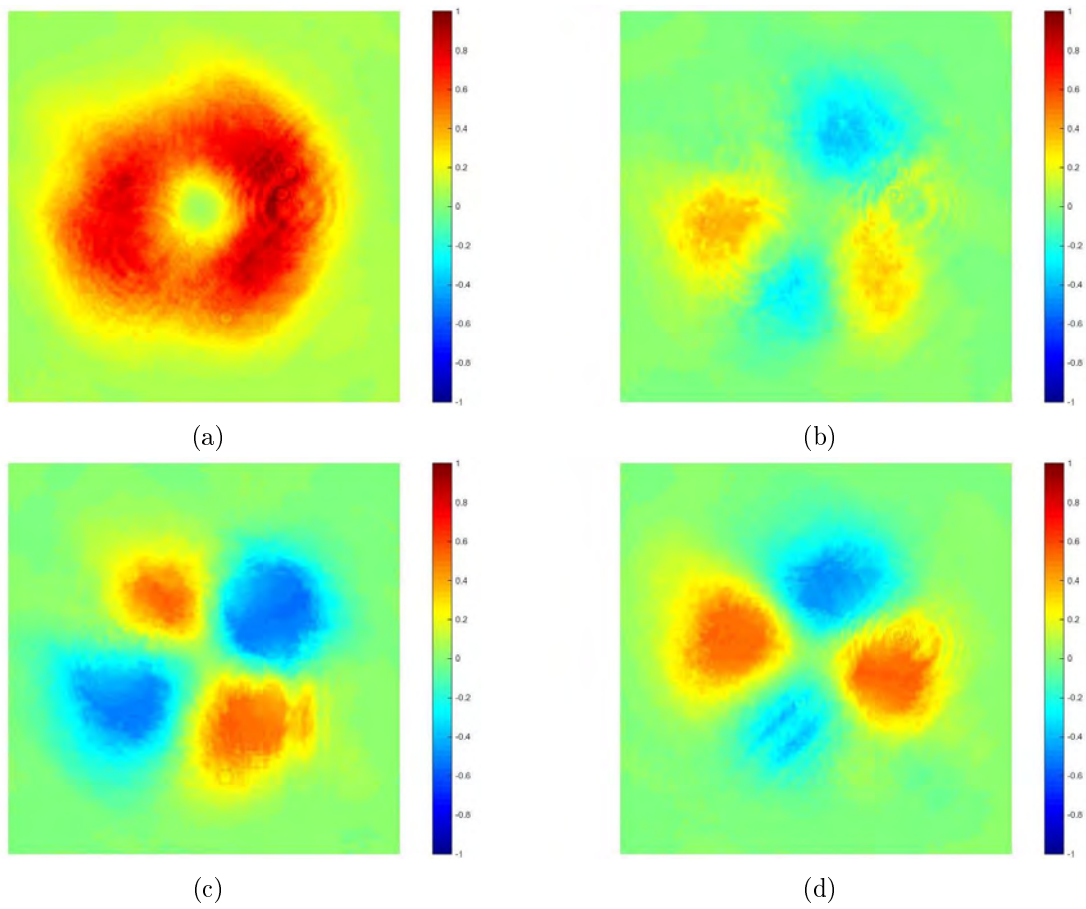
Figure 4.4: Stokes parameters in images for the azimuthally polarized beam after passing trough the $\pi/2$ converter and the collimation system. The Spatial Average Symmetry (SAS) provides the numerical values: [1 0.0259 -0.0542 0.0853]$^\intercal$.

4.2.2.   Results for the MCB: π converter

The results obtained for the π mode converter when using an azimuthal beam as an entrance, are shown in Figure 4.5. From these images, we can see that the spatial distribution for the horizontal/vertical and $\pm 45°$ polarizations is now interchanged with respect to the original distribution (the one for the incident azimuthally polarized beam, see Figure 4.1), while the circular polarizations maintain their Laguerre-Gaussian shape. This is exactly what we want from this converter. Notice also from the spatially averaged numerical values provided by the SAS code for this case, (at the description of Figure 4.6) that the beam globally still does not show a tendency to any conventional polarization, i.e. again we have worked with the spatial degree of freedom of the beam without alter its polarization state.
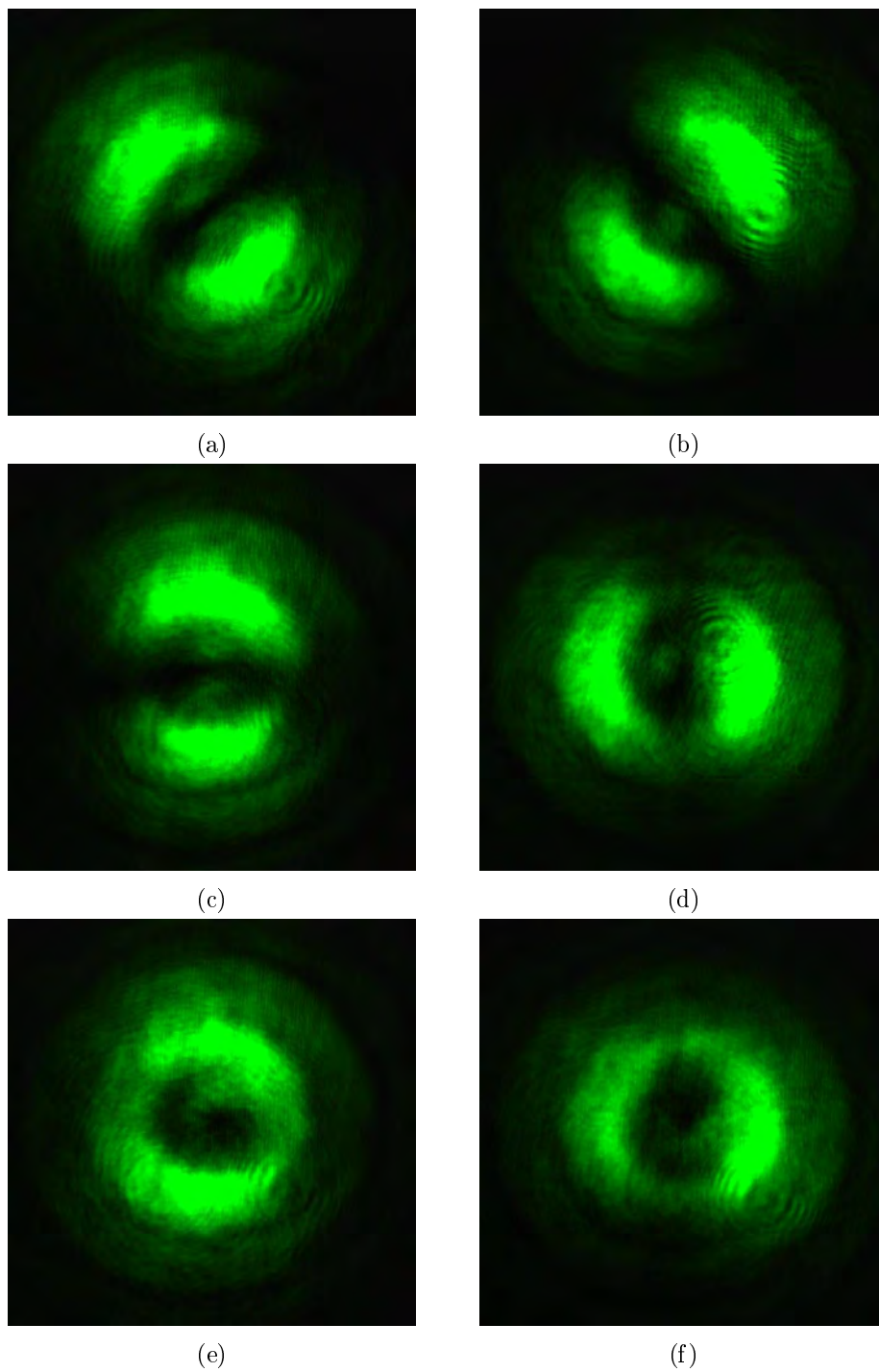
Figure 4.5: Modes obtained with a polarization state analyzer for the azimuthal beam after passing through the π mode converter. The polarization states shown are: a)Linear Horizontal. b) Linear Vertical. c)Linear at 45°. d)Linear at −45°. e)Circular right and f)Circular left polarization states. Exposure time of 0.5 ms.

(a)

(b)

(c)

(d)
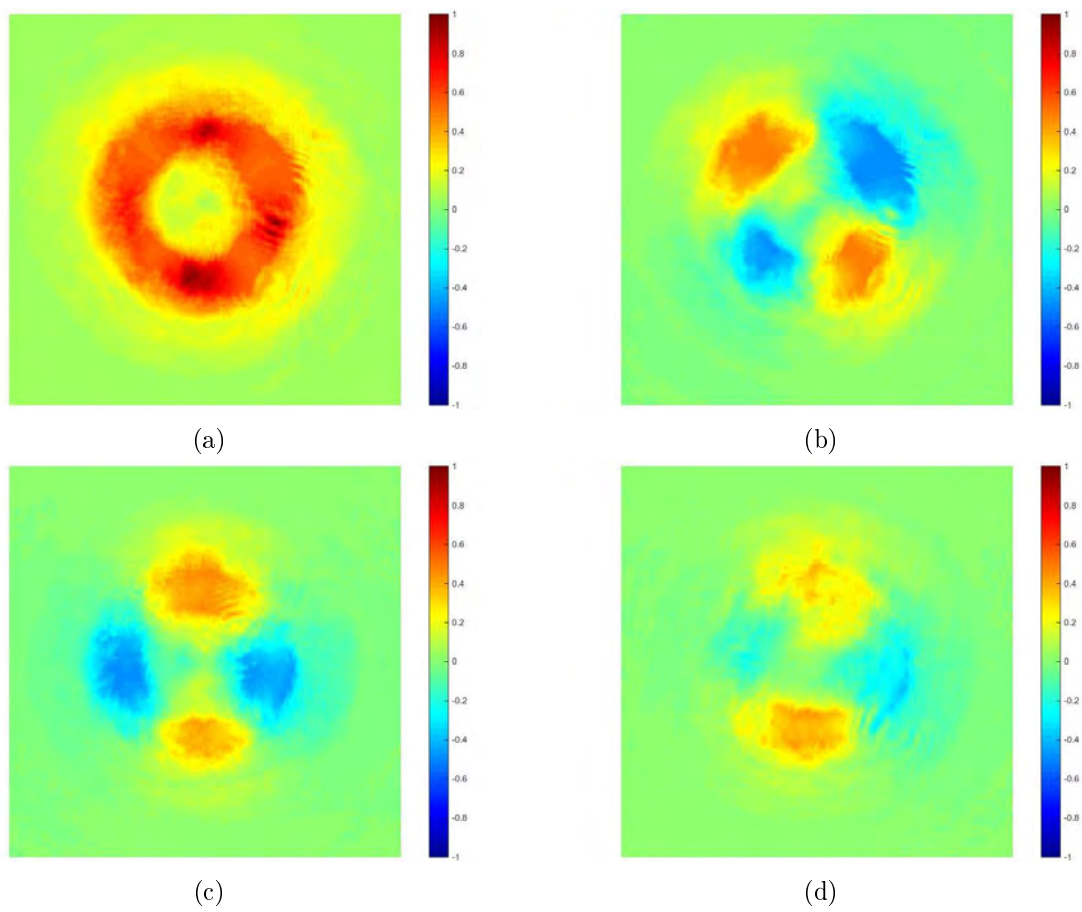
Figure 4.6: Stokes parameters in images for the azimuthally polarized beam after passing trough the π converter. The Spatial Average Symmetry (SAS) provides the numerical values: $[1\ 0.0198\ -0.0196\ 0.0975]^{\intercal}$.

4.2.3.   Results for MCC: Empty space (air)

The results for this mode converter correspond to the analysis of the azimuthal polarization generated, explained at Section 4.1 and Figures 4.1 and 4.2.

4.3.   Results for the mode beam splitter

The next step for the probe beam after passing through a mode converter, is to pass through the mode beam splitter (which is the modified Mach-Zehnder interferometer) in order to be separated in its horizontal and vertical mode components with orthogonal polarization.

This step is the most difficult part to achieve from all the stages in the arrangement and that is because the mode decomposition completely depends on the phase difference between the interfering beams, which has to be of π. As explained in Chapter 3, several things have to be taken into account in order to have the mode decomposition behavior of the interferometer. The main ones are:

- No fringes at all. This means that the orientation of the mirrors is the same among them and that we have the interferometer working with almost parallel beams (non localized fringes configuration). Any misalignment between the interfering beams will cause the occurrence of the fringes, so we can use them as an indicator to know when the beams are well aligned and when they are not.

- The visibility of the fringes has to be as clear as possible. In order to check this, we can place a microscope objective at the entrance of the interferometer in order to illuminate it with a divergent beam. In this case we will see circular fringes (personal communication with Dr. Zacarías Malacara Hernández). Because of the low coherence of our laser, some times this fringes are not very clear. We displace the third mirror with the micrometer screw until we reach the best visibility and then remove the microscope objective and re-align the interferometer for this new configuration.

- The phase difference between the arms of the interferometer must be of π. In order to check this, we use again the microscope objective and adjust the mirror in order to have a completely dark fringe at the center of one output and a completely bright fringe at the center of the other one.

When all these conditions are fulfilled, we will see an HG_{10} mode in one output port and an HG_{01} mode in the other.

Another thing to take care about is the polarizing behavior of the interferometer, this means that, depending on which mode converter the beam had passed through before, the output modes of the interferometer can exhibit:

- Horizontal/Vertical polarization for MCC (Air).

- Linear at $\pm 45°$ for MCB (π converter).

- Circular right/left for MCA ($\pi/2$ converter).

In order to check for this, once the interferometer is aligned and working as mode beam splitter, we select an HG_{10} or HG_{01} mode with a desired polarization and send it to the interferometer. If we observe a strong attenuation of one of the output beams with respect to the other, then we proceed to make the measurements.

4.4. Data polarimetric analysis

The final step in order to obtain the images from which the Mueller matrix is computed, is to place a PSA at each of the output ports of the interferometer. The PSAs are identical and are disposed in order to analyze the same state of polarization at each time. A CMOS camera is used to register the resultant beam of each port.

Notice that due to the extreme sensitivity of the interferometer to any change in the environmental conditions, it is necessary to check on a screen at one output port, the maintenance of the mode while taking measurements in the other.

We follow here the relationships proposed by Töppel et al. (2014) in order to find the Mueller matrix of our samples. These relationships, that are shown in Appendix A, make use of 4 specific analyzed states: {*Linear horizontal*, *vertical*, at $+45°$ and *circular left*}, which correspond to {*Linear horizontal*, *vertical*,at $+45°$ and *circular right*} in our convention used to describe polarization. Once the images had been taken, we proceed to process them using the code shown in the Appendix C.2 section.

We tested our system for 3 samples: Air, a commercial $\lambda/2$ waveplate and a commercial $\lambda/4$ waveplate. The interferometer was aligned for each mode converter and then used to measure each sample. The organization of results will be divided by blocks (results from the interferometer for each mode converter) for each sample and will be labelled indicating output port of the interferometer (P1 or P2), mode converter (MCA,MCB or MCC) and sample (1≡Air,2 ≡ $\lambda/2$, 3 ≡ $\lambda/4$). Of course, before testing the samples with our experimental arrangement, we first measured their phase retardation and determined the direction of their principal axis in order to have the appropriate reference when mounting them (we aligned them in order to have their fast axis at $0°$ so we have a simpler and familiar result when obtaining their Mueller matrices). The procedure followed in order to achieve this is explained in Appendix B.

Our results show a phase retardation of $161°$ for the case of the $\lambda/2$ WP (the ideal value for a HWP is $180°$) and of $95,2°$ for the case of the $\lambda/4$ WP (the ideal theoretical value for a QWP is $90°$), both results for a wavelength of $\lambda = 532nm$.

Once the retardation and the direction of the fast axis of the waveplates was established, we proceed to measure their Mueller matrices using the traditional ideal polarimetric arrangement (IPA) method, (see Section 2.1.3.2). These results are presented at the beginning of each corresponding Subsection.

4.4.1. Results for sample 1: Air

First we present the conventional results obtained for air when applying the IPA method. The resultant Mueller matrix for this case is shown in Figure 4.7. The numerical elements of the Mueller matrix were obtained averaging the corresponding image and normalizing to the average value of the M00 image element.

As can be seen from equation 4.1 and Figure 4.7, the obtained results are in perfect concordance with the theoretical ones, since they resemble to the identity matrix.

$$\mathbf{M}_{\mathbf{IPA}}^{\mathbf{Air}} = \begin{bmatrix} 1,0000 & -0,0045 & 0,0198 & -0,0078 \\ -0,0035 & 0,7926 & 0,0087 & -0,0447 \\ 0,0045 & -0,0093 & 0,7626 & -0,0049 \\ -0,0097 & -0,1264 & 0,0269 & 0,7755 \end{bmatrix} \tag{4.1}$$

One thing to take into account for the correct interpretation of these results (equation 4.1), is that the IPA method, as its name indicates, works considering ideal polarizing optical responses, i.e. waveplates that produce exactly a phase retardation of $180°$ for the HWP and $90°$ for the

QWP, and total transmission (attenuation) along the transmission (extinction) axis of the linear polarizers. We have measured the retardation of the waveplates that conform our PSA and PSG, at the wavelength we are working ($\lambda = 532$ nm), using the procedure explained in Appendix B, and we have found the values shown in Table 4.1.

The linear polarizers used are of the Glan-Thompson type, with extinction coefficients close to 100,000:1, which are some of the most reliable devices employed in polarimetric applications. We have verified they fulfill the null condition under the crossed condition, at the intensity values employed here.

Waveplate	$\lambda/2$ (1)	$\lambda/2$(2)	$\lambda/4$(1)	$\lambda/4$(2)
Retardance	166,48°	167,58°	100°	92,81°

Table 4.1: Phase retardation measurements for the waveplates that conform our PSG and PSA.
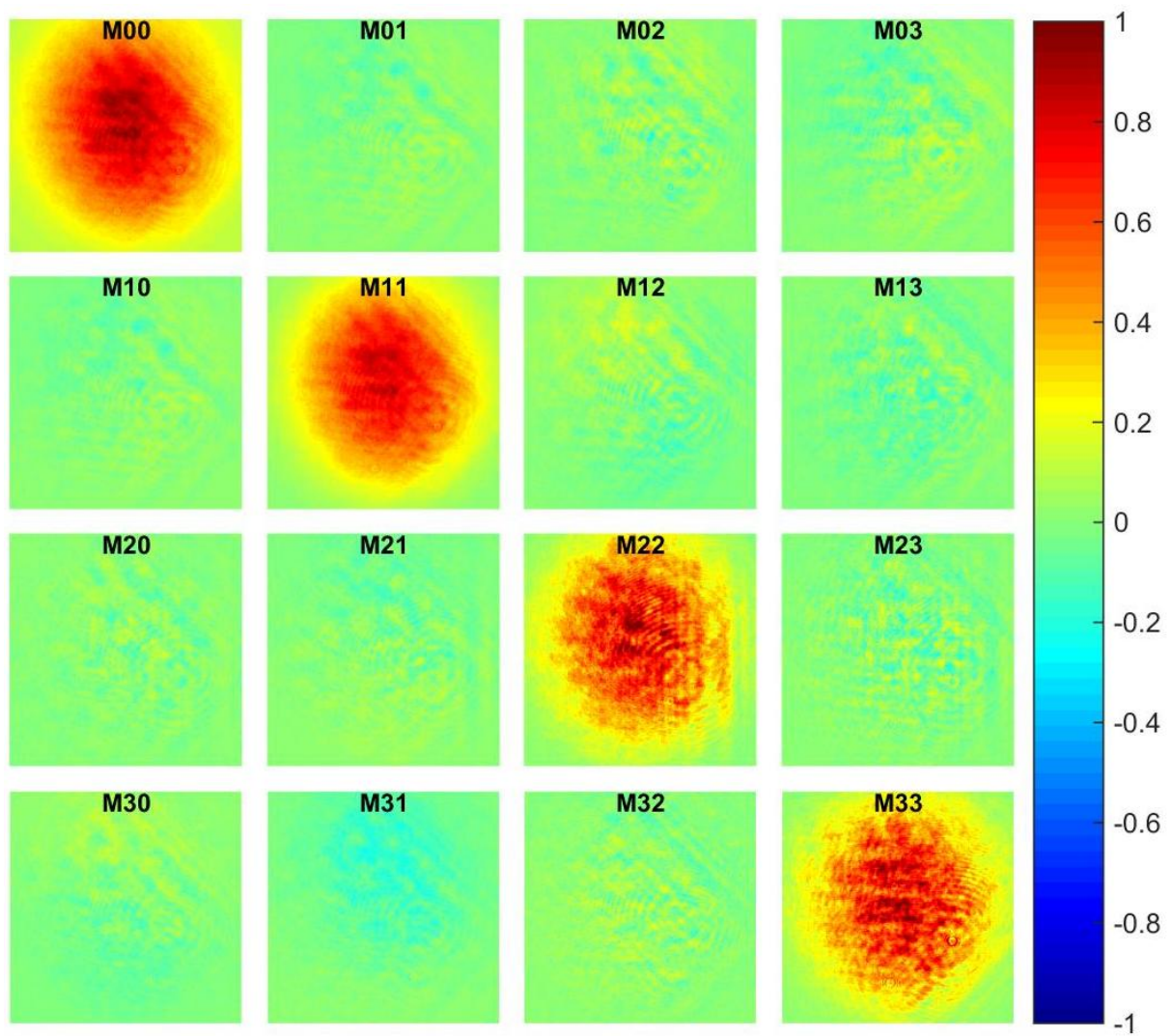
Figure 4.7: Experimental Mueller matrix for air using the IPA method

On the other hand, for unconventional polarization, we start by showing the images obtained from the MMZI for air, once that the beam has passed through the MCA, Figure 4.8. Using these images, we also analyzed the polarization of each output beam from the interferometer using the SAS code, the corresponding results for MCA, sample 1 (air) are shown in Figure 4.9.

The results for the MMZI MCB air are shown in Figures 4.10 and 4.11.

The results for the MMZI MCC air are shown in Figures 4.12 and 4.13.

Notice from the Stokes images and vectors given in Figure 4.9, that the beam at port 1 has a left handed polarization (the S3 parameter has a negative value), while the beam at port 2 has a right handed polarization (the S3 parameter is positive). The S2 parameter has also the opposite sign for each beam, indicating a tendency to $-45°$ linear polarization for the case when S2 is negative (beam at port 1) and to $45°$ linear polarization for the case when S2 is positive (beam at port 2). The S1 parameter indicate us the tendency of the polarization to be linear vertical for a - sign (beam at port 1) and to linear horizontal for a + sign (beam at port 2). From these results we can associate an elliptical left handed polarization for the beam at port 1 and an elliptical right handed polarization for the beam at port 2, showing that indeed, they have a tendency to be orthogonal. An important remark is that, in this case, the images show us that the vertical modes at port 1 have a more dominant presence for all Stokes parameters while the opposite case (horizontal modes) is true for the beam at port 2. This is the main difference with our original azimuthal polarized beam, who show a more balanced contribution of horizontal and vertical modes for each Stokes parameter (see Figure 4.2).
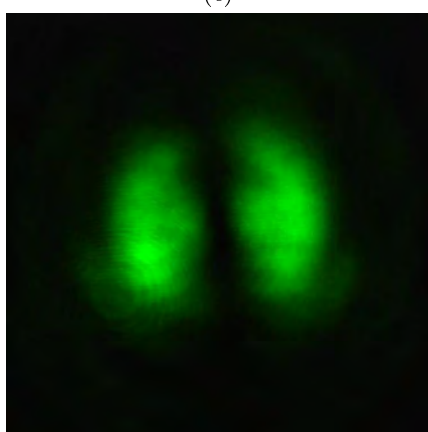
(a)

(b)

(c)

(d)

(e)

(f)

(g)

(h)

(i)   (j)

(k)   (l)
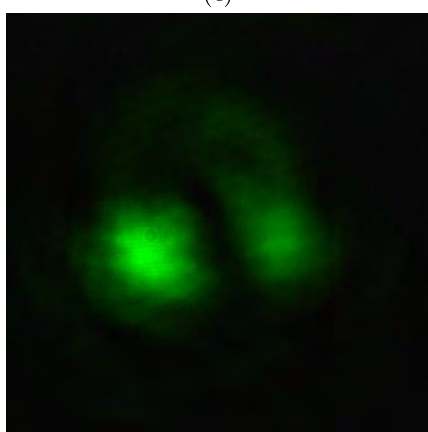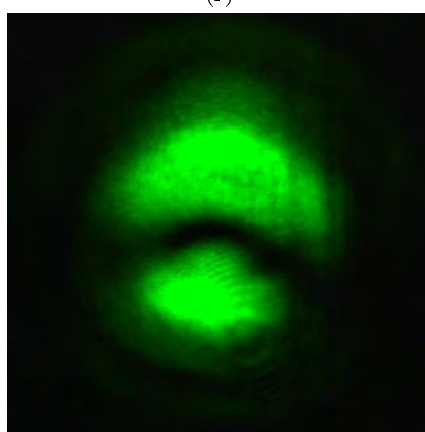
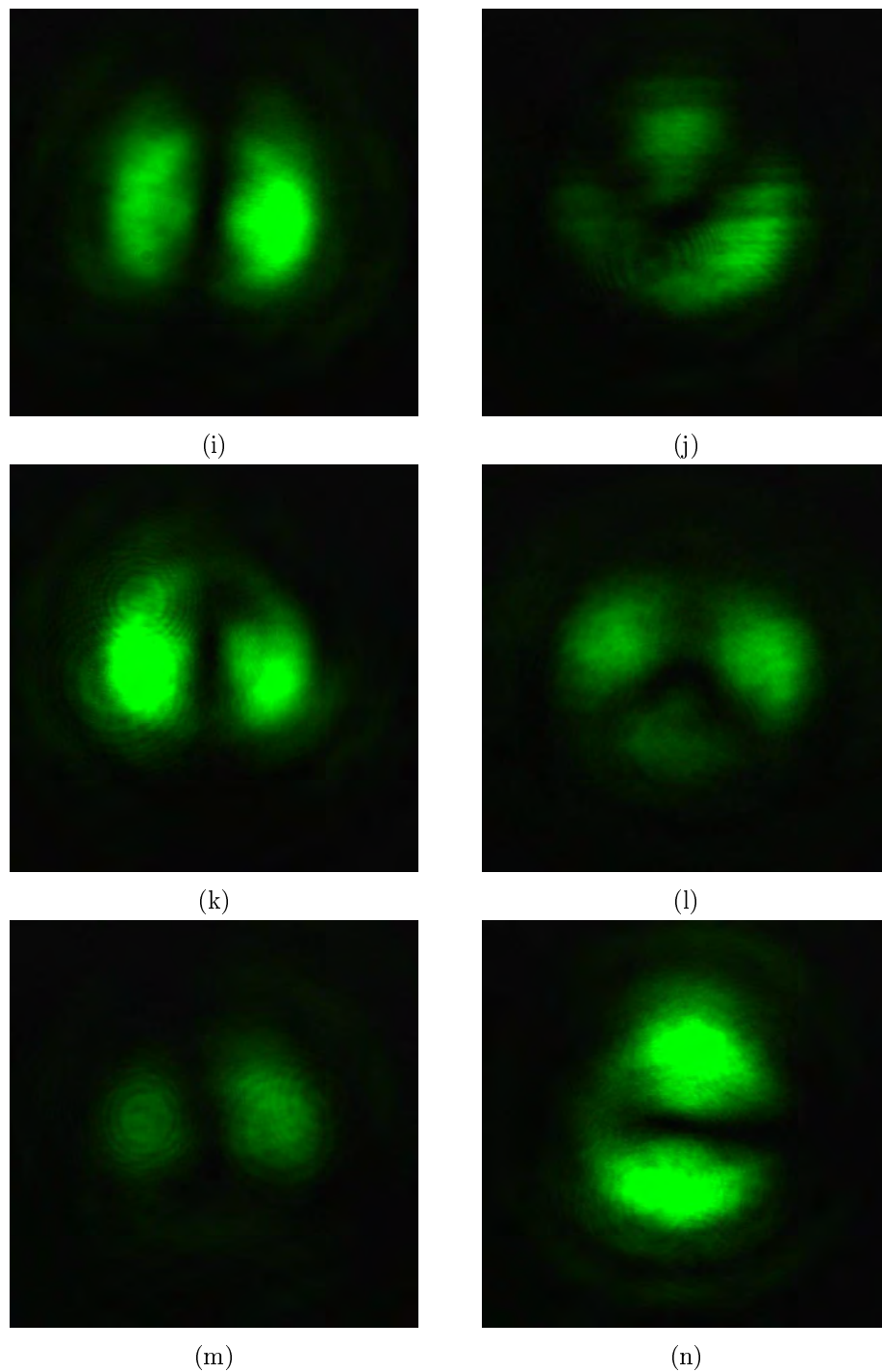(m)   (n)
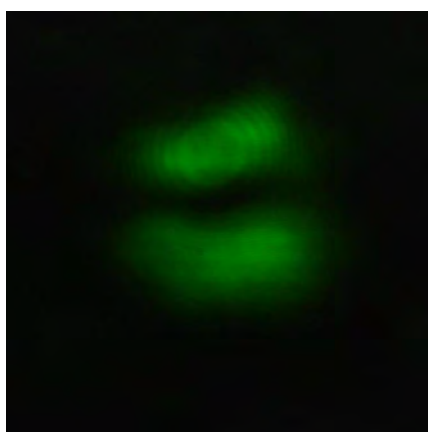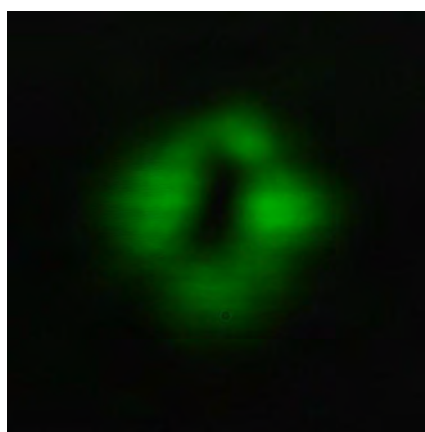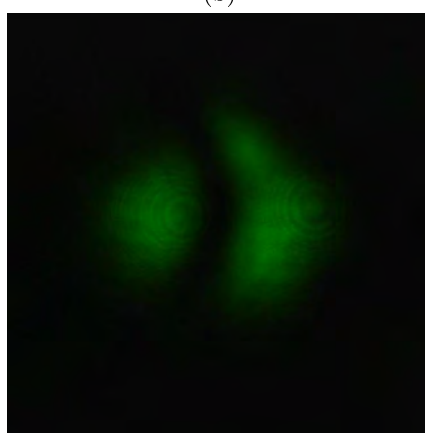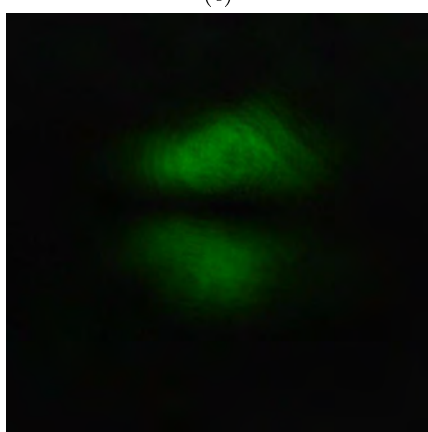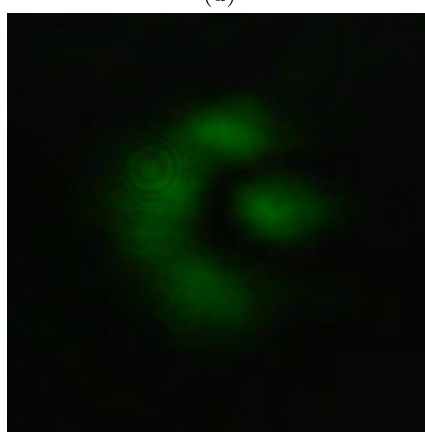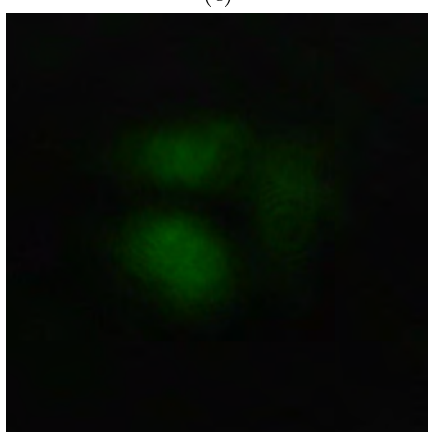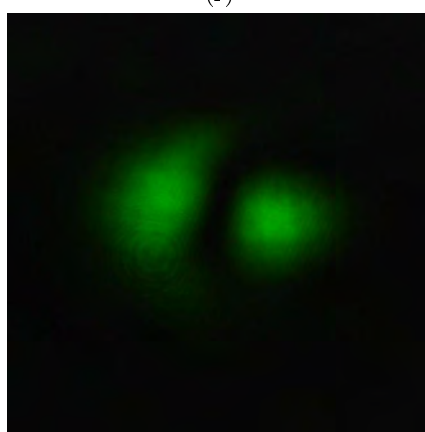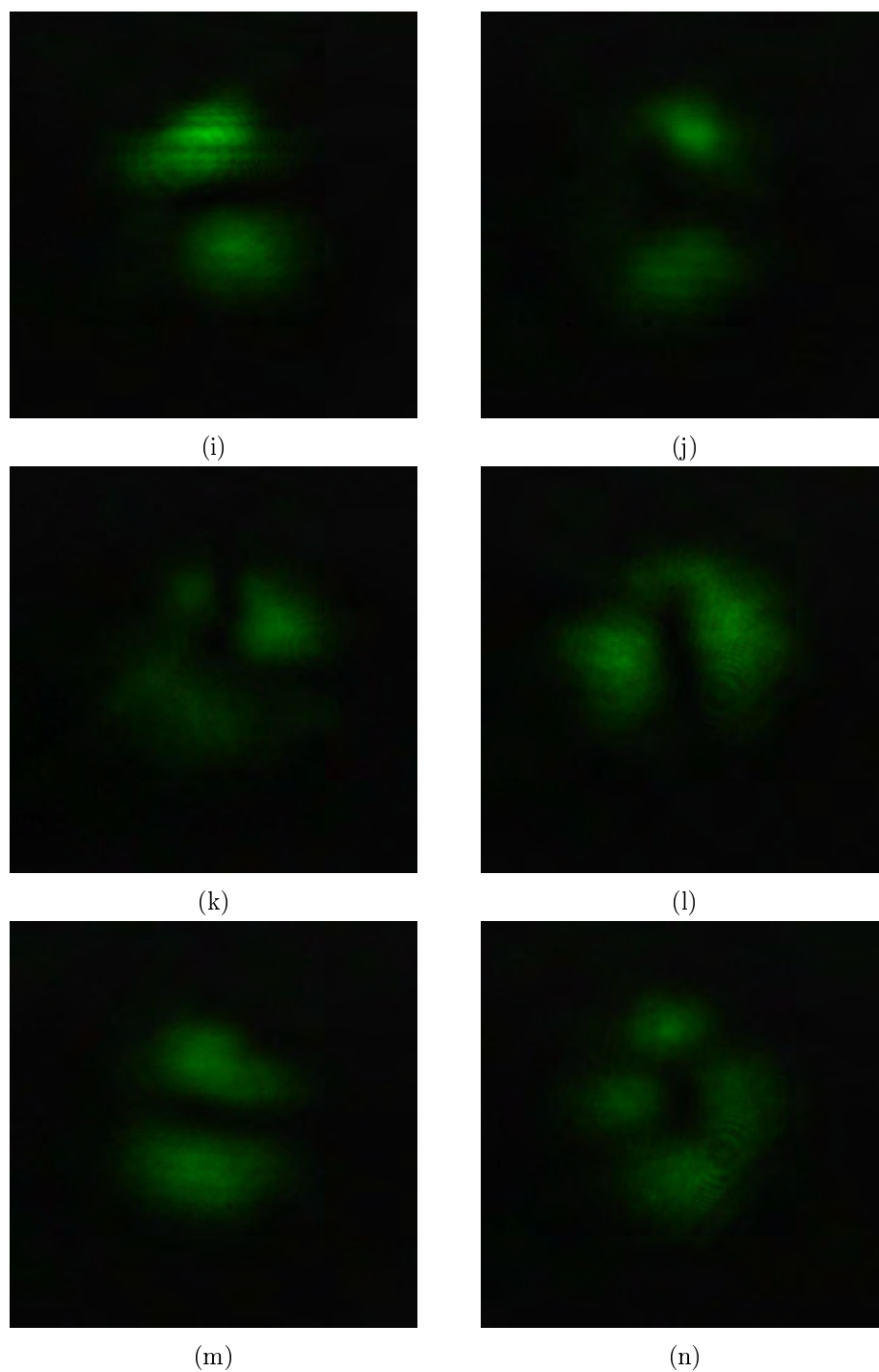
Figure 4.8: Modes obtained at port 1 (1rst column) and port 2 (2nd column) of the MMZI for sample 1 (air). The entrance beam to the interferometer has passed first through the MCA. (a),(b) interferograms at each port without PSA. PSA analyzing horizontal,(c),(d); vertical, (e),(f); +45° (g),(h); −45°, (i),(j); circular right, (k),(l) and circular left (m),(n) polarization states.
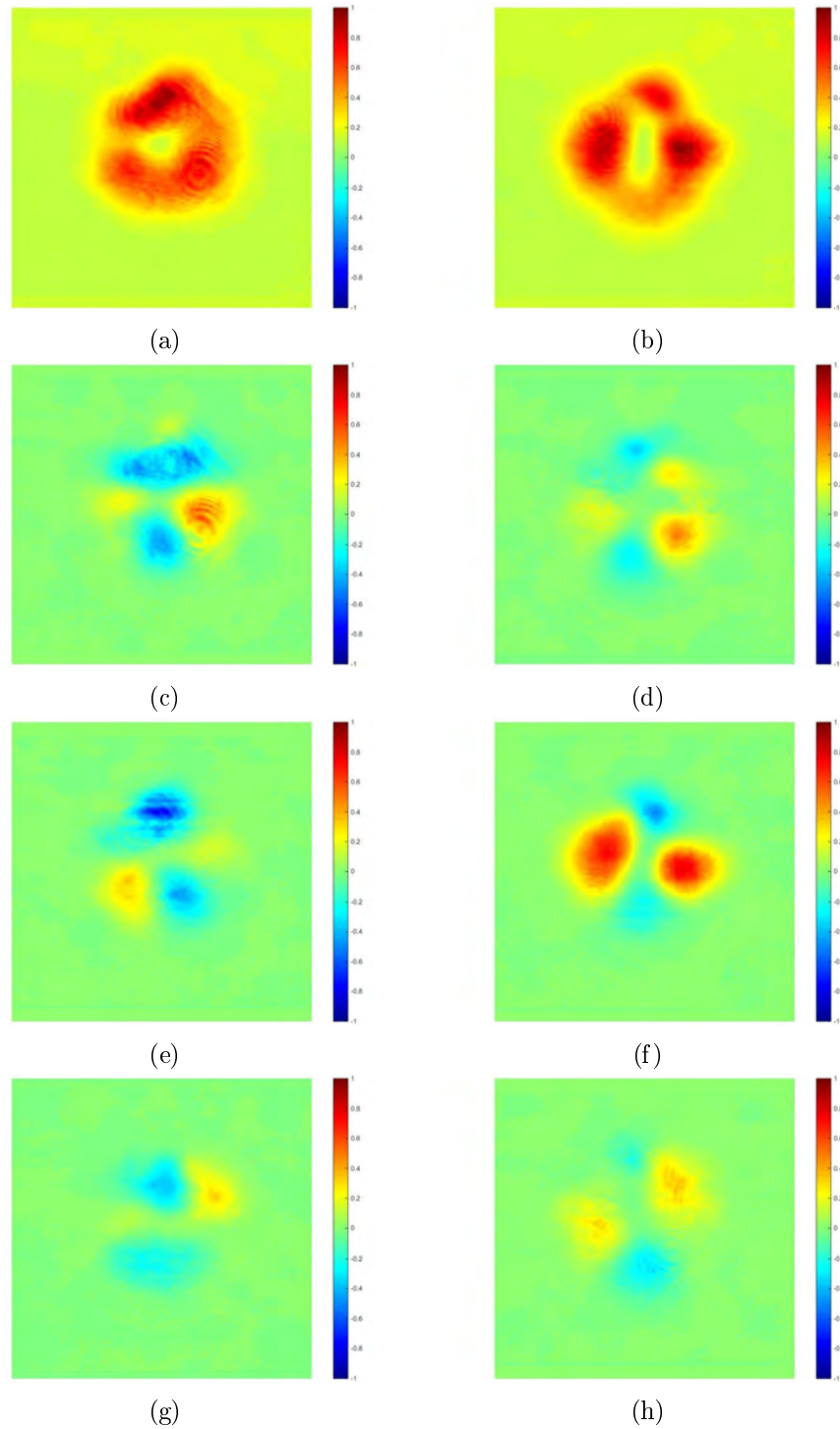
Figure 4.9: Stokes parameters in images and numerical values provided by the SAS code for outputs at port 1 (1rst column) and port 2 (2nd column) of the MMZI for sample 1 (air), MCA. (a),(b) S0. (c),(d) S1. (e),(f) S2. (g),(h) S3. The obtained Stokes vectors are: [1 -0.0581 -0.0746 -0.0642]⊤ for port 1 and [1 0.0011 0.1385 0.0427]⊤ for port 2. Exposure time of t=2ms.

(a)
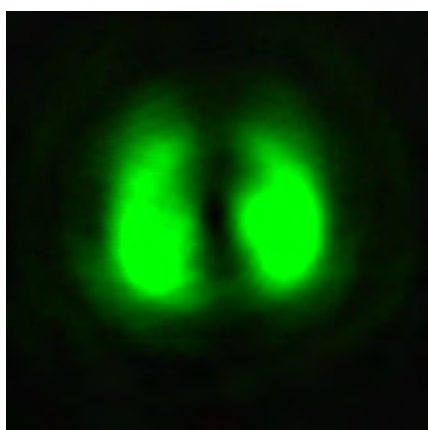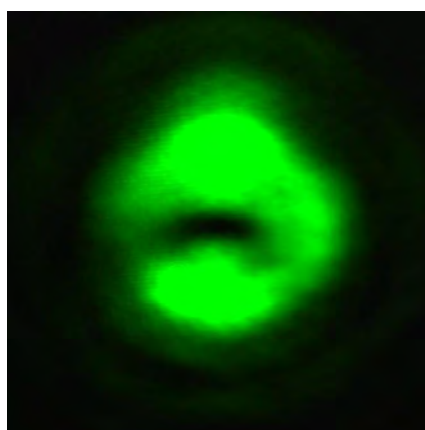
(b)
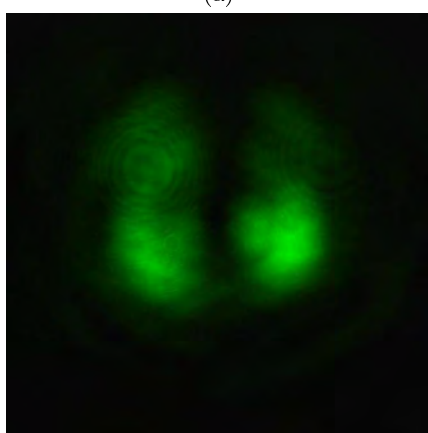
(c)
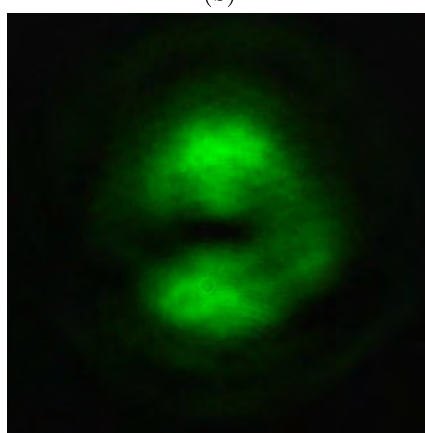
(d)

(e)
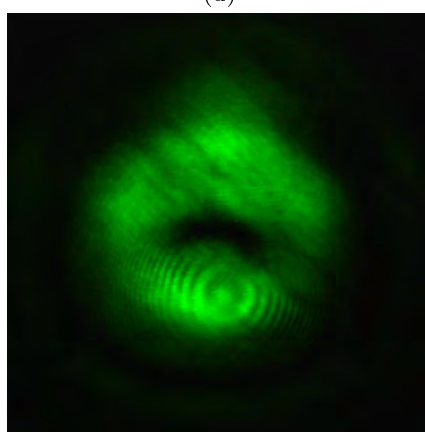
(f)

(g)

(h)

Figure 4.10: Modes obtained at port 1 (1rst column) and port 2 (2nd column) of the MMZI for sample 1 (air). The entrance beam to the interferometer has passed first through the MCB. (a),(b) interferograms at each port without PSA. PSA analyzing horizontal,(c),(d); vertical, (e),(f); +45° (g),(h); −45°, (i),(j); circular right, (k),(l) and circular left (m),(n) polarization states.
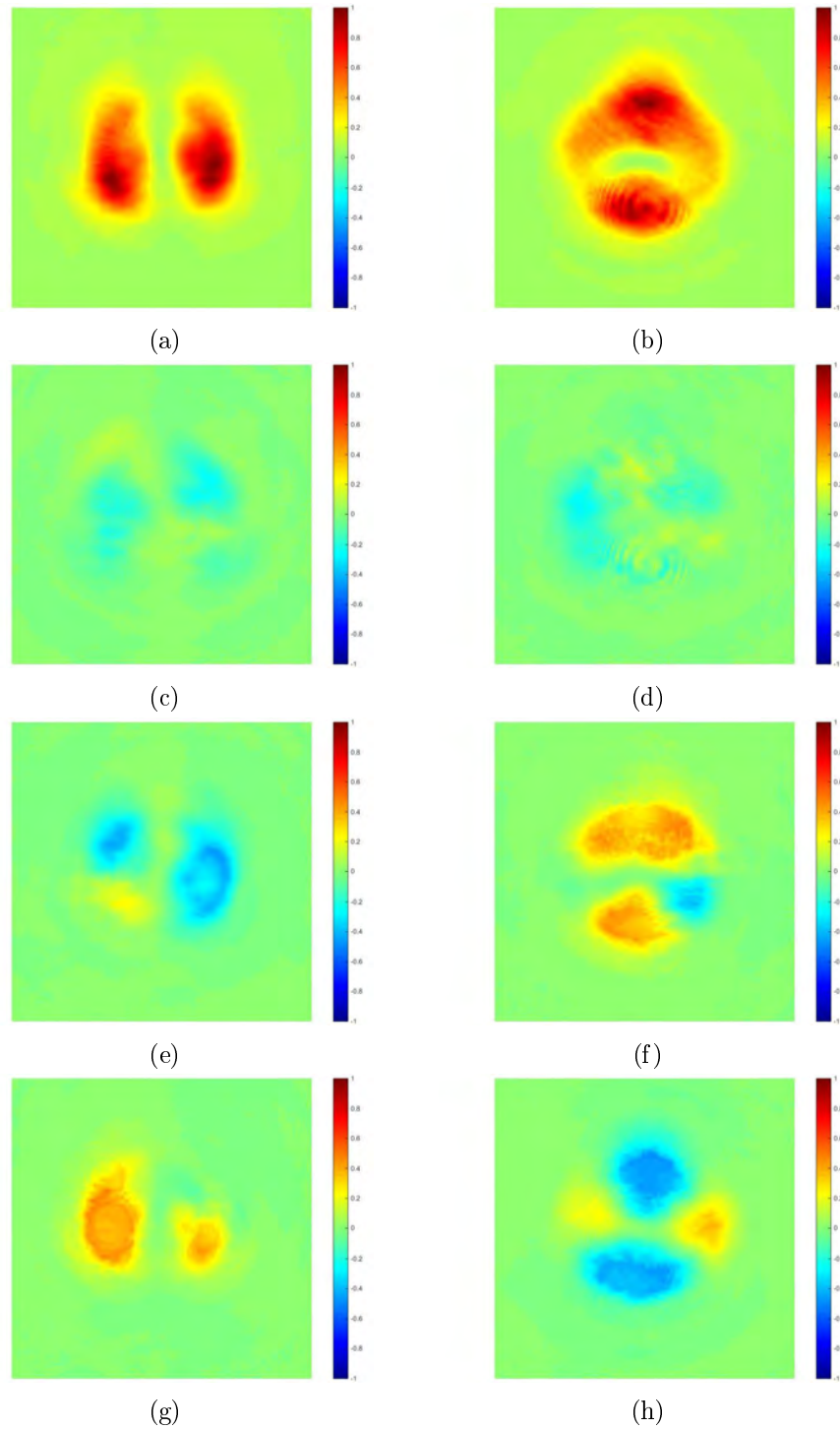
Figure 4.11: Stokes parameters in images and numerical values provided by the SAS code for outputs at port 1 (1rst column) and port 2 (2nd column) of the MMZI for sample 1 (air), MCB. (a),(b) S0. (c),(d) S1. (e),(f) S2. (g),(h) S3. The obtained Stokes vectors are: [1 -0.1009 -0.2316 0.2854]$^\intercal$ for port 1 and [1 -0.0982 0.3036 -0.2053]$^\intercal$ for port 2. Exposure time of t=2ms.

Notice from the description of the Figure 4.11 that, for the interferograms at the output ports of the MMZI, when the beams have passed first through the MCB, the corresponding Stokes vectors have the opposite sign in the S2 parameter, the one that indicates the tendency to $\pm 45°$ polarization and that it is related to the $\Psi_{\pm}$ mode. Due to the polarizing beam splitter behavior of the MMZI and the previous manipulation of the diagonal modes carried out by the MCB, we expect a Ψ_{01} mode with $\hat{\mathbf{e}}_{+}$ polarization and a Ψ_{10} mode with $\hat{\mathbf{e}}_{-}$ polarization at the output ports. From the obtained Stokes vector, we can see a tendency to these polarizations (S2 parameter has a high value) but also we find an important contribution from the S3 parameter, which implies a circular right or left handed tendency for the polarization also. This results in an elliptical right and left handed polarizations for the beams at port 1 and 2, respectively, instead of the searched linear at $\pm 45°$, when the Stokes images are spatially averaged.

On the other hand, the results for MMZI MCC air are the best experimental demonstration of the polarizing beam splitter behavior of the modified Mach-Zehnder interferometer. This fact can be clearly seen from Figure 4.13, where a Ψ_{01} mode with $\hat{\mathbf{e}}_{x}$ polarization and a Ψ_{10} with $\hat{\mathbf{e}}_{y}$ polarization are obtained for ports 1 and 2 respectively. The spatially averaged intensities that the SAS code provide us, also show this tendency to linear horizontal and linear vertical polarizations, respectively. So, through this configuration, we have successfully decomposed the azimuthally polarized beam into its Ψ_{10} and Ψ_{01} mode components, as required by the theoretical proposal (Töppel et al., 2014) in order to obtain the Mueller matrix of the sample (air).
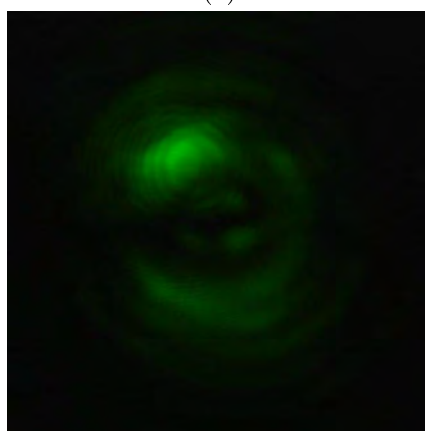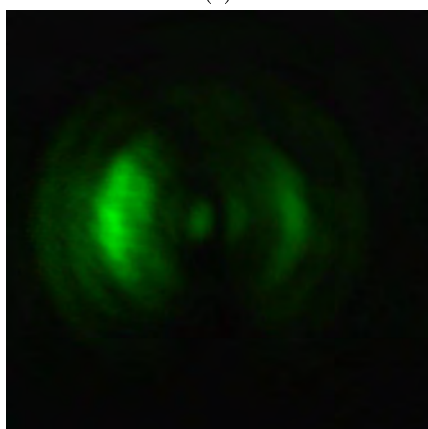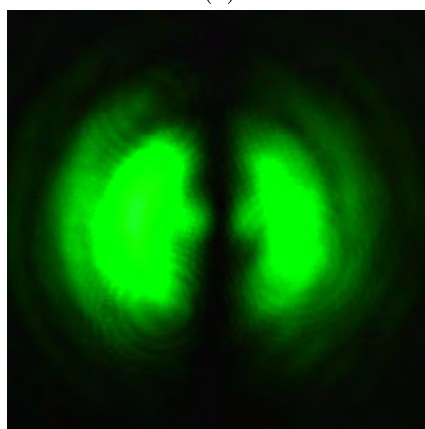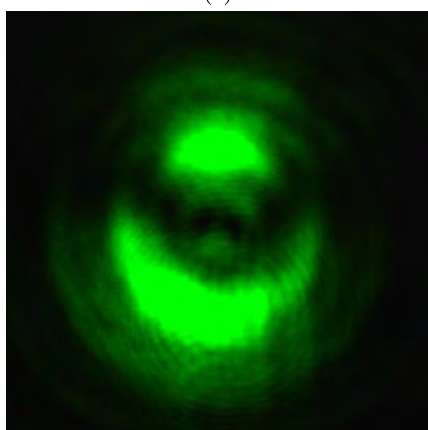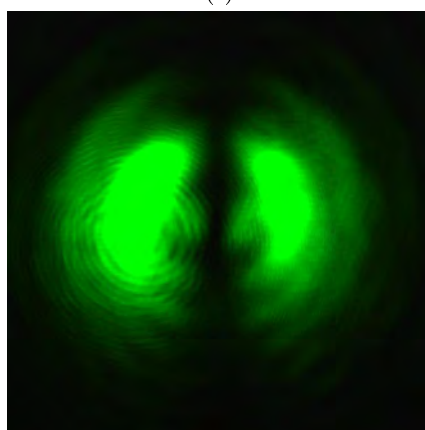
(a)
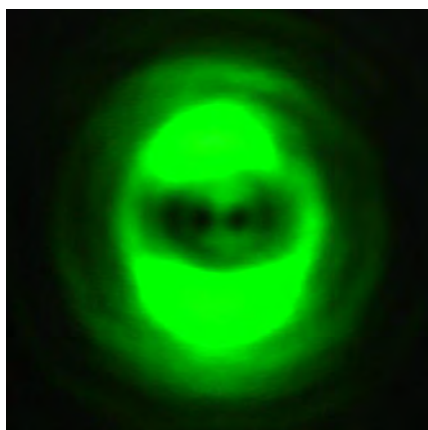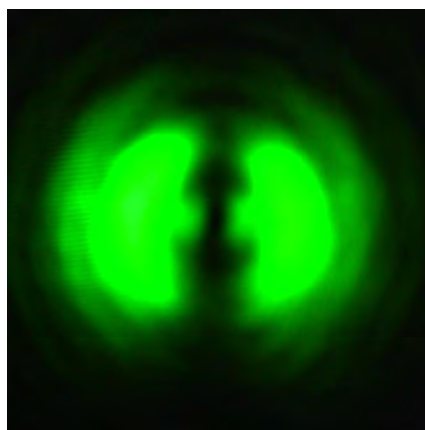
(b)
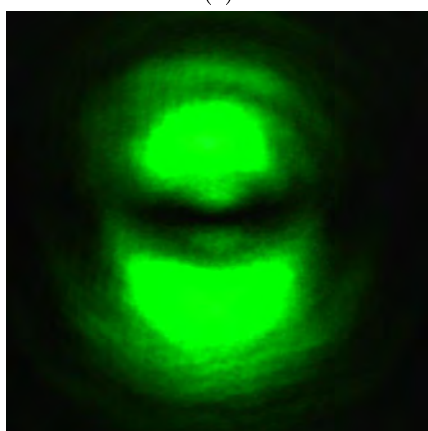
(c)

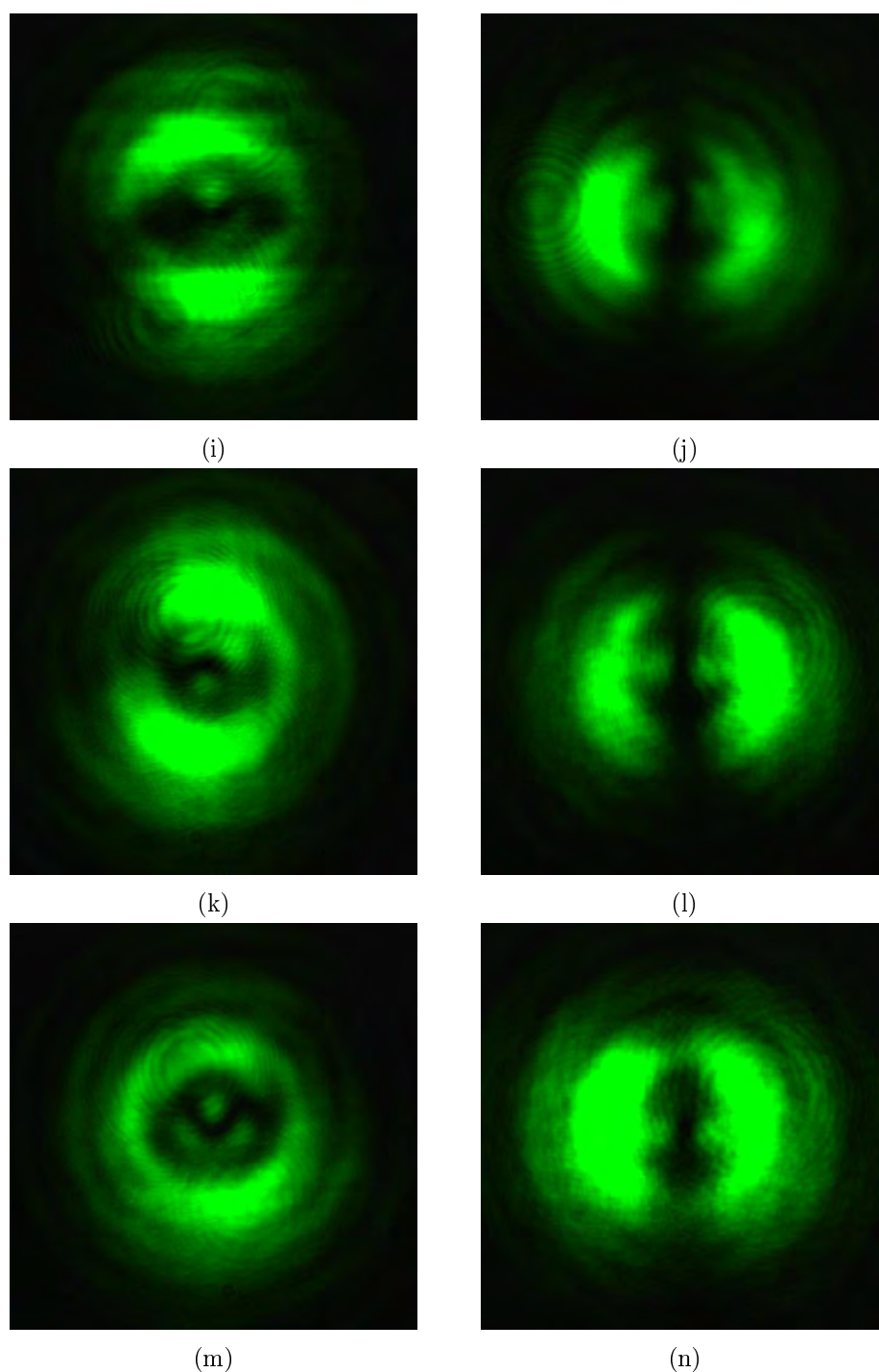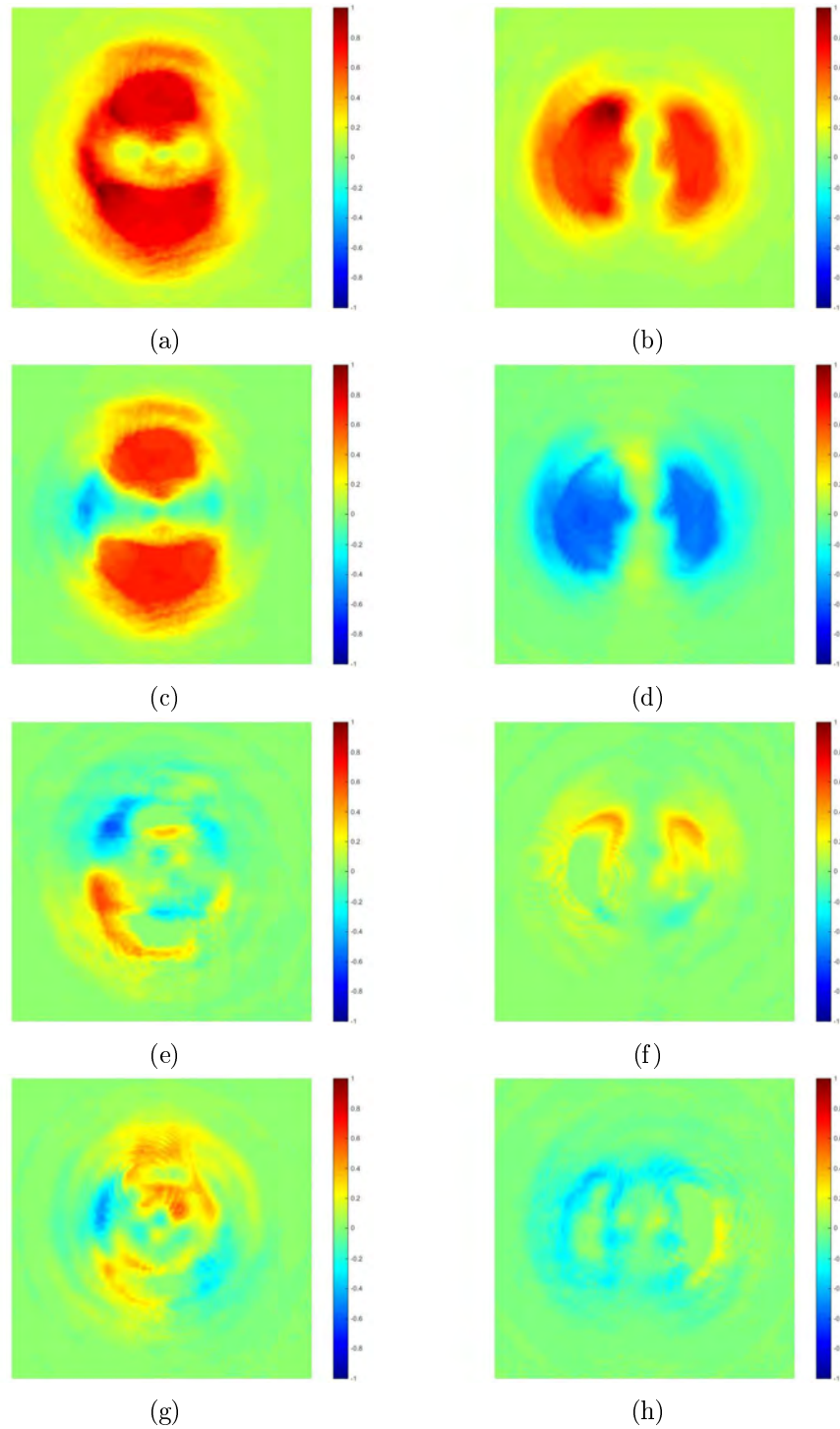(d)

(e)

(f)

(g)

(h)

Figure 4.12: Modes obtained at port 1 (1rst column) and port 2 (2nd column) of the MMZI for sample 1 (air). The entrance beam to the interferometer has passed first through the MCC. (a),(b) interferograms at each port without PSA. PSA analyzing horizontal,(c),(d); vertical, (e),(f); +45° (g),(h); −45°, (i),(j); circular right, (k),(l) and circular left (m),(n) polarization states.

Figure 4.13: Stokes parameters in images and numerical values provided by the SAS code for outputs at port 1 (1rst column) and port 2 (2nd column) of the MMZI for sample 1 (air), MCC. (a),(b) S0. (c),(d) S1. (e),(f) S2. (g),(h) S3. The obtained Stokes vectors are: [1 0.5040 0.0258 0.1310]$^\top$ for port 1 and [1 -0.5483 0.1640 -0.2126]$^\top$ for port 2. Exposure time of t=2ms.

Finally, the Mueller matrix elements for the air were obtained using the expressions in Appendix A and they are shown in Figure 4.14 for images and in Eq. 4.3 for numerical values.

For this case, we have obtained a Mueller matrix that has high values in the diagonal (as expected for the air Mueller matrix) but also has high (and low, which is ok) values outside of it when we would expect low values only. The most extreme case occurs for the M03 element, which has a value of -0.6019 when a close to 0 value was expected. If we track the images used to obtain this value along the complete process (including the use of the transformation matrix, equation 2.51), we will find that this element is obtained through the expression:

$$S_{02} = -I_{00} - I_{01} + 2I_{03} - I_{10} - I_{11} + 2I_{13} \qquad (4.2)$$

I_{00} and I_{10} values are obtained from the MCC MMZI port 2 (the one that shows a HG_{10} mode) when the x and y polarizations are analyzed, respectively. The I_{01} and I_{11} values are obtained from the MCC MMZI port 1 (the port that shows a HG_{01} mode) when the x and y polarizations are analyzed, respectively. The I_{03} and I_{13} values are obtained from the MCA MMZI port 2 (the port that shows a HG_{10} mode) when the x and y polarizations are analyzed, respectively. Now, notice the signs in the expression 4.2, in order to have a close to 0 value, the magnitude of all the MCC obtained intensity values has to be compensated with the ones obtained from the MCA images, which experimentally does not happen because of the important lost of intensity that occurs in MCA (remember that this mode converter is the one that needs more optical components for its implementation). Following this analysis, we find that the best-behaved elements are the ones whose intensities are comparable enough to be added or substracted, and the worst are for the case when a huge difference in intensity is presented externally to the MMZI operation.

This analysis applies also to the obtained images for the rest of our samples.

$$\mathbf{M_{Unc}^{Air}} = \begin{bmatrix} 1,0000 & 0,0406 & 0,2906 & -0,6019 \\ -0,0008 & 0,5261 & 0,0709 & -0,0224 \\ 0,2457 & -0,1018 & 0,4227 & -0,2914 \\ -0,2371 & -0,0654 & -0,0735 & 0,3049 \end{bmatrix} \qquad (4.3)$$
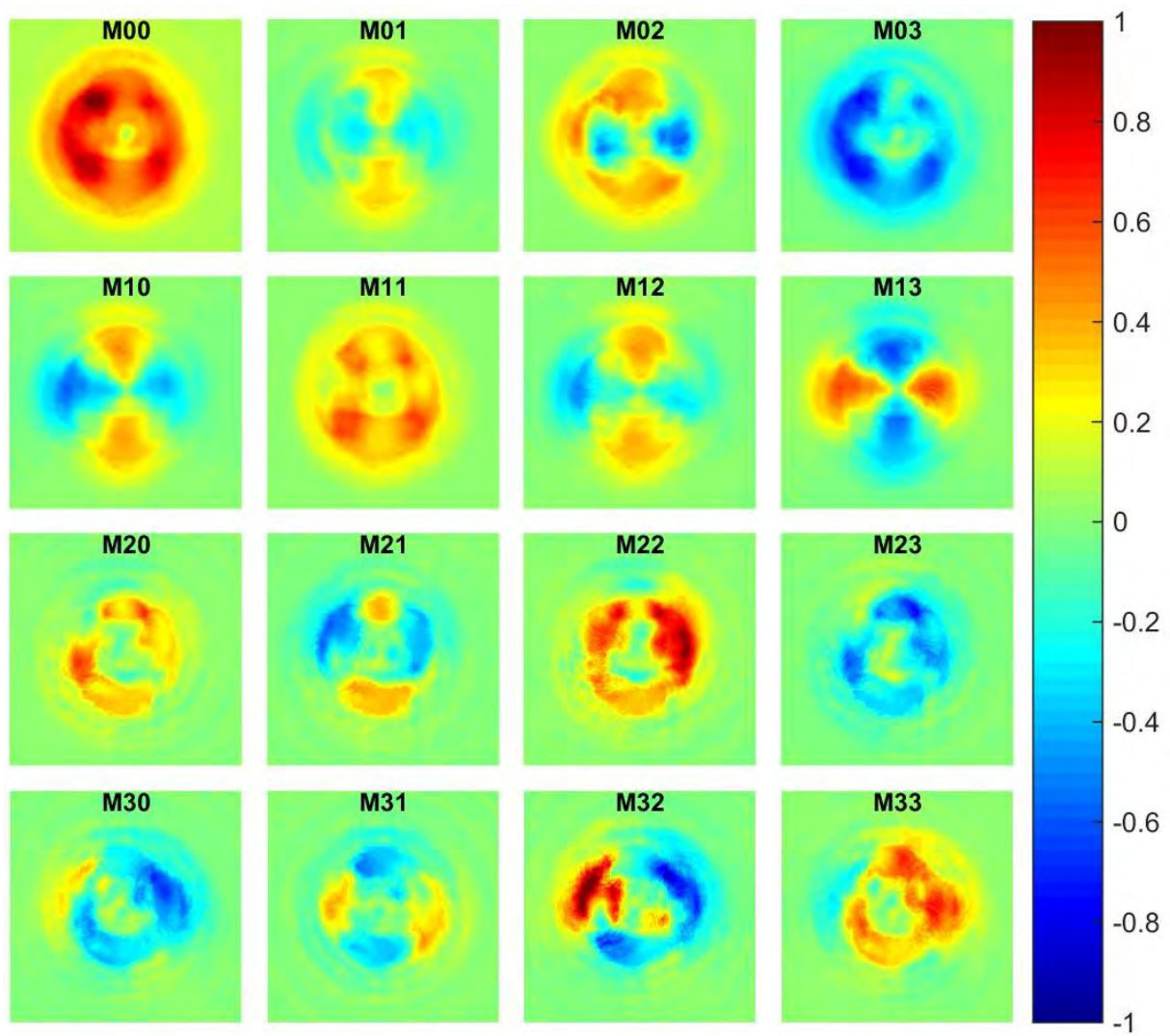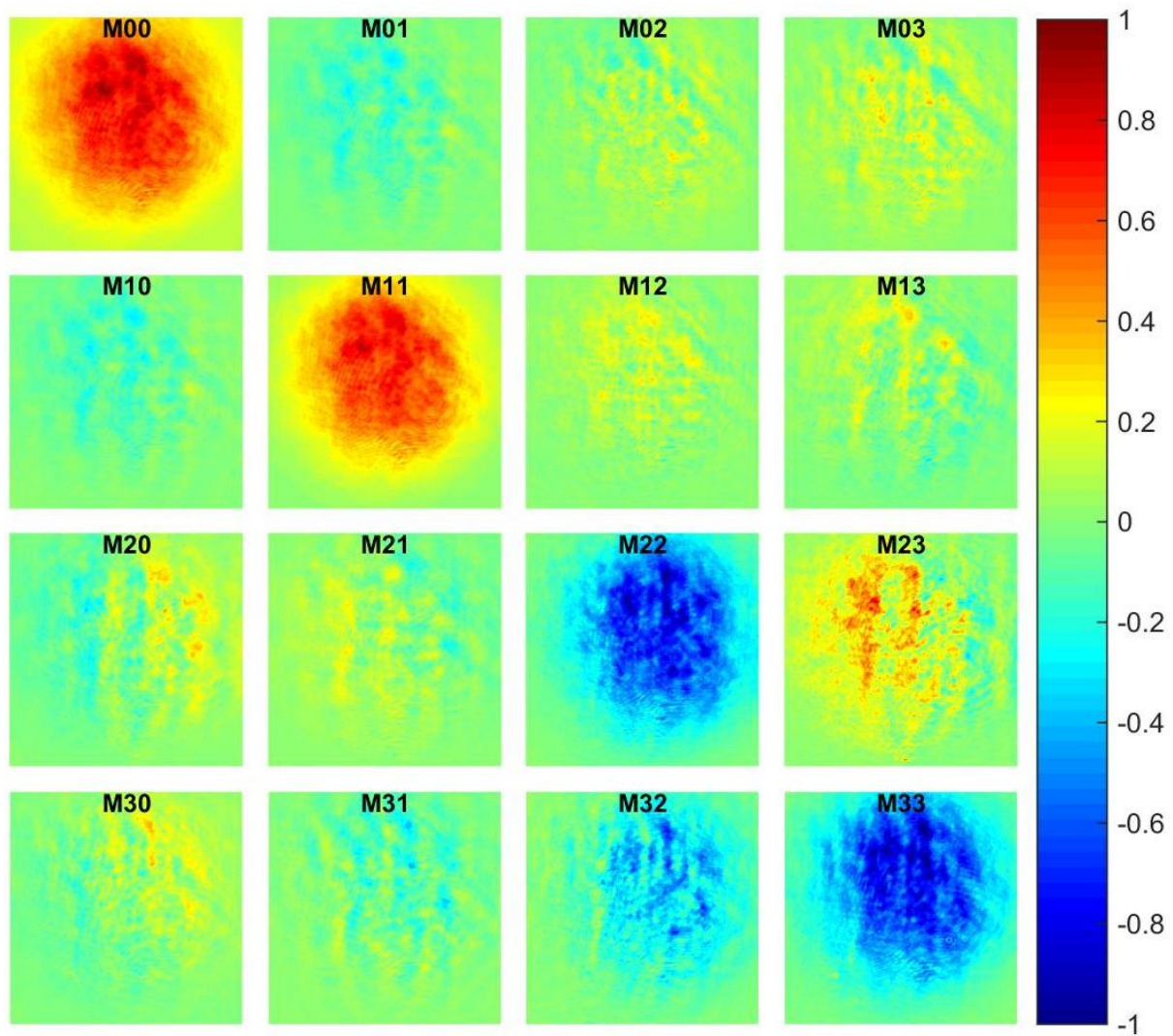
Figure 4.14: Experimental Mueller matrix for Air

Figure 4.15: Experimental Mueller matrix obtained for $\lambda/2$ WP at $0°$, when using the IPA method.

4.4.2. Results for sample 2: $\lambda/2$ waveplate

For the case of the sample 2, a commercial $\lambda/2$ waveplate with its fast axis at $0°$, the Mueller matrix obtained by the IPA method is shown in Figure 4.15 and equation 4.4.

$$\mathbf{M_{IPA}}^{\lambda/2} = \begin{bmatrix} 1{,}0000 & -0{,}1298 & 0{,}0803 & 0{,}1487 \\ -0{,}1198 & 0{,}7771 & 0{,}1072 & 0{,}0339 \\ 0{,}0238 & 0{,}0615 & -0{,}8281 & 0{,}2799 \\ 0{,}0425 & -0{,}0806 & -0{,}3880 & -0{,}8844 \end{bmatrix} \tag{4.4}$$

Again, notice that the experimental Mueller matrix obtained by the IPA method is very close to the expected one, equation 2.23.

For the case of unconventional polarization, we obtained the theoretical Mueller matrix using Töppel et al. (2014) expressions for our $\lambda/2$ WP with fast axis at $0°$ sample. For this, we constructed a schematic diagram similar to the one presented in Chapter 2, Section 2.4 for analyzing the beam as it passes through the complete system once that it has interacted with the sample. The schematic diagram for this case is shown in Figure 4.16.

Using this scheme and the relations in Appendix A, we found that the Theoretical Mueller matrix for this sample, following the proposal in Töppel et al. (2014) is (after being normalized and transformed through equation 2.51 to our optical convention):

$$\mathbf{M_{Unc,theo}}^{\lambda/2} = \begin{bmatrix} 1 & 0 & 0 & 0 \\ 0 & 1 & 0 & 0 \\ 0 & 0 & -1 & 0 \\ 0 & 0 & 0 & -1 \end{bmatrix} \tag{4.5}$$

Which is the expected Mueller matrix (see equation 2.23). This result is obtained also when doing the analysis using a radially polarized beam.
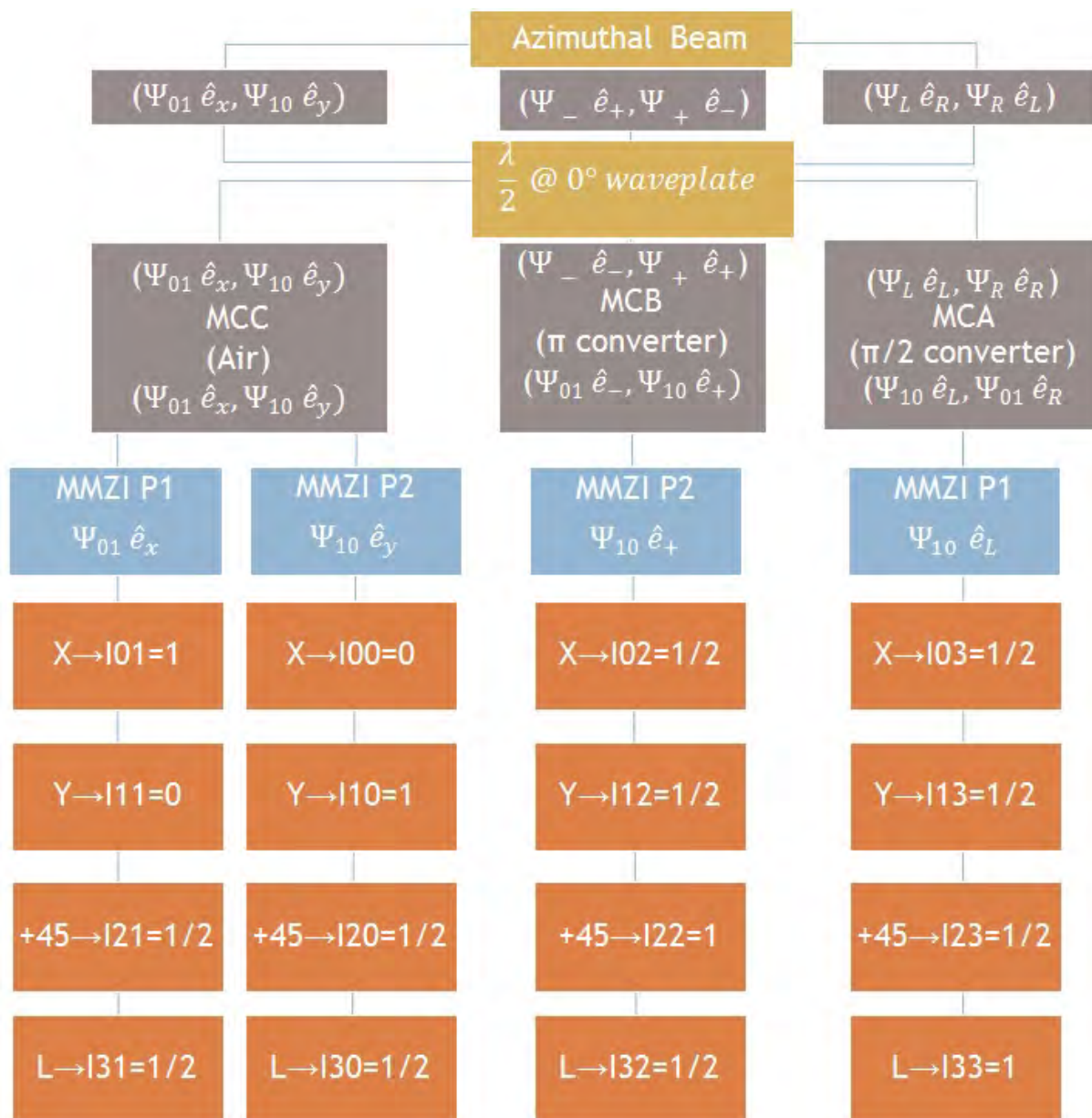
Figure 4.16: Schematic Diagram for the azimuthal beam travelling through the system once it has interacted with the $\lambda/2$ WP sample.

Now, for the experimental results, we present the images obtained from the MMZI, once that the beam has passed through the MCA: Figures 4.17 and 4.18.
The results for the MMZI MCB $\lambda/2$ are shown in Figures 4.19 and 4.20.
The results for the MMZI MCC $\lambda/2$ are shown in Figures 4.21 and 4.22.
Something that can be noticed from the images displayed in Figure 4.17 is that now, the output modes obtained when doing the polarimetric analysis are more deviated from the Ψ_{10} and Ψ_{01} shapes as compared with the ones obtained for MMZI MCA air. This can be related to some imperfection of our sample that causes a small deviation of the beam as it enters to the MCA, this in turn results into a slightly different shape for the transformed mode, which has an impact on the consequent functioning of the interferometer. Aside from this fact, we still can notice a tendency to the Ψ_{10} mode at port 1 and to the Ψ_{01} mode at port 2, which exhibits the mode beam splitter character of the interferometer.
With respect to the polarimetric analysis of the output beams (Figure 4.18), we expected a Ψ_{10} mode with $\hat{\mathbf{e}}_L$ polarization and a Ψ_{01} mode with $\hat{\mathbf{e}}_R$ polarization (see Figure 4.16). The related parameter, S3 image, shows equal contributions for the Ψ_{10} and Ψ_{01} modes, which causes this parameter to be spatially averaged almost to 0 for both output beams. In order to have a tendency for circular polarization, it would be necessary to have a strongest contribution of the Ψ_{10} mode with a low contribution of the Ψ_{01} mode in the S3 parameter of the Stokes vector of one of the beams, and the opposite condition at the other, and also, to have equal contributions of the corresponding modes at the S1 and S2 parameters in order that they spatially average to 0.
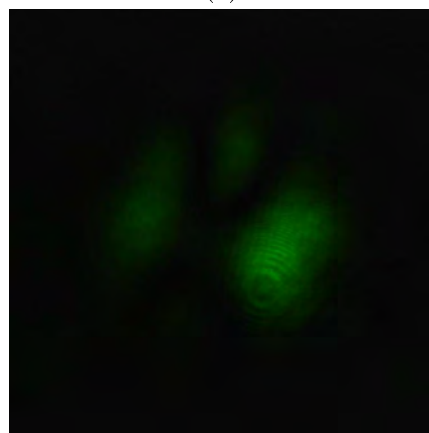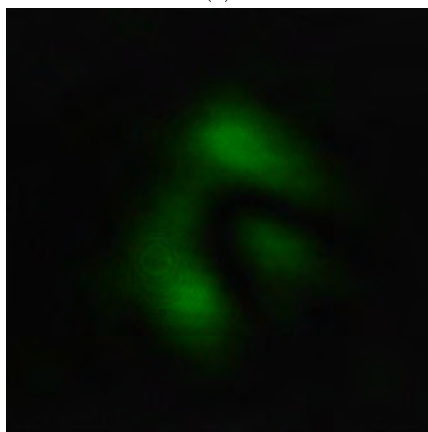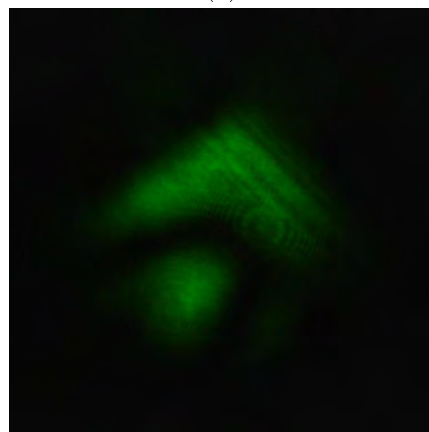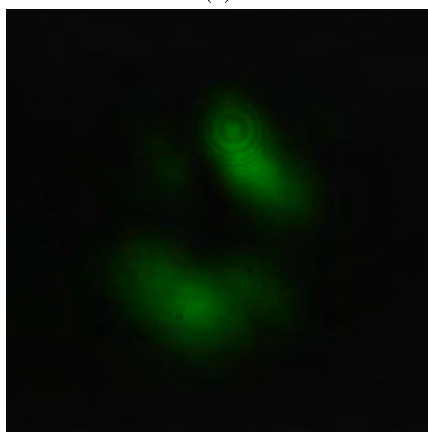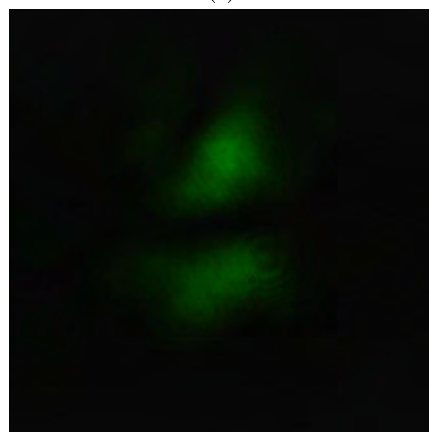
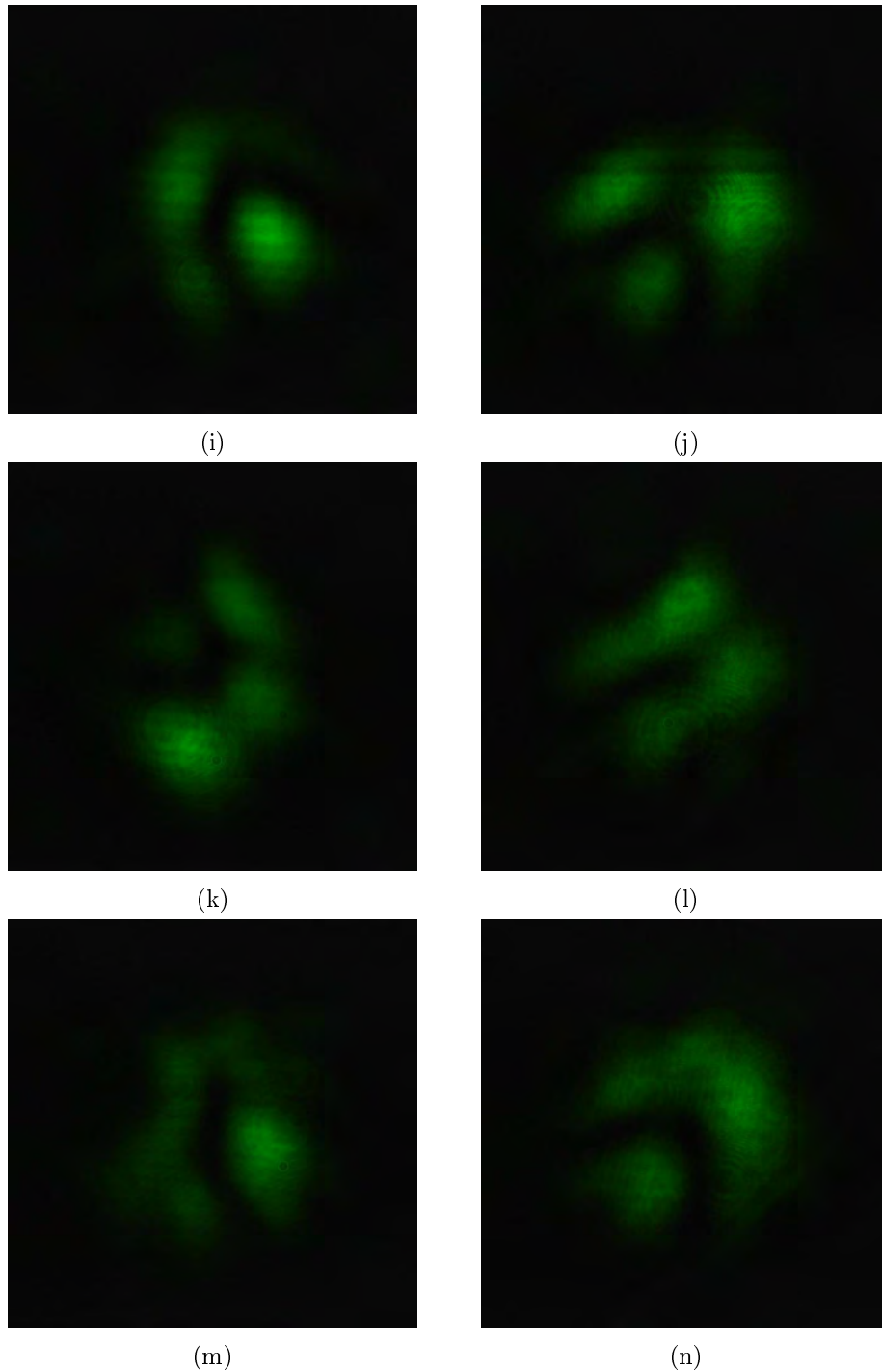(a)
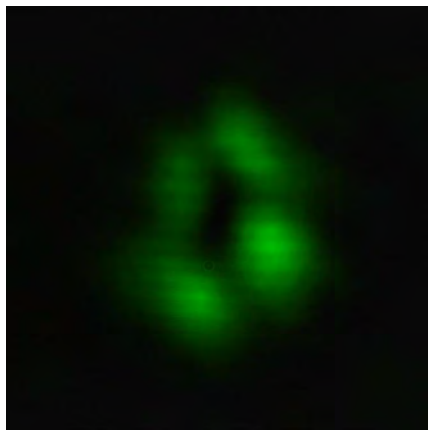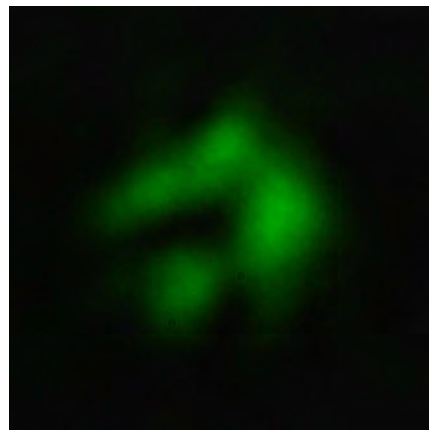
(b)
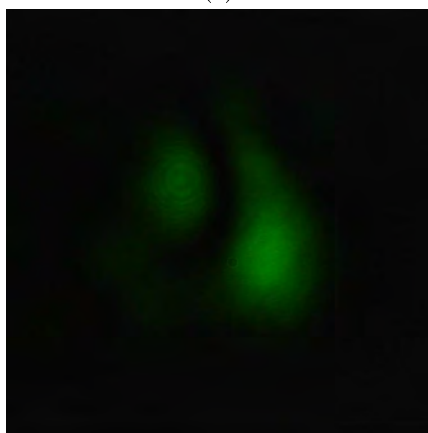
(c)

(d)

(e)

(f)

(g)

(h)

Figure 4.17: Modes obtained at port 1 (1rst column) and port 2 (2nd column) of the MMZI for sample 2 ($\lambda/2$ WP). The entrance beam to the interferometer has passed first through the MCA. (a),(b) interferograms at each port without PSA. PSA analyzing horizontal,(c),(d); vertical, (e),(f); +45° (g),(h); −45°, (i),(j); circular right, (k),(l) and circular left (m),(n) polarization states.
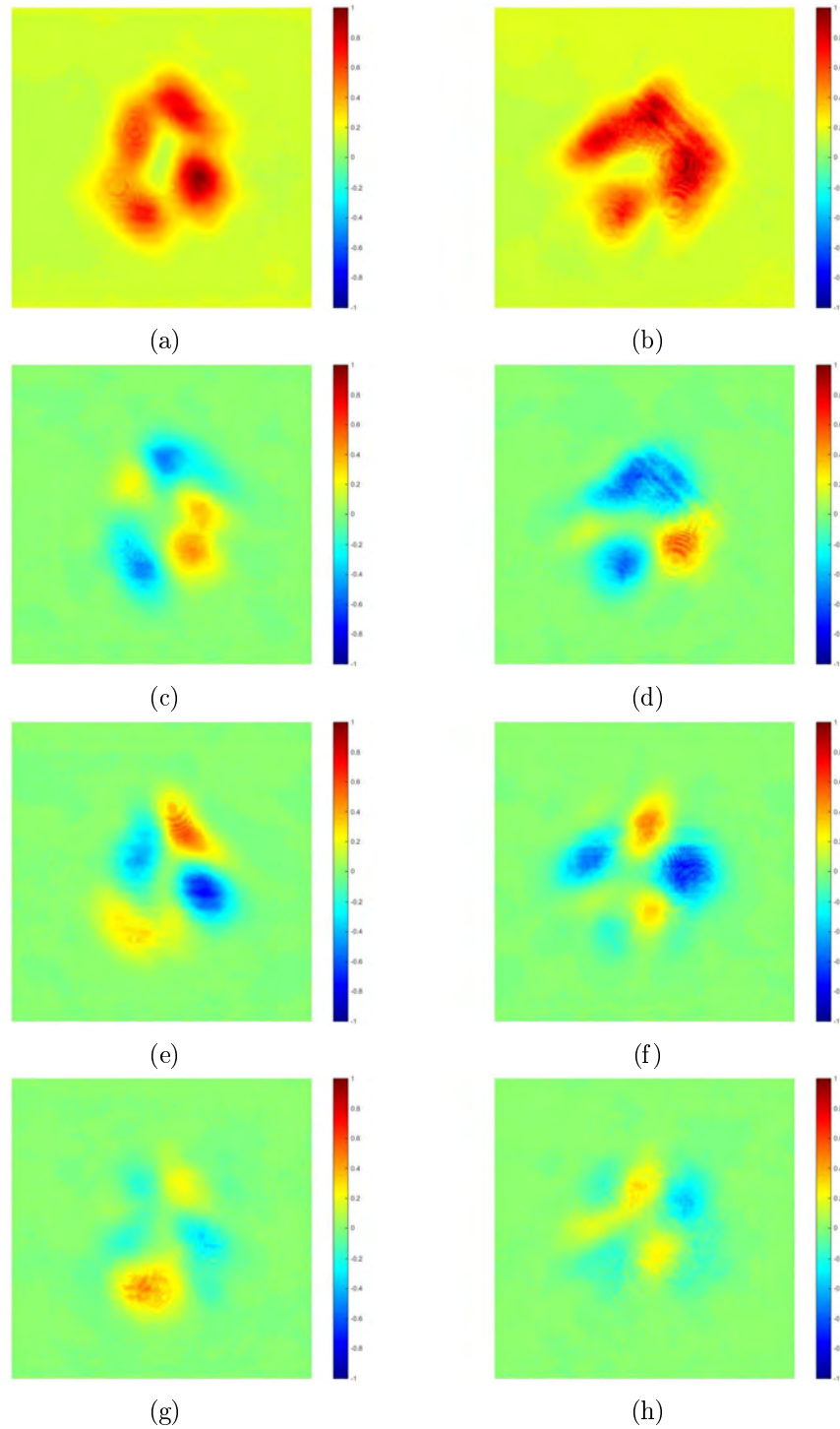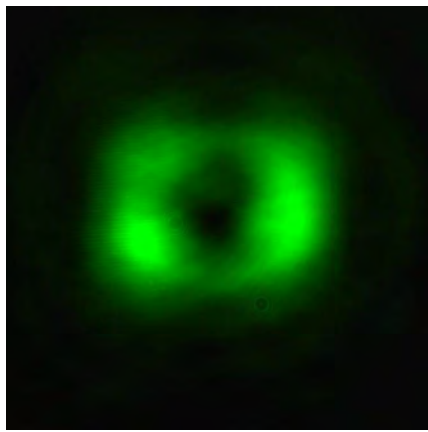
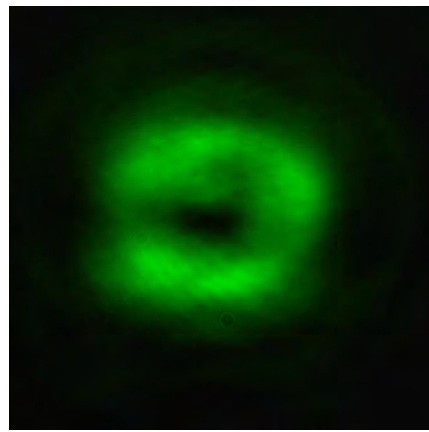Figure 4.18: Stokes parameters in images and numerical values provided by the SAS code for outputs at port 1 (1rst column) and port 2 (2nd column) of the MMZI for sample 2 ($\lambda/2$ WP), MCA. (a),(b) S0. (c),(d) S1. (e),(f) S2. (g),(h) S3. The obtained Stokes vectors are: [1 -0.0398 -0.0122 0.0060]$^{\mathsf{T}}$ for port 1 and [1 -0.1088 -0.1027 -0.0203]$^{\mathsf{T}}$ for port 2. Exposure time of t=2ms.

For the MMZI MCB $\lambda/2$ WP, we expect a Ψ_{10} mode with $\hat{\mathbf{e}}_+$ polarization and a Ψ_{01} mode with $\hat{\mathbf{e}}_-$ polarization. The polarimetric analysis shown in Figure 4.20 indicate us that the corresponding S2 parameter has a positive sign for the beam at port 1 and a negative one for the beam at port 2, which indicates a tendency to 45° and $-45°$ polarization, respectively. The clearest tendency for the diagonal polarization occurs for the beam at port 2, for which the remaining S1 and S3 parameters are almost 0. This is not the case for the Stokes vector for the beam at port 1, that besides that has a non negligible contribution of the orthogonal mode in the S2 parameter, which causes the parameter to be spatially averaged to a low value. Aside from this fact, we still can see a tendency to the horizontal and vertical HG modes at each output port of the interferometer (Figure 4.19).

For the MMZI MCC $\lambda/2$ WP configuration, we can see from Figure 4.22 that we still have a clear demonstration of the polarizing beam splitter behavior of the interferometer, since we have a vertically polarized Ψ_{10} mode at one output (port 1) and a horizontally polarized Ψ_{01} mode at the other (port 2). The mode beam splitter behavior of the interferometer can be seen directly from the images in Figure 4.21.

(a)

(b)
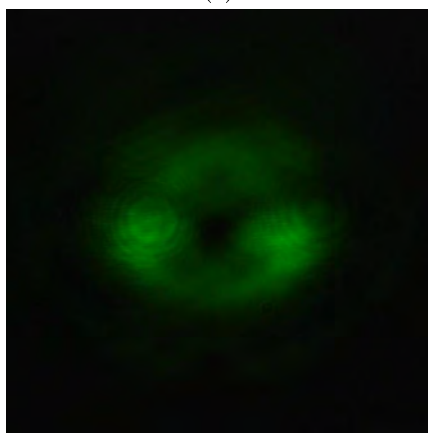
(c)

(d)

(e)

(f)

(g)

(h)

Figure 4.19: Modes obtained at port 1 (1rst column) and port 2 (2nd column) of the MMZI for sample 2 ($\lambda/2$ WP). The entrance beam to the interferometer has passed first through the MCB. (a),(b) interferograms at each port without PSA. PSA analyzing horizontal,(c),(d); vertical, (e),(f); +45° (g),(h); −45°, (i),(j); circular right, (k),(l) and circular left (m),(n) polarization states.

Figure 4.20: Stokes parameters in images and numerical values provided by the SAS code for outputs at port 1 (1rst column) and port 2 (2nd column) of the MMZI for sample 2 ($\lambda/2$ WP), MCB. (a),(b) S0. (c),(d) S1. (e),(f) S2. (g),(h) S3. The obtained Stokes vectors are: [1 -0.1514 0.0745 -0.0802]$^\intercal$ for port 1 and [1 -0.0253 -0.2817 0.0193]$^\intercal$ for port 2. Exposure time of t=2ms.
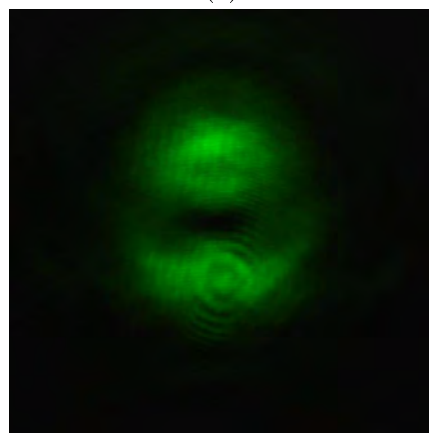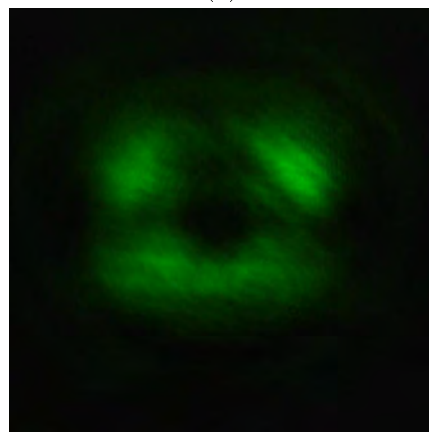
(a)

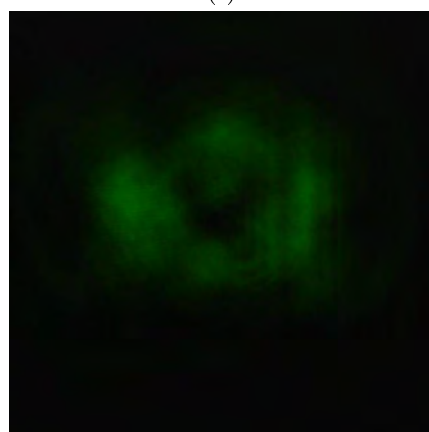

(b)

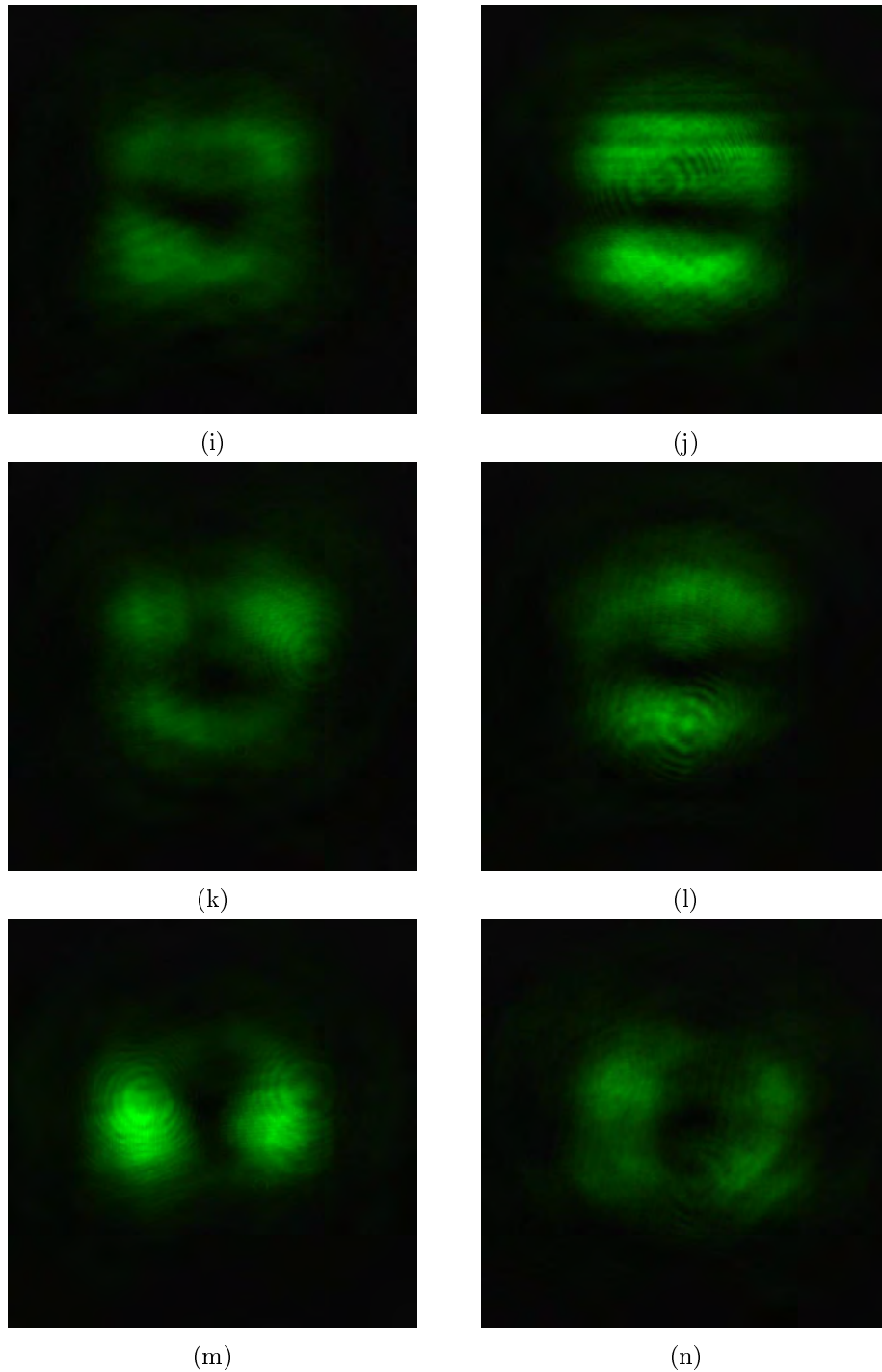(c)
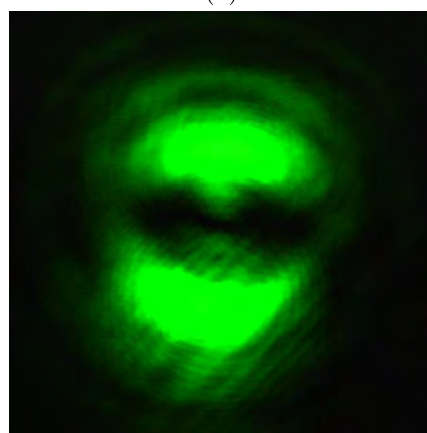
(d)
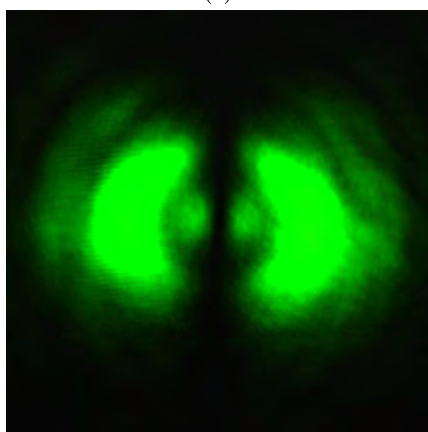
(e)
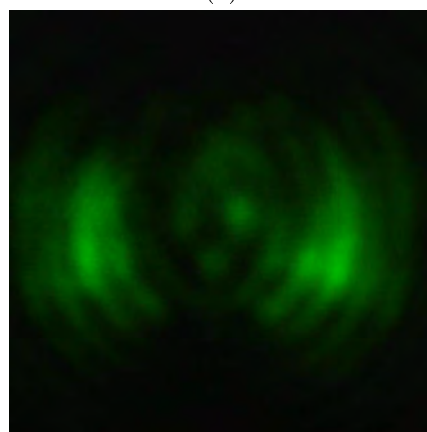
(f)
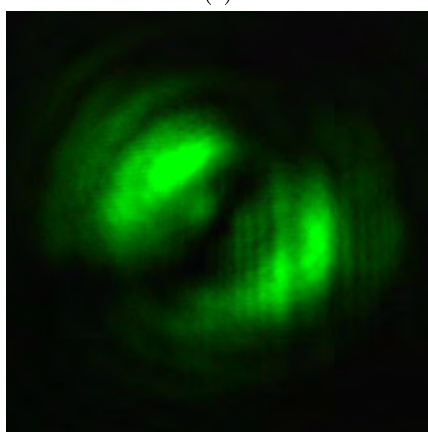
(g)
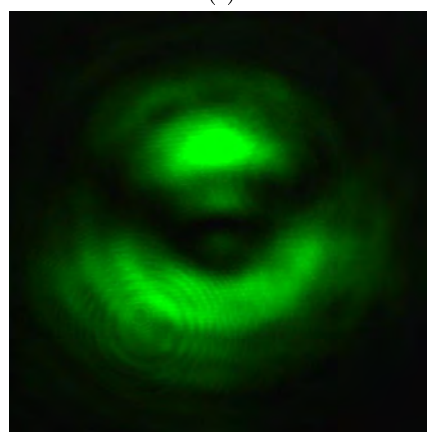
(h)
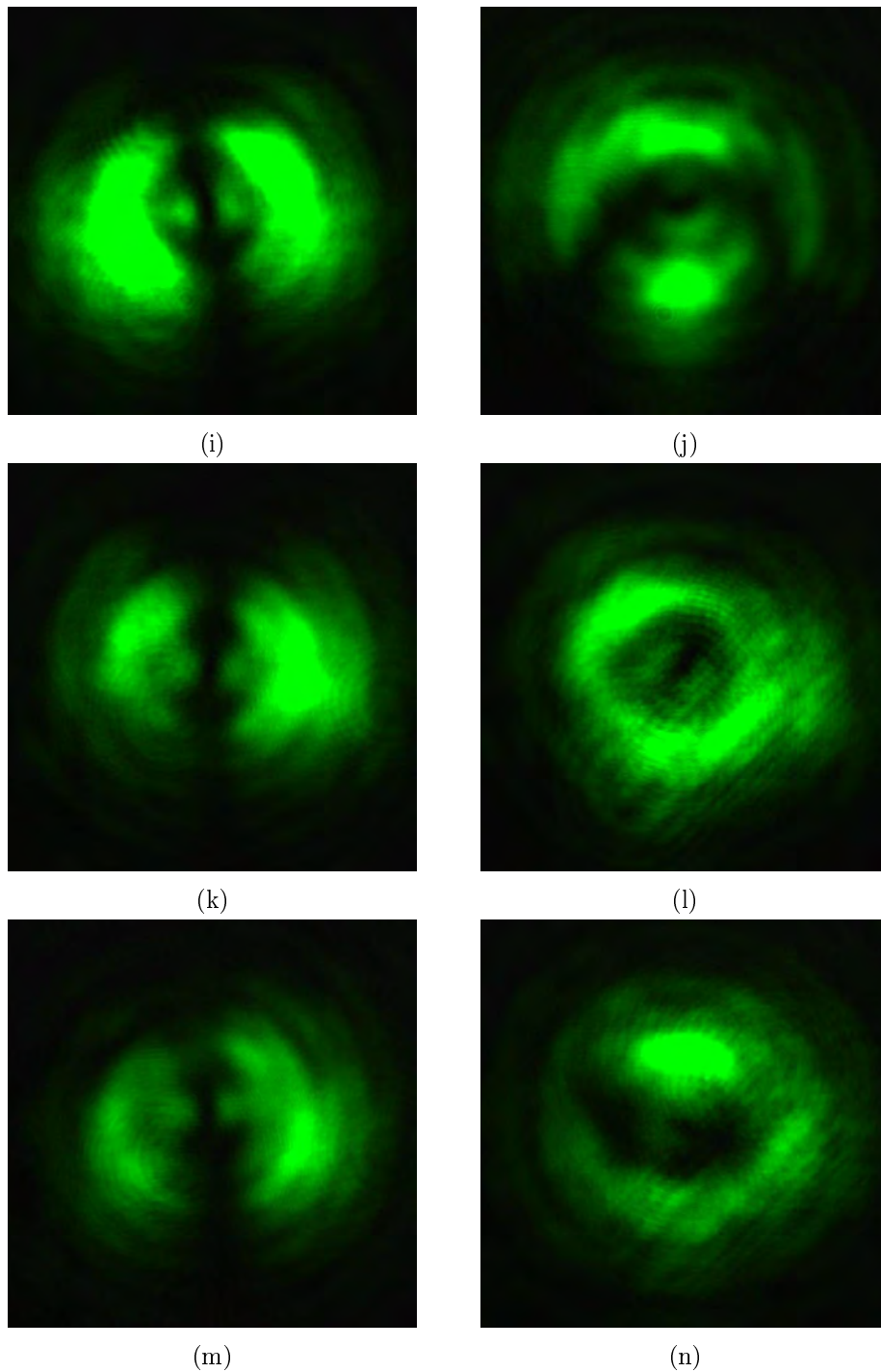
Figure 4.21: Modes obtained at port 1 (1rst column) and port 2 (2nd column) of the MMZI for sample 2 ($\lambda/2$ WP). The entrance beam to the interferometer has passed first through the MCC. (a),(b) interferograms at each port without PSA. PSA analyzing horizontal,(c),(d); vertical, (e),(f); $+45°$ (g),(h); $-45°$, (i),(j); circular right, (k),(l) and circular left (m),(n) polarization states.
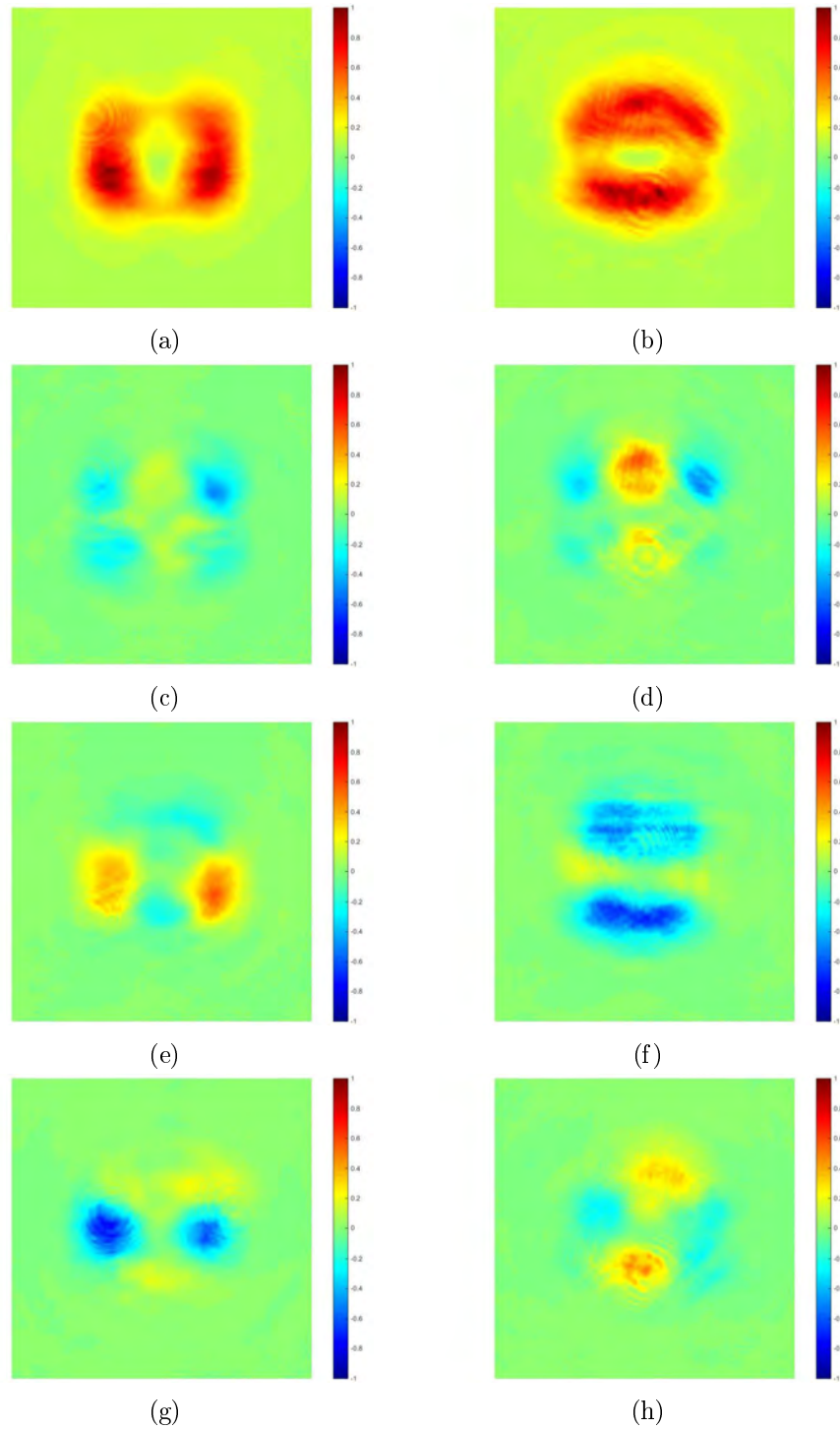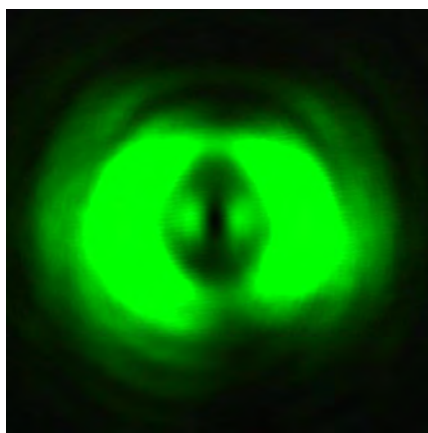
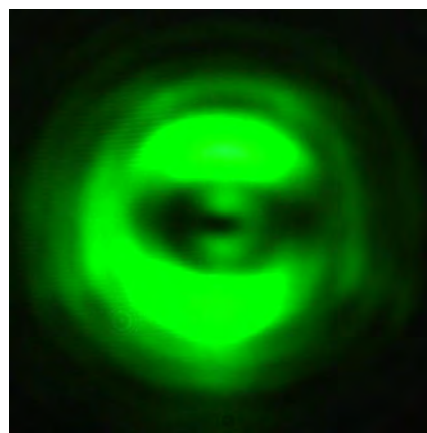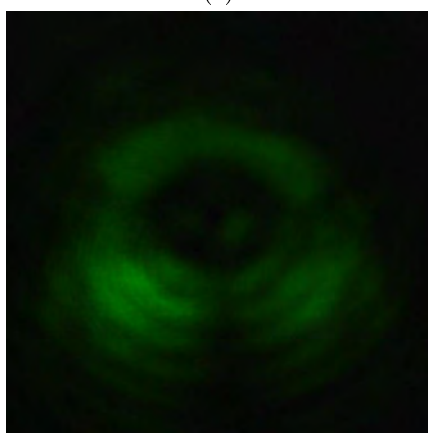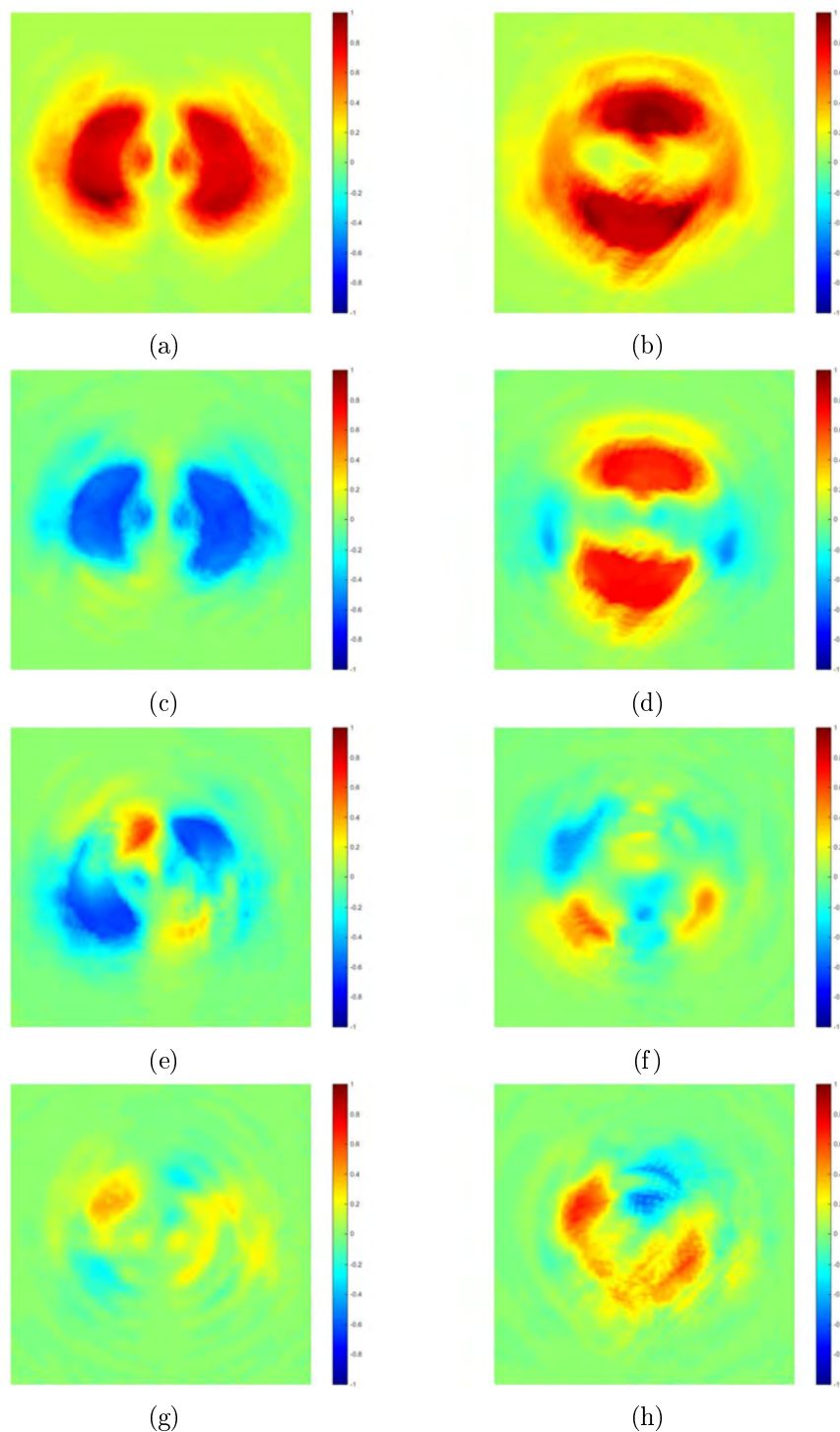Figure 4.22: Stokes parameters in images and numerical values provided by the SAS code for outputs at port 1 (1rst column) and port 2 (2nd column) of the MMZI for sample 2 ($\lambda/2$ WP), MCC. (a),(b) S0. (c),(d) S1. (e),(f) S2. (g),(h) S3. The obtained Stokes vectors are: [1 -0.4494 -0.2644 0.0868]$^\intercal$ for port 1 and [1 0.3153 -0.0151 0.1144]$^\intercal$ for port 2. Exposure time of t=2ms.
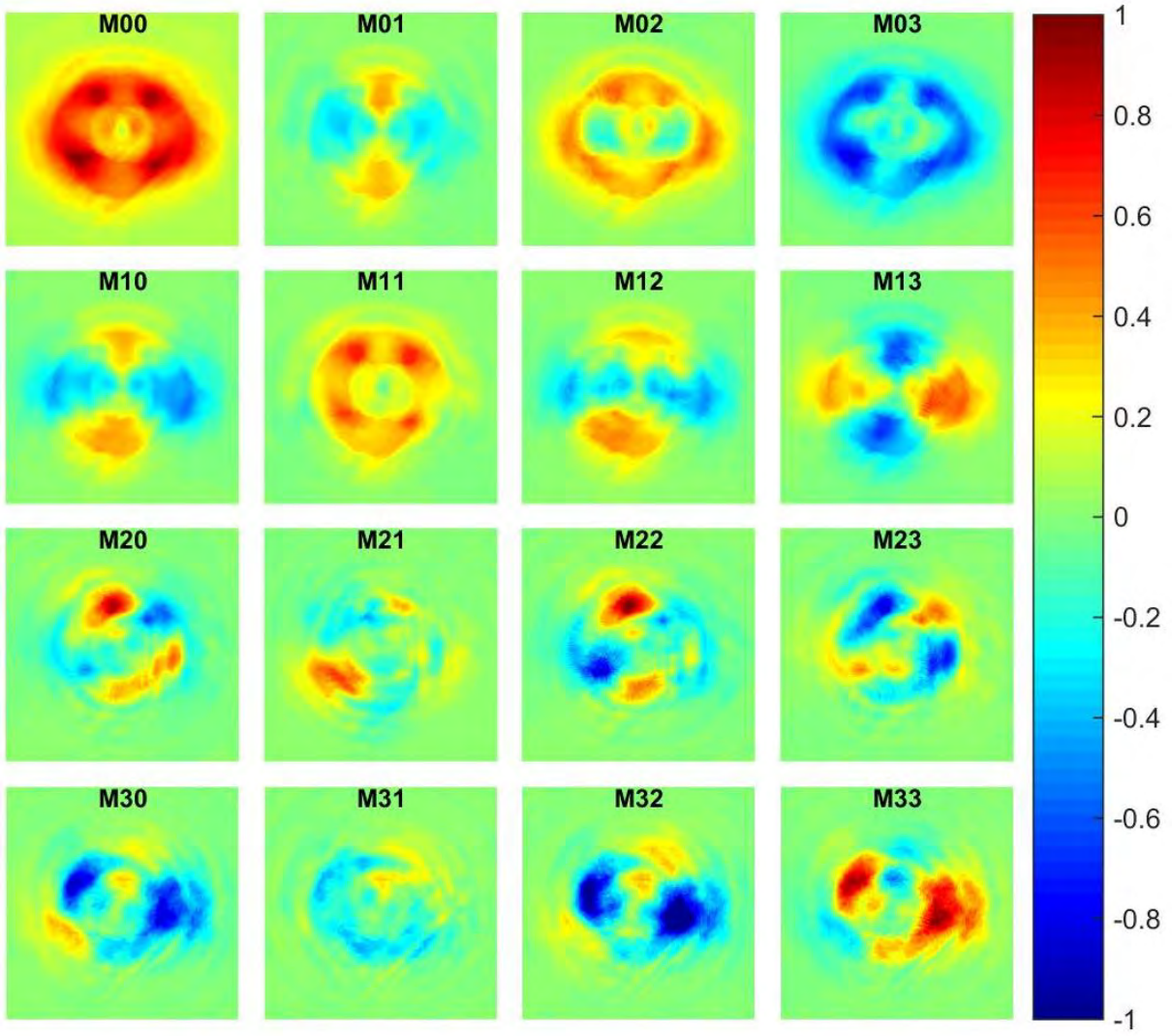
Figure 4.23: Experimental Mueller matrix for $\lambda/2$ WP.

Finally, the Mueller matrix elements for the $\lambda/2$ WP were obtained using the expressions in Appendix A and they are shown in Figure 4.23 for images and in Eq. 4.6 for numerical values.

$$\mathbf{M_{Unc}}^{\lambda/2} = \begin{bmatrix} 1{,}0000 & 0{,}0053 & 0{,}4288 & -0{,}5889 \\ -0{,}0666 & 0{,}3836 & 0{,}0199 & 0{,}0218 \\ -0{,}0153 & 0{,}0523 & -0{,}0628 & -0{,}0455 \\ -0{,}2167 & -0{,}0911 & -0{,}2618 & 0{,}2168 \end{bmatrix} \tag{4.6}$$

Again we see that we obtain high values outside of the diagonal that can be explained by the same reasoning previously exposed for the case of air. However, there is also here a particularly low value in one of the elements of the diagonal, the M22 element, which is almost 0 when we were expecting a -1 value. Tracking the obtention of this element, we see that it is obtained from the expression:

$$- S_{11} = -\{I_{00} + I_{01} - 2I_{02} + I_{10} + I_{11} - 2(I_{12} + I_{20} + I_{21} - 2I_{22})\} \tag{4.7}$$

Where the I_{00}, I_{10} and I_{20} values are obtained from the MCC MMZI Port 1 (Ψ_{10} mode), the I_{01},

I_{11} and I_{21} values are obtained from the MCC MMZI Port 2 (Ψ_{01} mode) and the I_{02}, I_{12} and I_{22} values are obtained from the MCB MMZI Port 1 (Ψ_{10} mode). The theoretical analysis indicates that equation 4.7 will led to a -1 value, however, in order for this to happen experimentally, the intensity values should be almost 1 for I_{01}, I_{10} and I_{22}; almost 0 for I_{00} and I_{11}, and almost 0.5 for I_{02}, I_{12}, I_{20} and I_{21}, which in general holds (from the corresponding Figures we can see that we have high, medium and low values of intensity in these images) except for the case of I_{22} which does not particularly has a high intensity (you can see this by looking the intensity of the image obtained when analysing the corresponding orthogonal polarization, which is almost the same). This deviation from the perfect 1 value led us to have almost equal contributions from the Ψ_{10} and Ψ_{01} modes, which spatially average to almost 0. This is a very illustrative example of the importance of polarizing beam splitter behavior of the interferometer: The I_{22} intensity was supposed to be one because the MMZI was supposed to split the incoming beam into its Ψ_{01} $\hat{\mathbf{e}}_-$ and Ψ_{10} $\hat{\mathbf{e}}_+$ components, but, from Figure 4.20 we see that the polarization of the output beams barely exhibits that tendency, which leads to have important deviations on the expected results.
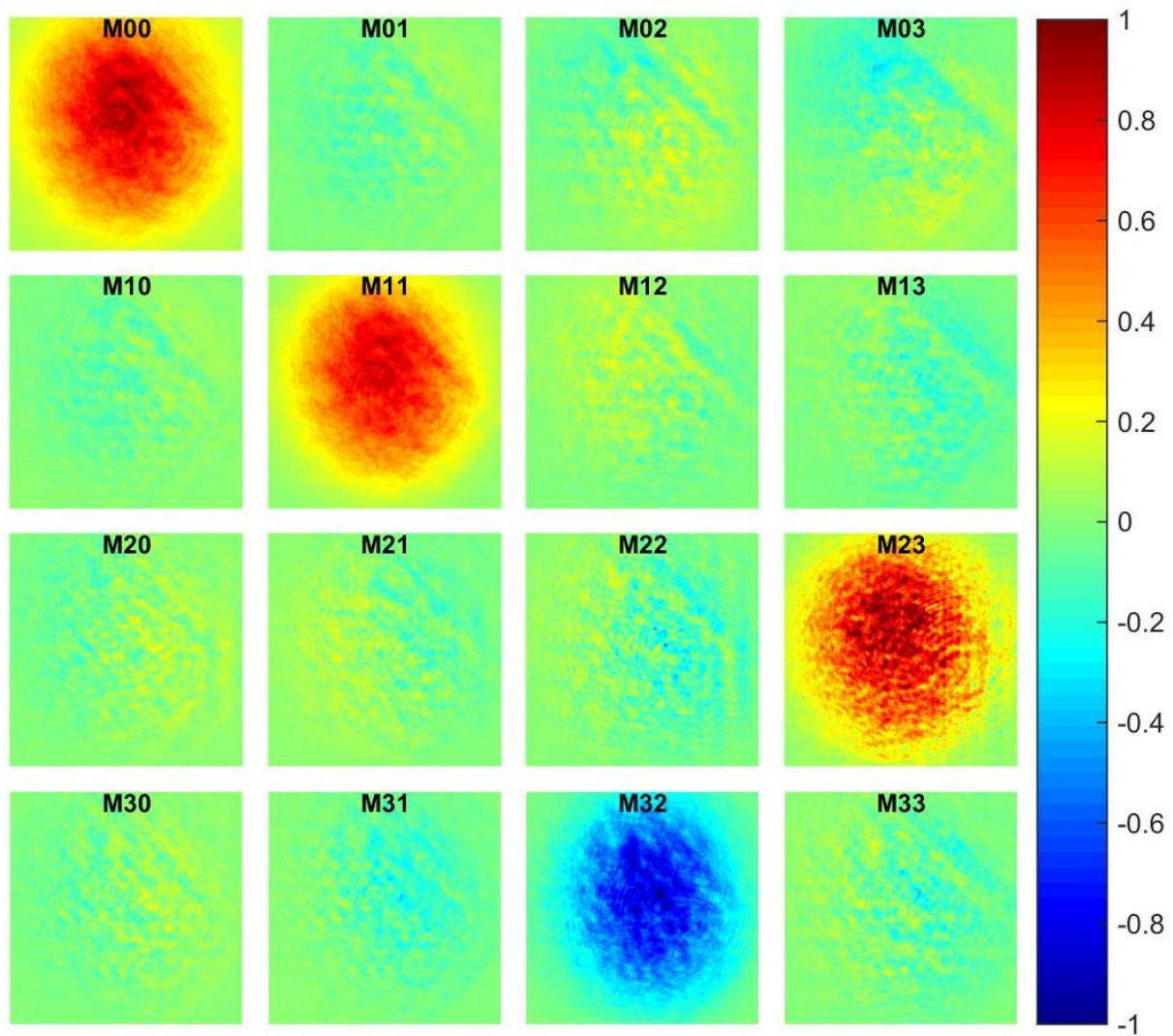
Figure 4.24: Experimental Mueller matrix for $\lambda/4$ WP at 0°, using IPA method

4.4.3.   Results for sample 3: $\lambda/4$ waveplate

We now present the images obtained for the sample 3: a commercial $\lambda/4$ waveplate with its fast axis at 0°, when using the IPA method, Figure 4.24 and equation 4.8.

$$
\mathbf{M_{IPA}}^{\lambda/4} = \begin{bmatrix} 1{,}0000 & -0{,}0477 & 0{,}0268 & -0{,}0538 \\ -0{,}0349 & 0{,}8218 & 0{,}0334 & -0{,}0961 \\ 0{,}0128 & 0{,}0114 & -0{,}0840 & 0{,}9101 \\ -0{,}0061 & 0{,}1317 & -0{,}8264 & -0{,}0777 \end{bmatrix} \tag{4.8}
$$

Comparing equations 4.8 and 2.27, we can see that the experimental results obtained by the IPA method are very close to the expected ones. We also can verify this visually from the image representation of the Mueller matrix in Figure 4.24.

For the case of unconventional polarization, again we construct a schematic diagram similar to the one presented in Chapter 2, Section 2.4 for analyzing the beam as it passes through the complete system once that it has interacted with the sample. The schematic diagram for this case is shown in Figure 4.25. Using this scheme and the relations in Appendix A, we found that the Theoretical Mueller matrix for this sample, following the proposal in Töppel et al. (2014) is (after being normalized and transformed through equation 2.51 to our optical convention):

$$\mathbf{M_{Unc,theo}}^{\lambda/4} = \begin{bmatrix} 1 & 0 & 0 & 0 \\ 0 & 1 & 0 & 0 \\ 0 & 0 & 0 & 1 \\ 0 & 0 & -1 & 0 \end{bmatrix} \tag{4.9}$$

Which corresponds to the expected Mueller matrix for this sample (see equation 2.29). The same result was obtained also when doing the analysis using a radially polarized beam.
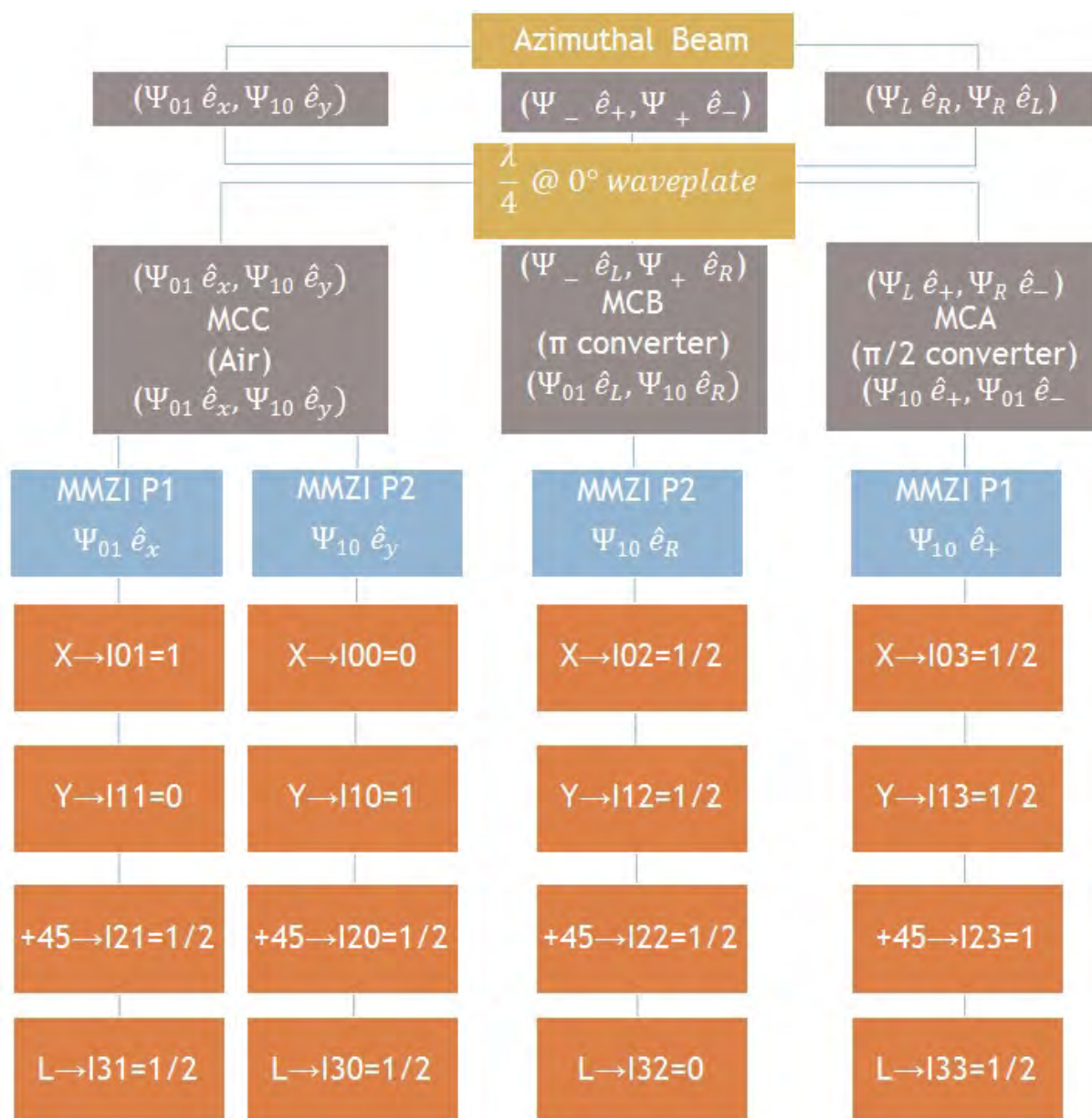
Figure 4.25: Schematic Diagram for the azimuthal beam travelling through the system once it has interacted with the $\lambda/4$ WP sample.

For the experimental results, we present the images obtained from the MMZI, once that the beam has passed through the MCA: Figures 4.26 and 4.27.

The results for MMZI MCB $\lambda/4$ are shown in Figures 4.28 and 4.29.

The results for MMZI MCC $\lambda/4$ are shown in Figures 4.30 and 4.31.

In these figures we can see the same tendency as before: the closest to the expected results are for the MMZI MCC configuration (the beam passes directly to the interferometer) and the worst for the MMZI MCA configuration (which is the most complex module). This show us the importance that has the beam symmetry for the correct functioning of the mode beam splitter (MMZI).

(a)

(b)

(c)

(d)

(e)

(f)

(g)

(h)

<center>(i)</center>

<center>(j)</center>

<center>(k)</center>

<center>(l)</center>

<center>(m)</center>

<center>(n)</center>
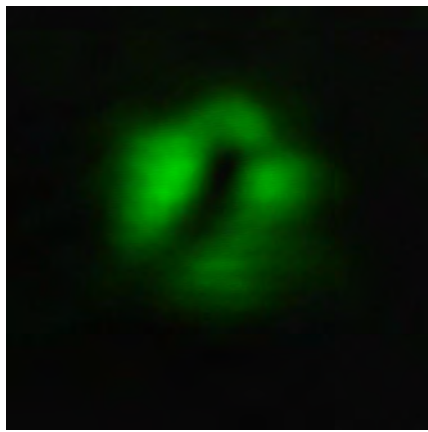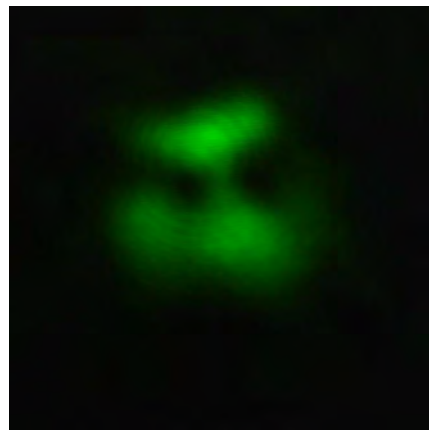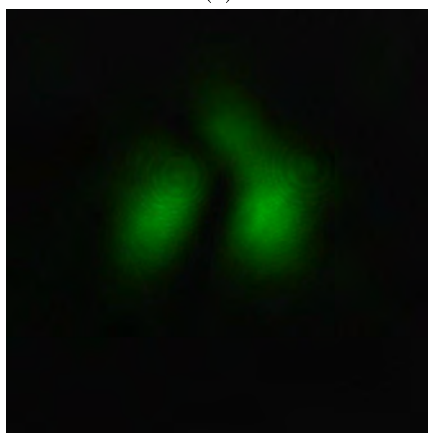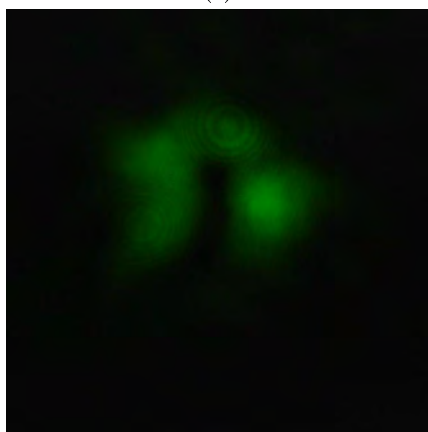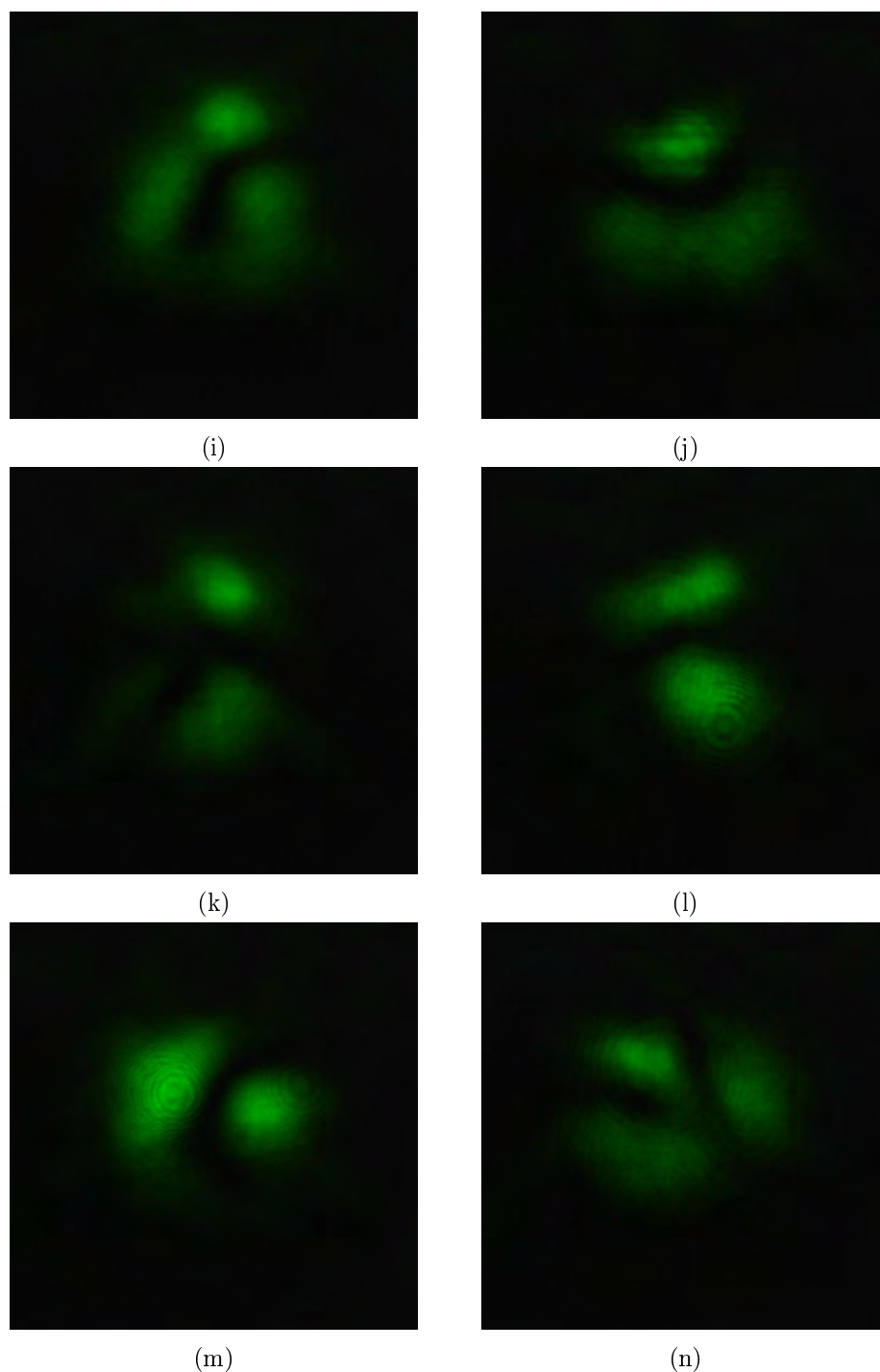
Figure 4.26: Modes obtained at port 1 (1rst column) and port 2 (2nd column) of the MMZI for sample 3 ($\lambda/4$ WP). The entrance beam to the interferometer has passed first through the MCA. (a),(b) interferograms at each port without PSA. PSA analyzing horizontal,(c),(d); vertical, (e),(f); $+45°$ (g),(h); $-45°$, (i),(j); circular right, (k),(l) and circular left (m),(n) polarization states.

Figure 4.27: Stokes parameters in images and numerical values provided by the SAS code for outputs at port 1 (1rst column) and port 2 (2nd column) of the MMZI for sample 3 (λ/4 WP), MCA. (a),(b) S0. (c),(d) S1. (e),(f) S2. (g),(h) S3. The obtained Stokes vectors are: [1 0.0005 -0.0426 -0.1256]$^{\intercal}$ for port 1 and [1 -0.0689 -0.0450 0.0043]$^{\intercal}$ for port 2. Exposure time of t=2ms.

(a)
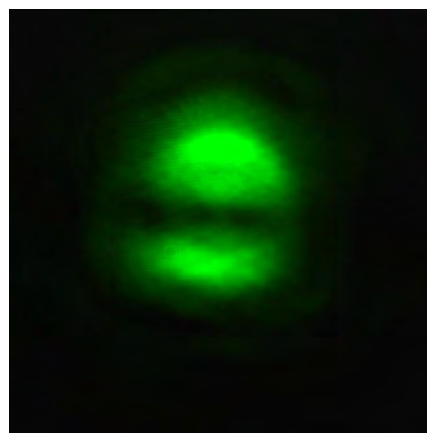
(b)
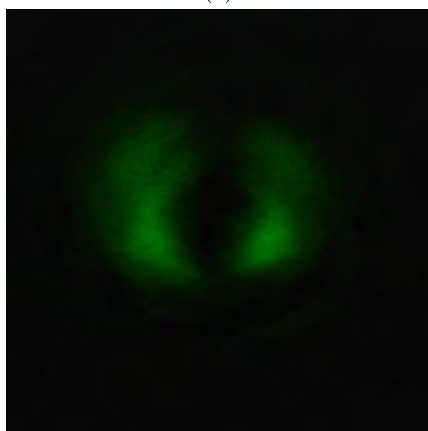
(c)
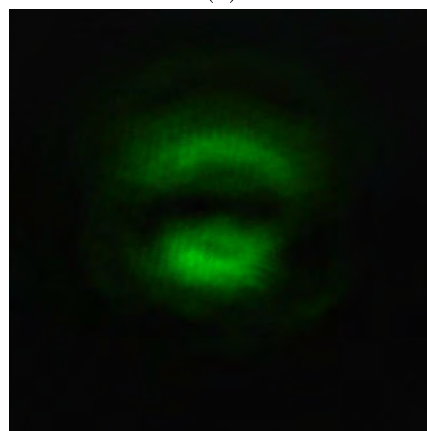
(d)
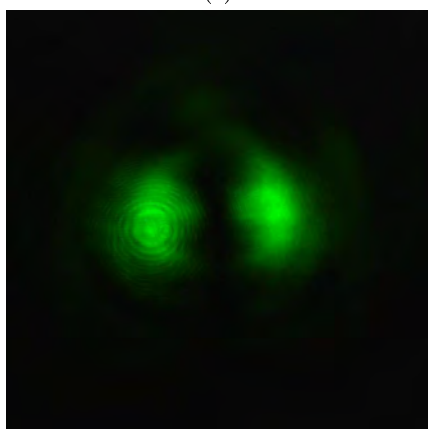
(e)
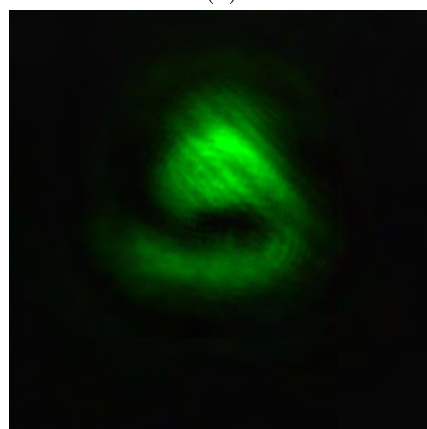
(f)
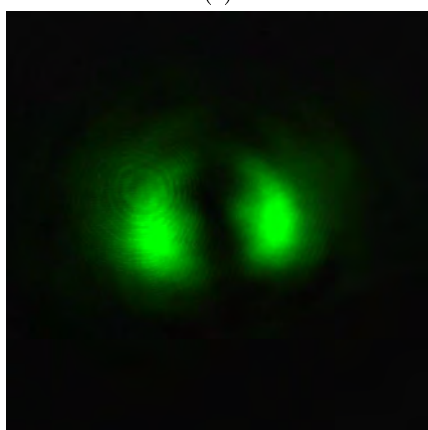
(g)
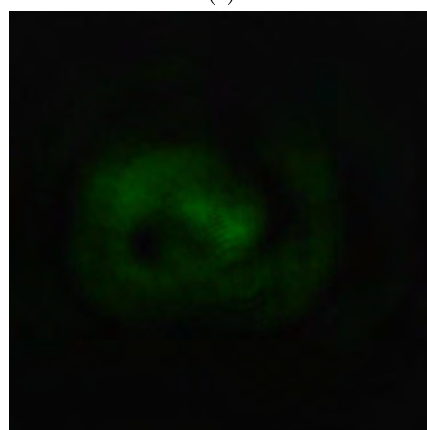
(h)
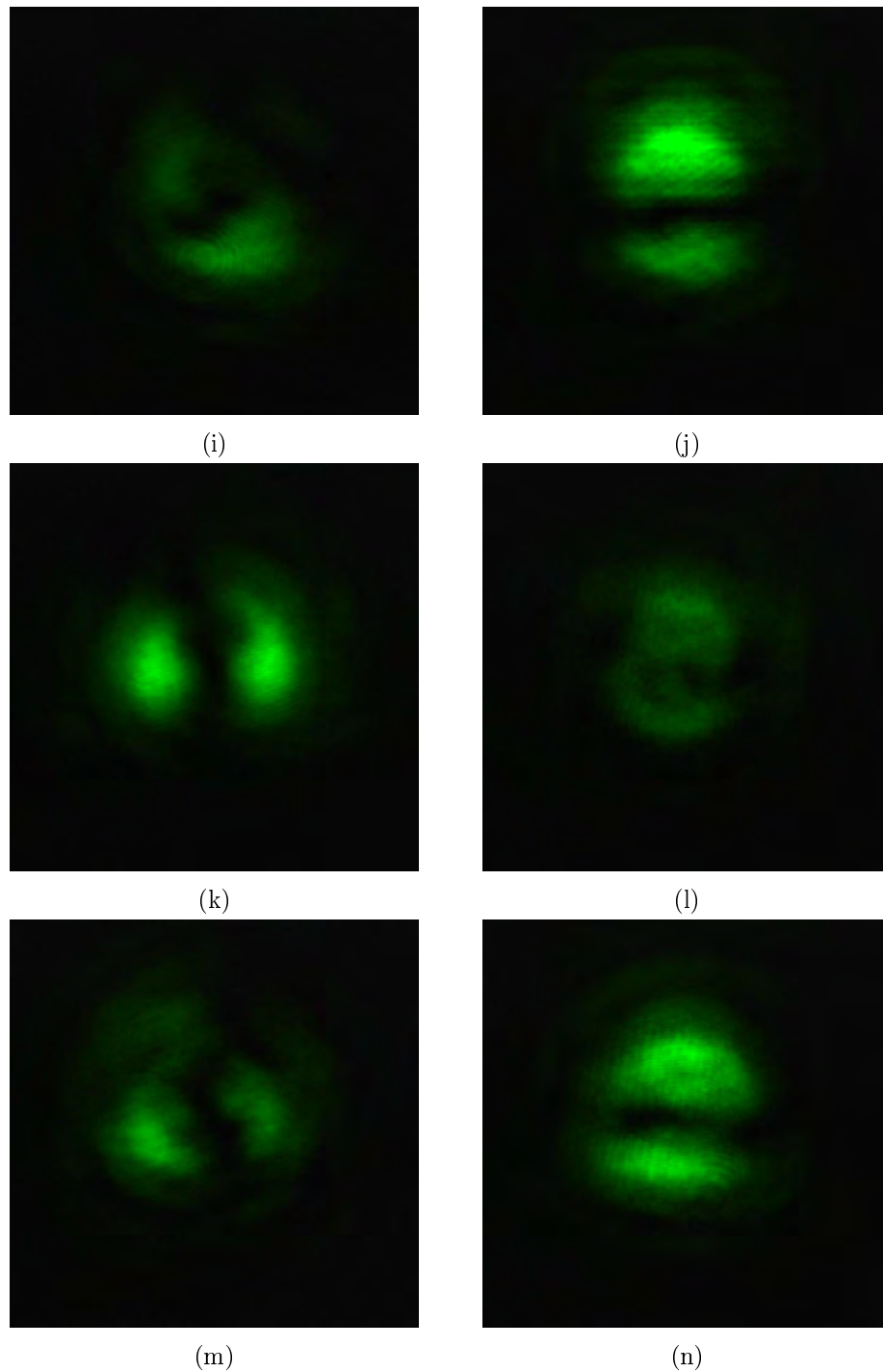
Figure 4.28: Modes obtained at port 1 (1rst column) and port 2 (2nd column) of the MMZI for sample 3 ($\lambda/4$ WP). The entrance beam to the interferometer has passed first through the MCB. (a),(b) interferograms at each port without PSA. PSA analyzing horizontal,(c),(d); vertical, (e),(f); +45° (g),(h); −45°, (i),(j); circular right, (k),(l) and circular left (m),(n) polarization states.
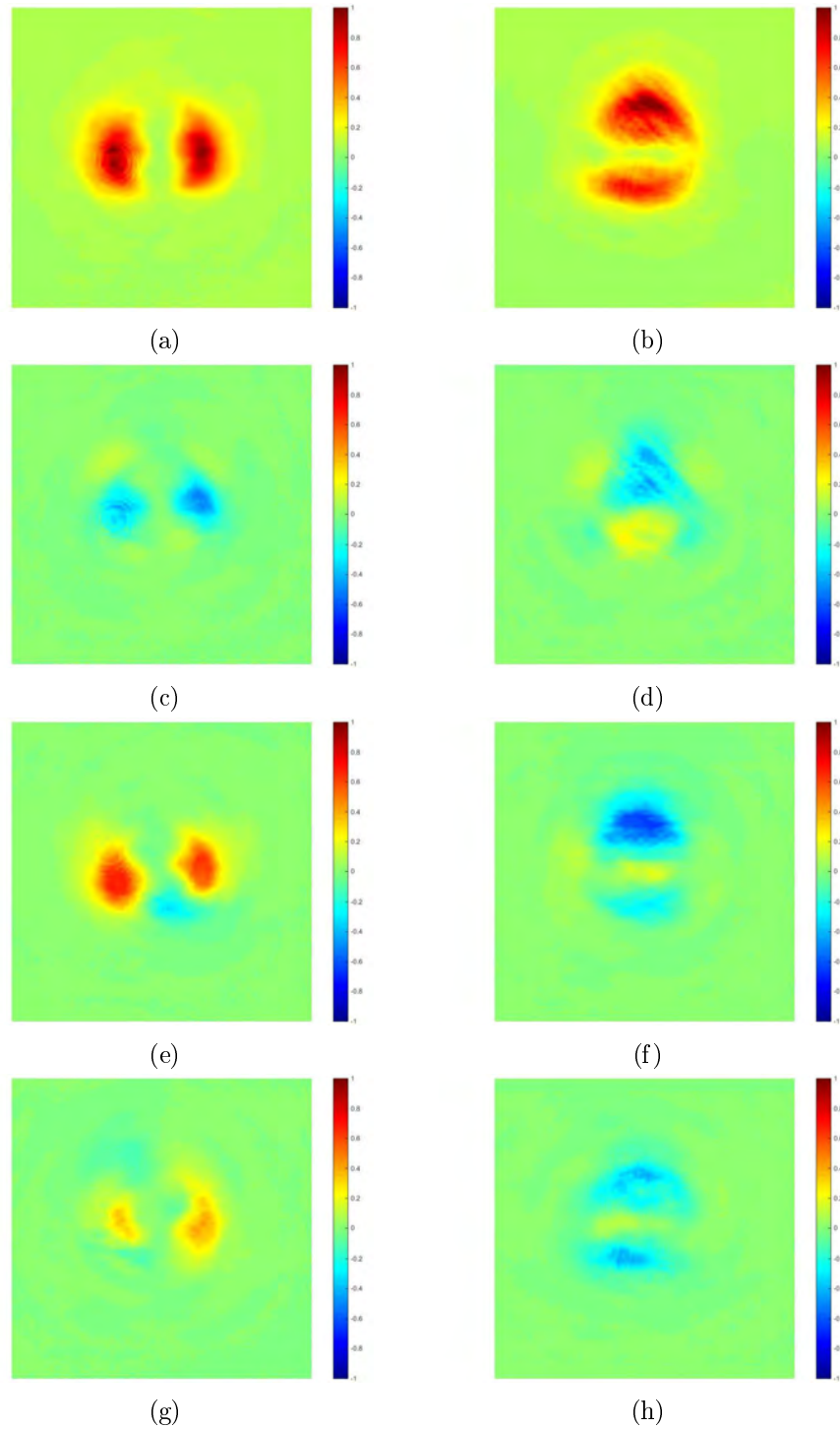
Figure 4.29: Stokes parameters in images and numerical values provided by the SAS code for outputs at port 1 (1rst column) and port 2 (2nd column) of the MMZI for sample 3 ($\lambda/4$ WP), MCB. (a),(b) S0. (c),(d) S1. (e),(f) S2. (g),(h) S3. The obtained Stokes vectors are: [1 -0.1222 0.2579 0.1002]$^\intercal$ for port 1 and [1 -0.0770 -0.2134 -0.2019]$^\intercal$ for port 2. Exposure time of t=2ms.
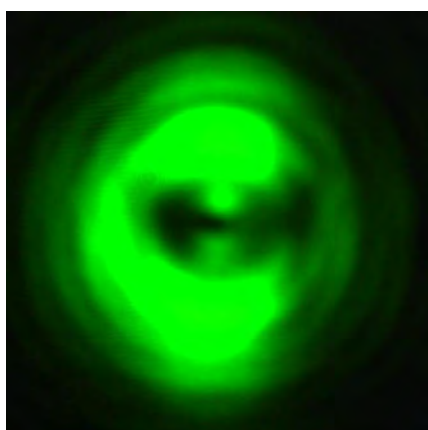
(a)
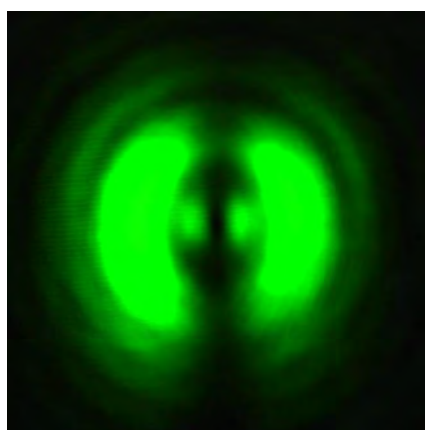
(b)
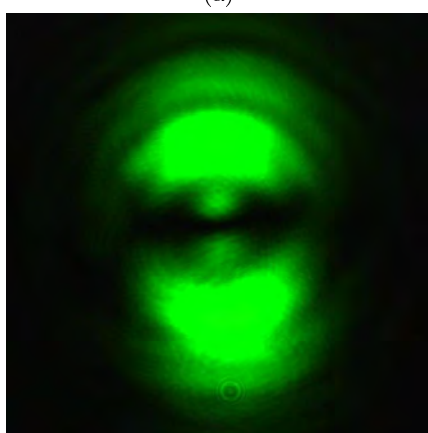
(c)
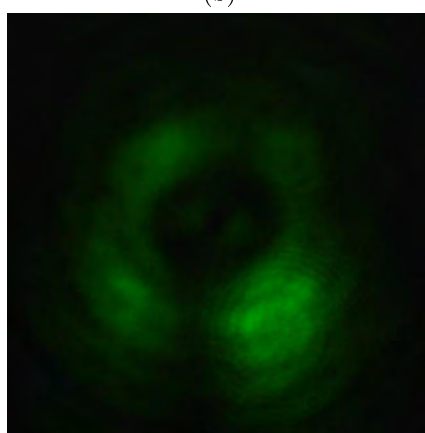
(d)
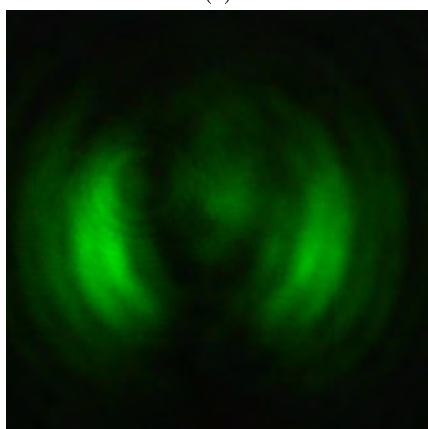
(e)
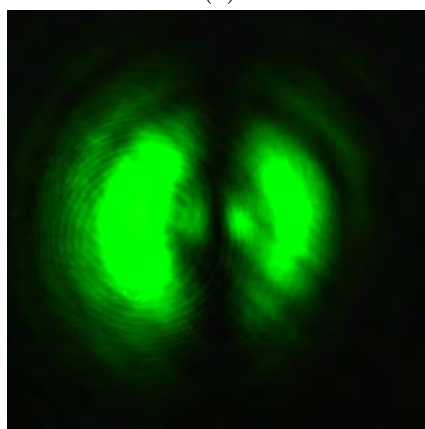
(f)
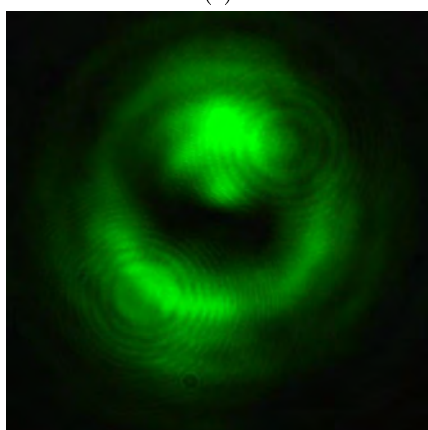
(g)
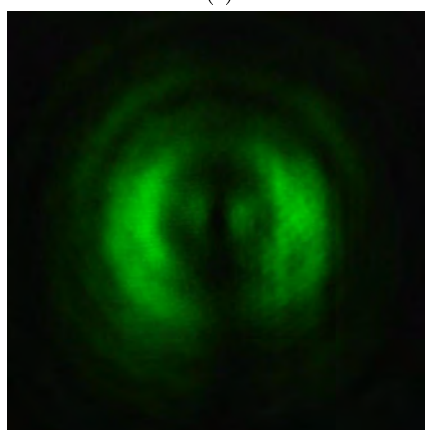
(h)
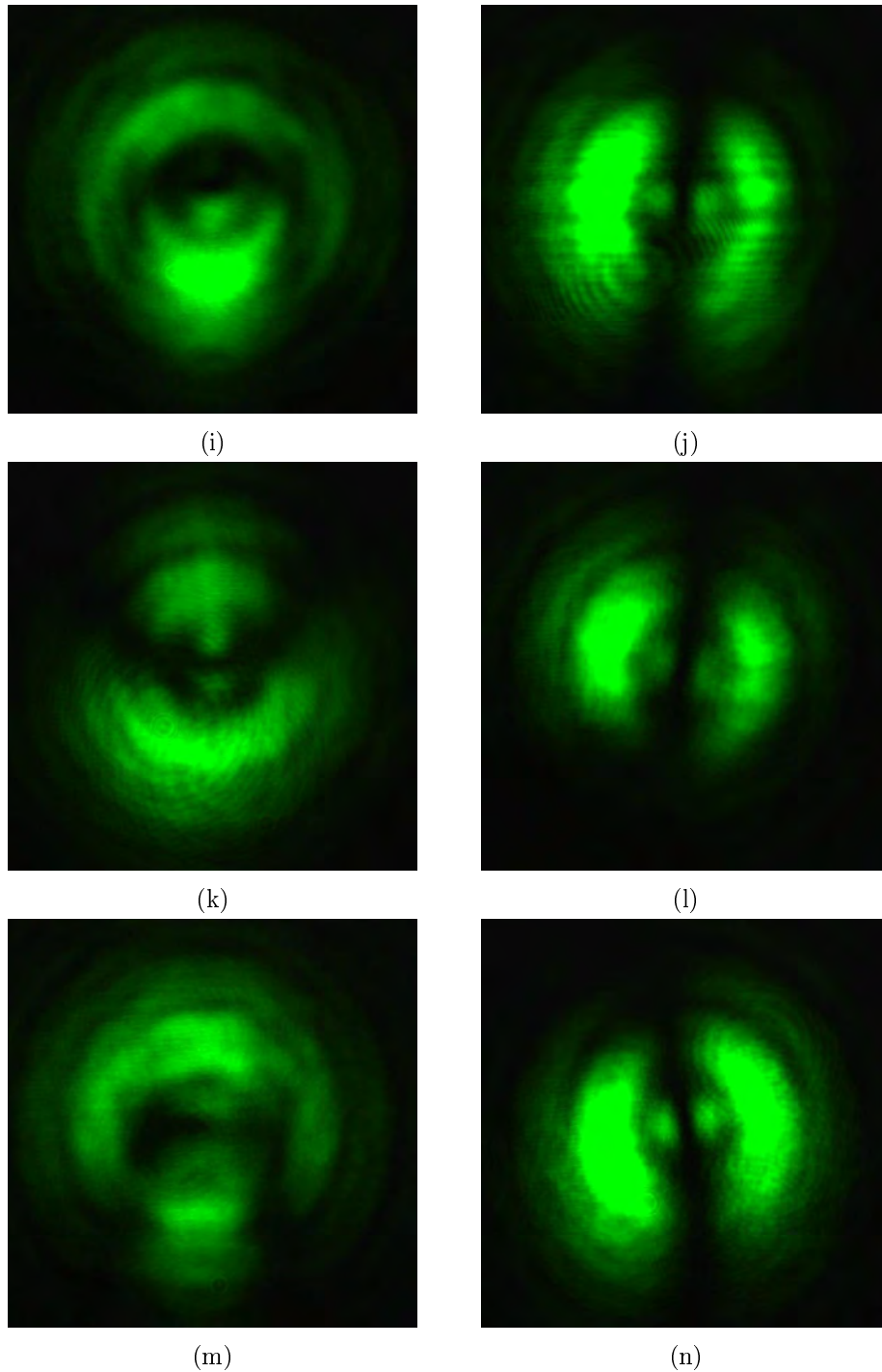
Figure 4.30: Modes obtained at port 1 (1rst column) and port 2 (2nd column) of the MMZI for sample 3 ($\lambda/4$ WP). The entrance beam to the interferometer has passed first through the MCC. (a),(b) interferograms at each port without PSA. PSA analyzing horizontal,(c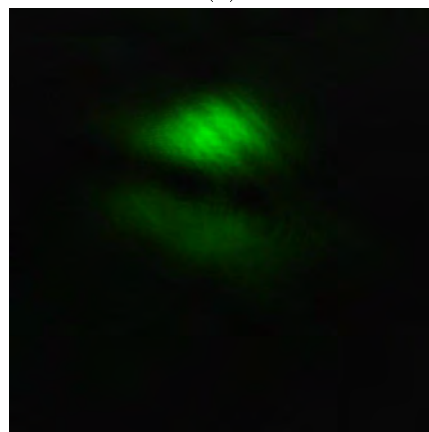),(d); vertical, (e),(f); $+45°$ (g),(h); $-45°$, (i),(j); circular right, (k),(l) and circular left (m),(n) polarization states.

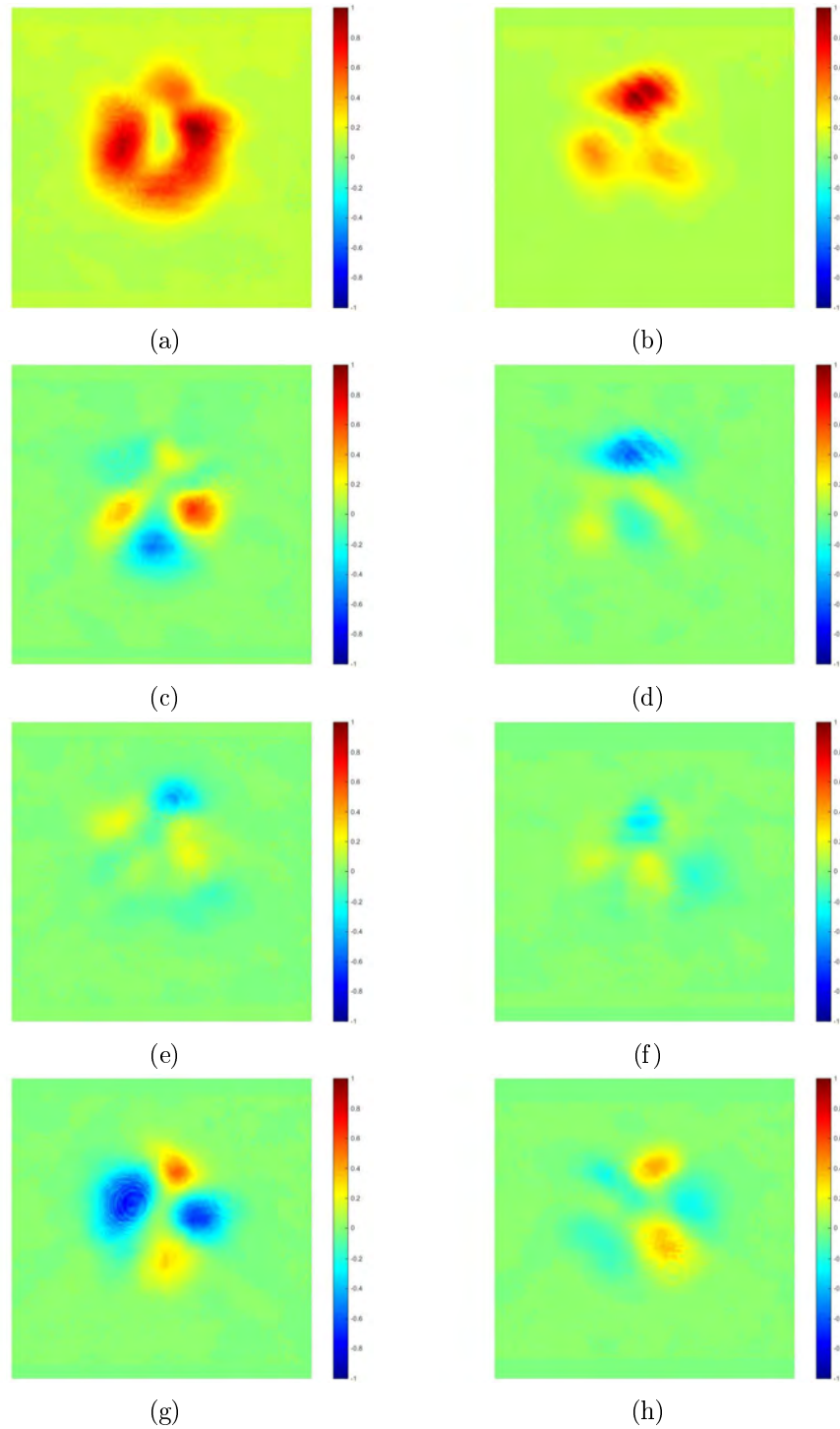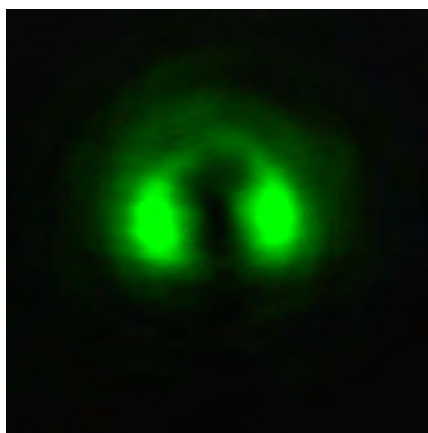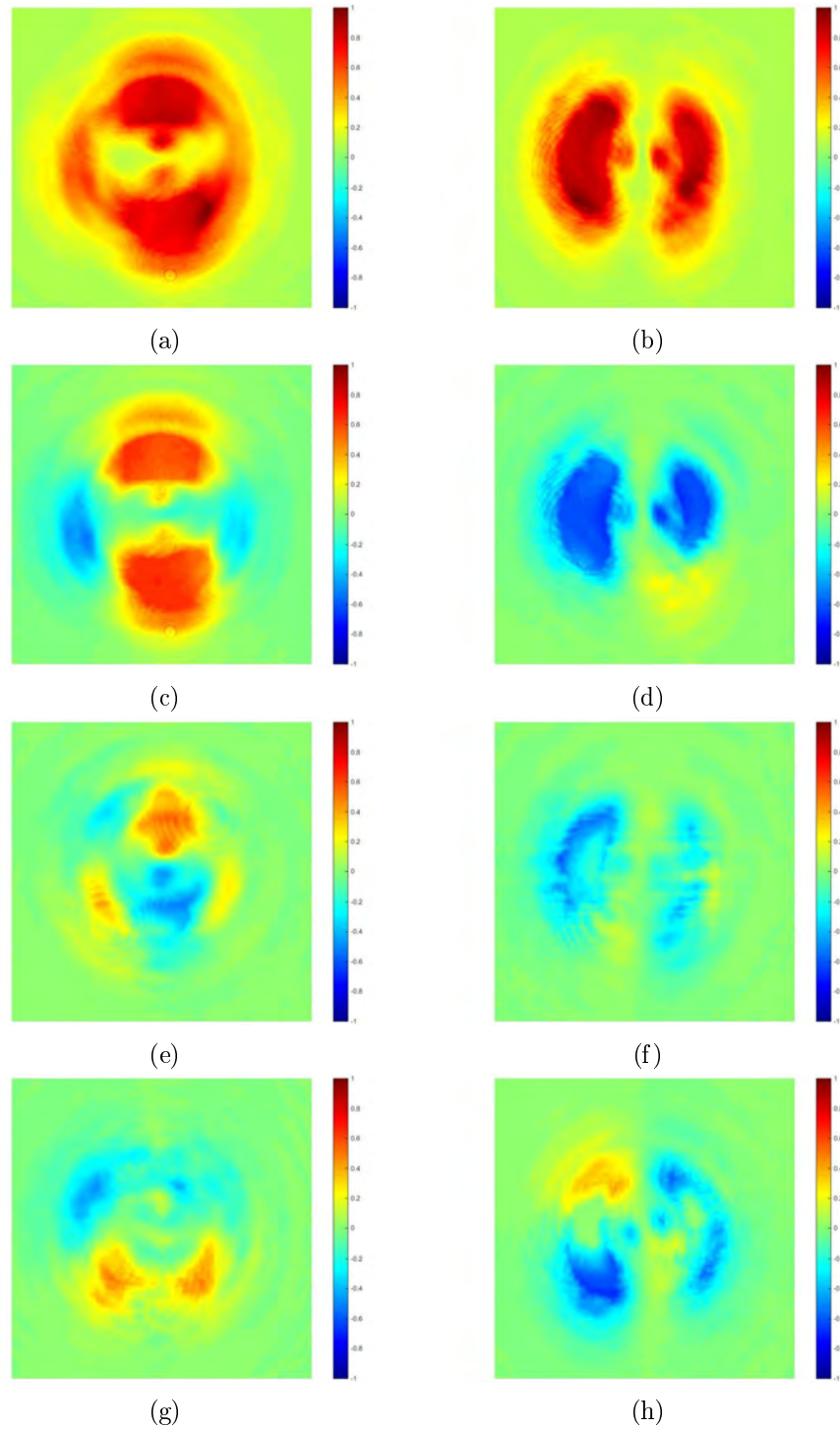Figure 4.31: Stokes parameters in images and numerical values provided by the SAS code for outputs at port 1 (1rst column) and port 2 (2nd column) of the MMZI for sample 3 ($\lambda/4$ WP), MCC. (a),(b) S0. (c),(d) S1. (e),(f) S2. (g),(h) S3. The obtained Stokes vectors are: $[1\ 0.2372\ 0.0280\ -0.0262]^{\intercal}$ for port 1 and $[1\ -0.3668\ -0.2318\ -0.2084]^{\intercal}$ for port 2. Exposure time of t=2ms.
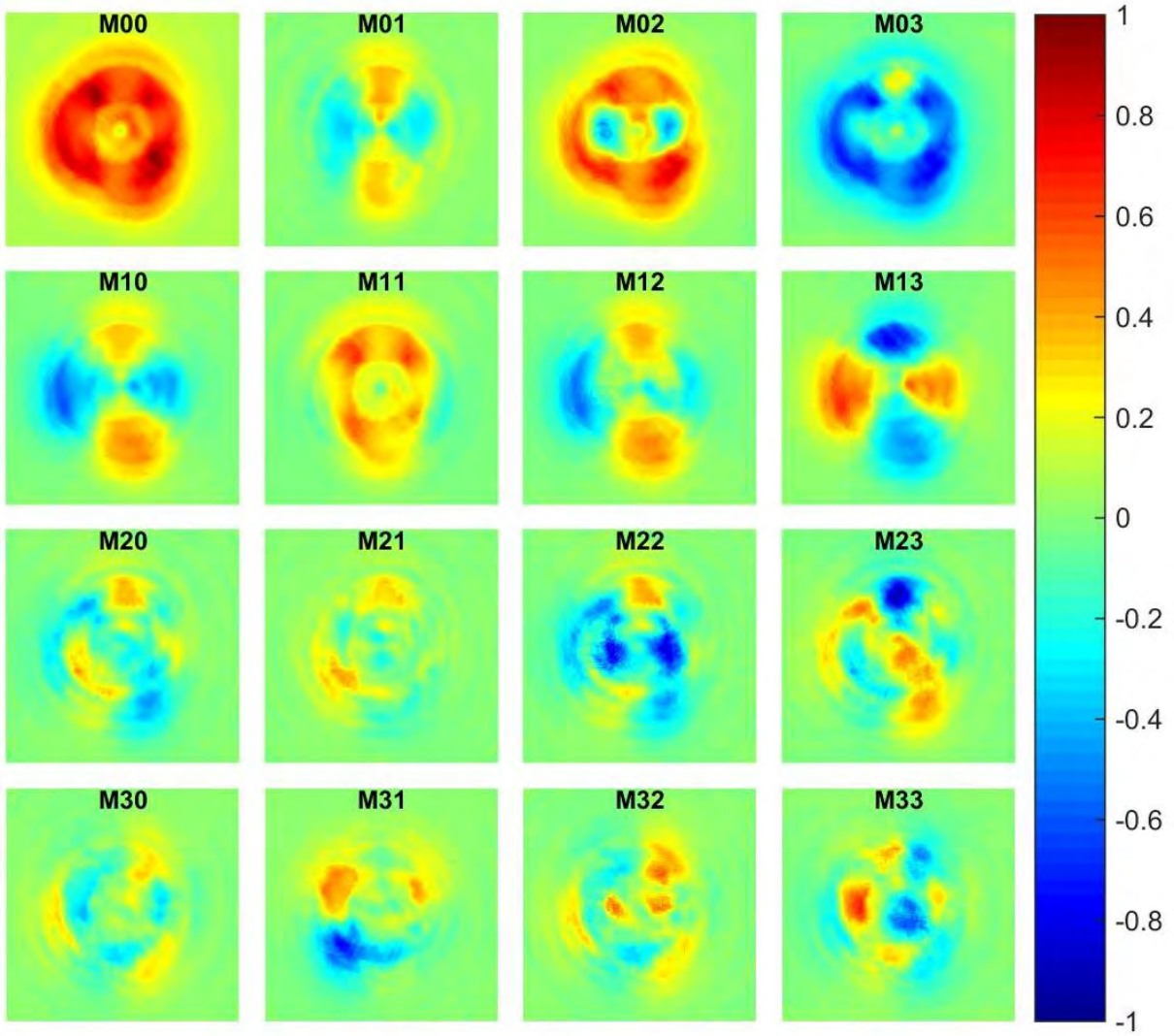
Figure 4.32: Experimental Mueller matrix for $\lambda/4$ WP.

Finally, the Mueller matrix elements for the $\lambda/4$ WP were obtained using the expressions in Appendix A and they are shown in Figure 4.32 for images and in equation 4.10 for numerical values.

$$\mathbf{M_{Unc}}^{\lambda/4} = \begin{bmatrix} 1{,}0000 & 0{,}0861 & 0{,}5362 & -0{,}6111 \\ -0{,}0392 & 0{,}2967 & 0{,}0175 & 0{,}0123 \\ -0{,}0690 & 0{,}0893 & -0{,}2179 & 0{,}0306 \\ 0{,}0430 & 0{,}0186 & 0{,}0983 & -0{,}0626 \end{bmatrix} \tag{4.10}$$

When analyzing the obtained Mueller matrices of our samples using unconventional polarization presented in this Chapter, it is important to take into account that our system is too complex, where its alignment implies a lot of mechanical mounts and optical components. The results presented here could be improved with the use of nanopositioners, super-achromatic waveplate retarders, a CMOS camera at each MMZI port, among many other high-quality components.

Chapter 5

Conclusions and future work

Learn from yesterday, live for today, hope for tomorrow.

Albert Einstein

SUMMARY: We present the conclusions derived from this thesis work along with several proposals to improve the experimental arrangement and the obtained results.

5.1. Conclusions

Based on our results and observations through all this thesis work, we can conclude:

- *About the $\pi/2$ converter.* It is of a great importance for the beam impinging on the mode converter to be correctly mode-matched to the cylinder lenses; otherwise we can have a huge distortion of the geometry of the beam which gets worst with beam propagation.

- *About the mode beam splitter (MMZI).* We have seen that the mode beam splitter needs micrometer precision mountings for the third mirror and the 2nd beam splitter, the latter needing also a rotatory mounting which allow us to center it to both arms in the interferometer. If we do not have these resources, any fine adjustment of the interferometer can take several hours of much patience.

- Once aligned, the visibility of the modes at the output ports of the MMZI purely depends on the phase difference between the arms of the interferometer. So, it becomes a necessity to have a method that allow us to know this phase difference when placing the 3rd mirror, otherwise we can spend a lot of time aligning an interferometer that will not exhibit the desired mode beam splitter behavior.

- It is necessary also to reach a strong polarizing beam splitter behavior of the interferometer in order to correctly retrieve the Mueller matrix of the sample, since we have seen a direct relationship between the magnitudes of some matrix elements and the magnitude of the Stokes parameter at which the output beam should show a tendency depending on which mode converter the beam has passed through before; S1 for MCC, S2 for MCB and S3 for MCA. For example, for our best polarization behavior result, which was for the MCC analyzing air, we found that the M11 element of the corresponding Mueller matrix had a

numerical value of 0.5261 while the S1 parameter of the interferograms was of 0.5040 for port 1 and -0.5483 for port 2. The theoretical expected values for these cases were 1, 1, 1, respectively. We can also verify the opposite case, as for MCB analyzing $\lambda/2$ WP: We had a S2 parameter of 0.0745 for port 1 and -0.2817 for port 2. The corresponding M22 element has a value of -0.0628, the expected values were 1,-1, -1, respectively.

- The polarizing behavior of the interferometer strongly depends on the symmetry of the interfering beams. We have seen that our best results are for the MCC analyzing air, which is the beam that best preserves its original shape. Our worst results are for MCA, which is the mode converter that most distorts the original symmetry of the beam.

- We have observed that, because of the important difference in the number of the optical elements that compose each mode converter, there is a considerable lost of intensity in the images from MCA, which can lead to incorrect data when comparing these images with the ones obtained from the other 2 mode converters. This can result in inaccuracies when determining the Mueller matrix of the sample.

- Through the implementation of the experimental optical arrangement, it was possible to successfully modify the spatial and polarization degrees of freedom of a classically entangled beam of light, the azimuthal beam, and to use the collected information in order to recover the Mueller matrix of the sample under study, which was the purpose of the arrangement as proposed by Töppel et al. (2014) and our general objective in this thesis work: To exploit the classical entanglement property of an azimuthally polarized beam of light to extract useful information of transparent non depolarizing samples.

- The work presented here is the sum of the achievements of the individual stages of the complete setup. In order to finally obtain the Mueller matrix of a sample, we firstly had to obtain the best possible results on each stage, say, the best azimuthal beam provided by the S-waveplate, the best mode-conversion provided by the mode converters A and B, the correct functioning of the MMZI and finally the assemble of all these elements to obtain the searched data. This well-defined, methodological form of work, allow us to say that the presented results are the best that can be obtained according to our present resources and conditions. We are able also to identify how each individual result affects the resultant Mueller matrix and to propose ideas to improve the experimental data.

5.2.   Future work

Based on the experience gained while working with the different modules of this arrangement, we propose the following ideas in order to improve the obtained results:

- One way to compensate for difference in the intensity transmitted through each mode converter, is to measure the intensity lost in each one in order to determine the lowest transmittance value and place neutral density filters where needed in order to have the same losses in all converters. This will allow to correctly compensate for the undesired intensity changes intrinsic to the optical arrangement. In this way, we will have a better comparison between images when doing the Mueller matrix computation, since any change in intensity will be due to phase difference in the interferometer, as is theoretically expected. As can be imagined, the largest lost occurs in the mode converter A, so, we can take the transmitted intensity from this converter as our reference value in order to have the same transmittance in mode converters B and C.

- Something to take into account is that the length of the cross section of the resultant interferograms has to be the same for all mode converters. The way we compensated in this work for little deviations caused by the experimental setup, was through scaling factors in the image processing. Though, the best way will be to experimentally adjust the beam to have the same size in all cases and/or improving the algorithms proposed here.

- One aspect that affected our experimental results, was the presence of noisy data in the MCC images, the ones with highest intensity, that was caused by the use of the diaphragm at the beginning of the arrangement. As explained before, this diaphragm allow us for fine experimental adjustment in the mode-matching process. However, the best situation would be to directly collimate the light to the needed beam-waist size, in order to use the entire intensity of the beam and avoid undesired effects, as the ones presented here.

- Because of the high sensitivity to any change in environmental conditions exhibited by the interferometer, it is necessary to have an active compensation method that allows for phase difference maintenance between optical paths and thus a larger stabilization of the system during measurements.

Appendix A

Appendix. Töppel's expressions to find the Mueller matrix of a sample

Here we show the analytic expressions derived by Töppel in his work Töppel et al. (2014). These relationships allow us to find the Two Degree of Fredoom Stokes parameters; a matrix that is directly related with the Mueller matrix. In the case of azimuthal polarization, this relationship reads as:

$$M_{\mu\nu} = \begin{cases} S_{\mu\nu}, & \text{if } \nu = 0 \\ -S_{\mu\nu}, & \text{otherwise} \end{cases} \tag{A.1}$$

The $S_{\mu\nu}$ elements are directly obtained from:

$$
\begin{aligned}
S_{00} &= I_{00} + I_{01} + I_{10} + I_{11} \\
S_{01} &= -I_{00} - I_{01} + 2I_{02} - I_{10} - I_{11} + 2I_{12} \\
S_{02} &= -I_{00} - I_{01} + 2I_{03} - I_{10} - I_{11} + 2I_{13} \\
S_{03} &= I_{00} - I_{01} + I_{10} - I_{11} \\
S_{10} &= -I_{00} - I_{01} - I_{10} - I_{11} + 2(I_{20} + I_{21}) \\
S_{11} &= I_{00} + I_{01} - 2I_{02} + I_{10} + I_{11} - 2(I_{12} + I_{20} + I_{21} - 2I_{22}) \\
S_{12} &= I_{00} + I_{01} - 2I_{03} + I_{10} + I_{11} - 2(I_{13} + I_{20} + I_{21} - 2I_{23}) \\
S_{13} &= -I_{00} + I_{01} - I_{10} + I_{11} + 2I_{20} - 2I_{21} \\
S_{20} &= -I_{00} - I_{01} - I_{10} - I_{11} + 2(I_{30} + I_{31}) \\
S_{21} &= I_{00} + I_{01} - 2I_{02} + I_{10} + I_{11} - 2(I_{12} + I_{30} + I_{31} - 2I_{32}) \\
S_{22} &= I_{00} + I_{01} - 2I_{03} + I_{10} + I_{11} - 2(I_{13} + I_{30} + I_{31} - 2I_{33}) \\
S_{23} &= -I_{00} + I_{01} - I_{10} + I_{11} + 2I_{30} - 2I_{31} \\
S_{30} &= I_{00} + I_{01} - I_{10} - I_{11} \\
S_{31} &= -I_{00} - I_{01} + 2I_{02} + I_{10} + I_{11} - 2I_{12} \\
S_{32} &= -I_{00} - I_{01} + 2I_{03} + I_{10} + I_{11} - 2I_{13} \\
S_{33} &= I_{00} - I_{01} - I_{10} + I_{11}
\end{aligned}
\tag{A.2}
$$

With the μ index indicating polarization: $\{0 \equiv horizontal, 1 \equiv vertical, 2 \equiv +45°, 3 \equiv L\}$, and the ν index indicating mode: $\{0 \equiv \Psi_{10}, 1 \equiv \Psi_{01}, 2 \equiv \Psi_+, 3 \equiv \Psi_L\}$.[*]

---

[*]Notice that the index 3 corresponds to left polarization and mode in Töppel´s article, which works with the "looking to the direction of propagation" convention. We respected this convention in the theoretical analysis but, since we are working in the "looking to the source" convention, this index will correspond to right polarization and mode in our experimental measurements.

Appendix B

Appendix. Experimental procedure to find the phase retardation and direction of the fast axis of a waveplate

In order to determine the phase retardation ϕ and the direction of the fast axis of our waveplates (WP) samples, we followed the experimental procedure presented in Collet (1993), which is depicted in Figure B.1.
The procedure is as follows:

- The waveplate (WP) is placed between two crossed linear polarizers: The transmission axes of the first polarizer and second polarizer are in the x and y directions, respectively, as shown in Figure B.1.

- The mounting of the waveplate is rotated until we achieve again a minimum transmission through the analyzing polarizer (transmission axis at $90°$). At this orientation we have the fast axis of the waveplate aligned with the horizontal direction.

- Once in this configuration, we measure the intensity registered by the photodetector when the transmission axis of the analyzer is at $90°$ (intensity labelled as $I(0°, \phi)$) and when it is at $90°$ (labelled as $I(90°, \phi)$.

The phase retardation ϕ of the waveplate is obtained through the Equation (Collet, 1993)

$$\cos(\phi) = \frac{I(0°, \phi) - I(90°, \phi)}{I(0°, \phi) + I(90°, \phi)} \tag{B.1}$$

.
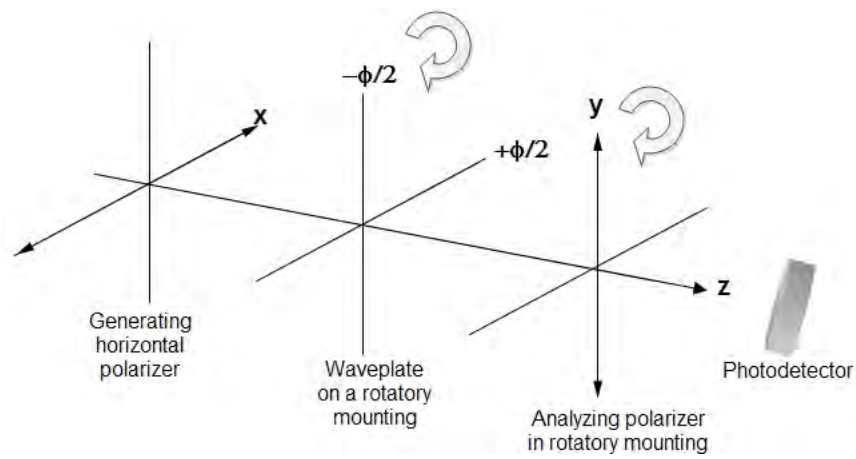
Figure B.1: Schematic diagram showing the crossed polarizer method to measure the phase retardation of a waveplate. Adapted from Collet (1993).

Appendix C

Appendix. Algorithms employed in this thesis work

C.1. Algorithm to compute the Mueller matrix through images following the ideal polarimetric arrangement (IPA) method

```matlab
%Program to obtain the Mueller matrix of a sample using the IPA method.
%This method is based in the generation and analysis of conventional
%polarization.
%By Jacqueline Muro.
%V1.0 13/06/2017
%Initializing and loading images
clear all; close all; clc;
ImgHH=imread('IHHt0_30.jpg');
ImgHV=imread('IHVt0_30.jpg');
ImgH45=imread('IH+t0_30.jpg');
ImgHR=imread('IHRt0_30.jpg');
ImgVH=imread('IVHt0_30.jpg');
ImgVV=imread('IVVt0_30.jpg');
ImgV45=imread('IV+t0_30.jpg');
ImgVR=imread('IVRt0_30.jpg');
Img45H=imread('I+Ht0_30.jpg');
Img45V=imread('I+Vt0_30.jpg');
Img4545=imread('I++t0_30.jpg');
Img45R=imread('I+Rt0_30.jpg');
ImgRH=imread('IRHt0_30.jpg');
ImgRV=imread('IRVt0_30.jpg');
ImgR45=imread('IR+t0_30.jpg');
ImgRR=imread('IRRt0_30.jpg');
%% Processing images
rad=300; %half the size of the cropped image
[ImgHHc,ImHHc]=ImageCrop2(ImgHH,rad);
imwrite(uint8(ImHHc),'ImHHc.jpg','jpg');
imwrite(ImgHHc,'ImHHgc.jpg','jpg');
[ImgHVc,ImHVc]=ImageCrop2(ImgHV,rad);
imwrite(uint8(ImHVc),'ImHVc.jpg','jpg');
imwrite(ImgHVc,'ImHVgc.jpg','jpg');
[ImgH45c,ImH45c]=ImageCrop2(ImgH45,rad);
imwrite(uint8(ImH45c),'ImH45c.jpg','jpg');
imwrite(ImgH45c,'ImH45gc.jpg','jpg');
[ImgHRc,ImHRc]=ImageCrop2(ImgHR,rad);
imwrite(uint8(ImHRc),'ImHRc.jpg','jpg');
imwrite(ImgHRc,'ImHRgc.jpg','jpg');
[ImgVHc,ImVHc]=ImageCrop2(ImgVH,rad);
imwrite(uint8(ImVHc),'ImVHc.jpg','jpg');
imwrite(ImgVHc,'ImVHgc.jpg','jpg');
[ImgVVc,ImVVc]=ImageCrop2(ImgVV,rad);
imwrite(uint8(ImVVc),'ImVVc.jpg','jpg');
imwrite(ImgVVc,'ImVVgc.jpg','jpg');
[ImgV45c,ImV45c]=ImageCrop2(ImgV45,rad);
imwrite(uint8(ImV45c),'ImV45c.jpg','jpg');
imwrite(ImgV45c,'ImV45gc.jpg','jpg');
[ImgVRc,ImVRc]=ImageCrop2(ImgVR,rad);
imwrite(uint8(ImVRc),'ImVRc.jpg','jpg');
imwrite(ImgVRc,'ImVRgc.jpg','jpg');
[Img45Hc,Im45Hc]=ImageCrop2(Img45H,rad);
imwrite(uint8(Im45Hc),'Im45Hc.jpg','jpg');
imwrite(Img45Hc,'Im45Hgc.jpg','jpg');
[Img45Vc,Im45Vc]=ImageCrop2(Img45V,rad);
imwrite(uint8(Im45Vc),'Im45Vc.jpg','jpg');
imwrite(Img45Vc,'Im45Vgc.jpg','jpg');
```

```matlab
[Img4545c,Im4545c]=ImageCrop2(Img4545,rad);
imwrite(uint8(Im4545c),'Im4545c.jpg','jpg');
imwrite(Img4545c,'Im4545gc.jpg','jpg');
[Img45Rc,Im45Rc]=ImageCrop2(Img45R,rad);
imwrite(uint8(Im45Rc),'Im45Rc.jpg','jpg');
imwrite(Img45Rc,'Im45Rgc.jpg','jpg');
[ImgRHc,ImRHc]=ImageCrop2(ImgRH,rad);
imwrite(uint8(ImRHc),'ImRHc.jpg','jpg');
imwrite(ImgRHc,'ImRHgc.jpg','jpg');
[ImgRVc,ImRVc]=ImageCrop2(ImgRV,rad);
imwrite(uint8(ImRVc),'ImRVc.jpg','jpg');
imwrite(ImgRVc,'ImRVgc.jpg','jpg');
[ImgR45c,ImR45c]=ImageCrop2(ImgR45,rad);
imwrite(uint8(ImR45c),'ImR45c.jpg','jpg');
imwrite(ImgR45c,'ImR45gc.jpg','jpg');
[ImgRRc,ImRRc]=ImageCrop2(ImgRR,rad);
imwrite(uint8(ImRRc),'ImRRc.jpg','jpg');
imwrite(ImgRRc,'ImRRgc.jpg','jpg');
%% Showing cropped images
iptsetpref('ImshowBorder','tight');
figure('Name','Cropped images','units','normalized','outerposition',[0 0
1 1]);
subplot(4,4,1); imagesc(ImHHc); colormap gray; title('ImHH'); axis image;
axis off;
subplot(4,4,2); imagesc(ImHVc); colormap gray; title('ImHV'); axis image;
axis off;
subplot(4,4,3); imagesc(ImH45c); colormap gray; title('ImH+'); axis
image; axis off;
subplot(4,4,4); imagesc(ImHRc); colormap gray; title('ImHR'); axis image;
axis off;
subplot(4,4,5); imagesc(ImVHc); colormap gray; title('ImVH'); axis image;
axis off;
subplot(4,4,6); imagesc(ImVVc); colormap gray; title('ImVV'); axis image;
axis off;
subplot(4,4,7); imagesc(ImV45c); colormap gray; title('ImV+'); axis
image; axis off;
subplot(4,4,8); imagesc(ImVRc); colormap gray; title('ImVR'); axis image;
axis off;
subplot(4,4,9); imagesc(Im45Hc); colormap gray; title('Im+H'); axis
image; axis off;
subplot(4,4,10); imagesc(Im45Vc); colormap gray; title('Im+V'); axis
image; axis off;
subplot(4,4,11); imagesc(Im4545c); colormap gray; title('Im++'); axis
image; axis off;
subplot(4,4,12); imagesc(Im45Rc); colormap gray; title('Im+R'); axis
image; axis off;
subplot(4,4,13); imagesc(ImRHc); colormap gray; title('ImRH'); axis
image; axis off;
subplot(4,4,14); imagesc(ImRVc); colormap gray; title('ImRV'); axis
image; axis off;
subplot(4,4,15); imagesc(ImR45c); colormap gray; title('ImR+'); axis
image; axis off;
subplot(4,4,16); imagesc(ImRRc); colormap gray; title('ImRR'); axis
image; axis off;
saveas(gcf,'Cropped images.jpg')
```

```matlab
%% Computing Mueller elements
ImHHc=double(ImHHc); ImHVc=double(ImHVc); ImH45c=double(ImH45c);
ImHRc=double(ImHRc);
ImVHc=double(ImVHc); ImVVc=double(ImVVc); ImV45c=double(ImV45c);
ImVRc=double(ImVRc);
Im45Hc=double(Im45Hc); Im45Vc=double(Im45Vc); Im4545c=double(Im4545c);
Im45Rc=double(Im45Rc);
ImRHc=double(ImRHc); ImRVc=double(ImRVc); ImR45c=double(ImR45c);
ImRRc=double(ImRRc);

m11=(1/2).*(ImHHc+ImHVc+ImVHc+ImVVc);
m12=(1/2).*(ImHHc+ImHVc-ImVHc-ImVVc);
m13=Im45Hc+Im45Vc-(1/2).*(ImHHc+ImHVc+ImVHc+ImVVc);
m14=ImRHc+ImRVc-(1/2).*(ImHHc+ImHVc+ImVHc+ImVVc);
m21=(1/2).*(ImHHc-ImHVc+ImVHc-ImVVc);
m22=(1/2).*(ImHHc-ImHVc-ImVHc+ImVVc);
m23=Im45Hc-Im45Vc-(1/2).*(ImHHc-ImHVc+ImVHc-ImVVc);
m24=ImRHc-ImRVc-(1/2).*(ImHHc-ImHVc+ImVHc-ImVVc);
m31=ImH45c+ImV45c-(1/2).*(ImHHc+ImHVc+ImVHc+ImVVc);
m32=ImH45c-ImV45c-(1/2).*(ImHHc+ImHVc-ImVHc-ImVVc);
m33=2.*Im4545c-Im45Hc-Im45Vc-ImH45c-
ImV45c+(1/2).*(ImHHc+ImHVc+ImVHc+ImVVc);
m34=2.*ImR45c-ImRHc-ImRVc-ImH45c-ImV45c+(1/2).*(ImHHc+ImHVc+ImVHc+ImVVc);
m41=ImHRc+ImVRc-(1/2).*(ImHHc+ImHVc+ImVHc+ImVVc);
m42=ImHRc-ImVRc-(1/2).*(ImHHc+ImHVc-ImVHc-ImVVc);
m43=2.*Im45Rc-Im45Hc-Im45Vc-ImHRc-ImVRc+(1/2).*(ImHHc+ImHVc+ImVHc+ImVVc);
m44=2.*ImRRc-ImRHc-ImRVc-ImHRc-ImVRc+(1/2).*(ImHHc+ImHVc+ImVHc+ImVVc);
%% Obtaining numerical Mueller matrix
Anorm=mean(mean(m11));
M(1,1)=1; M(1,2)=mean(mean(m12))/Anorm; M(1,3)=mean(mean(m13))/Anorm;
M(1,4)=mean(mean(m14))/Anorm;
M(2,1)=mean(mean(m21))/Anorm; M(2,2)=mean(mean(m22))/Anorm;
M(2,3)=mean(mean(m23))/Anorm; M(2,4)=mean(mean(m24))/Anorm;
M(3,1)=mean(mean(m31))/Anorm; M(3,2)=mean(mean(m32))/Anorm;
M(3,3)=mean(mean(m33))/Anorm; M(3,4)=mean(mean(m34))/Anorm;
M(4,1)=mean(mean(m41))/Anorm; M(4,2)=mean(mean(m42))/Anorm;
M(4,3)=mean(mean(m43))/Anorm; M(4,4)=mean(mean(m44))/Anorm;
%% Showing normalized Mueller matrix as images
norm=max(max(m11));
h=figure('Name','Optical normalized Mueller
matrix','units','normalized','outerposition',[0 0 1 1]);
h.PaperPositionMode = 'auto'; %for saving the image at it appears on
screen
set(h,'visible','off'); %hide the figure while we are changing its
properties
iptsetpref('ImshowBorder','tight'); %remove innecesary white space
subplot(4,4,1); imagesc(m11/norm); colormap jet; axis image; axis off;
caxis([-1 1]);
subplot(4,4,2); imagesc(m12/norm); colormap jet; axis image; axis off;
caxis([-1 1]);
subplot(4,4,3); imagesc(m13/norm); colormap jet; axis image; axis off;
caxis([-1 1]);
subplot(4,4,4); imagesc(m14/norm); colormap jet; axis image; axis off;
caxis([-1 1]);
subplot(4,4,5); imagesc(m21/norm); colormap jet; axis image; axis off;
caxis([-1 1]);
```

```matlab
subplot(4,4,6); imagesc(m22/norm); colormap jet; axis image; axis off;
caxis([-1 1]);
subplot(4,4,7); imagesc(m23/norm); colormap jet; axis image; axis off;
caxis([-1 1]);
subplot(4,4,8); imagesc(m24/norm); colormap jet; axis image; axis off;
caxis([-1 1]);
subplot(4,4,9); imagesc(m31/norm); colormap jet; axis image; axis off;
caxis([-1 1]);
subplot(4,4,10); imagesc(m32/norm); colormap jet; axis image; axis off;
caxis([-1 1]);
subplot(4,4,11); imagesc(m33/norm); colormap jet; axis image; axis off;
caxis([-1 1]);
subplot(4,4,12); imagesc(m34/norm); colormap jet; axis image; axis off;
caxis([-1 1]);
subplot(4,4,13); imagesc(m41/norm); colormap jet; axis image; axis off;
caxis([-1 1]);
subplot(4,4,14); imagesc(m42/norm); colormap jet; axis image; axis off;
caxis([-1 1]);
subplot(4,4,15); imagesc(m43/norm); colormap jet; axis image; axis off;
caxis([-1 1]);
subplot(4,4,16); imagesc(m44/norm); colormap jet; axis image; axis off;
caxis([-1 1]);
f=0;%counter for the number of subfigure;
xant=0; l=0;%initial x and factor shift for subplots
for i=0:3 %two fors for easy labeling of each subfigure
    for j=0:3
        l=l+1; %control of shifting of figure
        f=f+1; %updating subfigure counter
        sp_hand1 = subplot(4,4,f); %calling handle of subfigure
        pos1 = get(sp_hand1, 'Position'); % obtaining the position of
current sub-plot
        new_pos1 = pos1 +[xant 0 0.04 0.04]; %defining new position
        set(sp_hand1, 'Position',new_pos1 ); % setting new position of
current sub - plot
        v = axis; %For the title position
        handle=title(['M',num2str(i), num2str(j)]); %Assigning the title
of the graphic
        set(handle,'Position',[v(2)/2 v(4)*0.12 0]); %Placing the title
        xant=(-new_pos1(3)/2+.003)*l; %defining new x coordinate
    end
    xant=0; l=0; %resetting values for new row
end
%Placing one color bar for all subfigures; taking as reference the
position
%of the last subfigure.
colorbar('Position', [new_pos1(1)+new_pos1(3)-0.04  new_pos1(2)  0.03
new_pos1(2)+new_pos1(3)*3.78],'fontsize',12)
drawnow
set(h,'visible','on'); %Showing figure
saveas(gcf,'Normalized Mueller Matrix IPA.jpg')
```

C.2. Algorithm to compute the Mueller matrix through images following Töppel´s expressions

```
%Program to obtain the Mueller matrix of a sample using azimuthal
%polarization.
%By Jacqueline Muro
%V1.0 01/06/2017
%V1.1 12/07/2017 Section to improve the format of the Mueller matrix
figure is added
clear all; close all; clc;
%% Loading cropped images
% From MCC MBS HG10 (horizontal mode)
Im00=double(imread('MCCHAzHt2c.jpg'));
Im10=double(imread('MCCHAzVt2c.jpg'));
Im20=double(imread('MCCHAz45t2c.jpg'));
Im30=double(imread('MCCHAzRt2c.jpg'));
% From MCC MBS HG01 (vertical mode)
Im01=double(imread('MCCVAzHt2c.jpg'));
Im11=double(imread('MCCVAzVt2c.jpg'));
Im21=double(imread('MCCVAz45t2c.jpg'));
Im31=double(imread('MCCVAzRt2c.jpg'));
%% From MCA (Pi/2 mode converter) MBS HG01 (vertical mode)
Im03=double(imread('MCAVAzHt2c.jpg'));
Im13=double(imread('MCAVAzVt2c.jpg'));
Im23=double(imread('MCAVAz45t2c.jpg'));
Im33=double(imread('MCAVAzRt2c.jpg'));
%% From MCB (Pi Converter) MBS HG10 (horizontal mode)
Im02=double(imread('MCBHAzHt2c.jpg'));
Im12=double(imread('MCBHAzVt2c.jpg'));
Im22=double(imread('MCBHAz45t2c.jpg'));
Im32=double(imread('MCBHAzRt2c.jpg'));
%% Computing S elements
ImS00=Im00+Im01+Im10+Im11; S(1,1)=mean(mean(ImS00));
ImS03=Im00-Im01+Im10-Im11; S(1,4)=mean(mean(ImS03));
ImS10=-Im00-Im01-Im10-Im11+2.*(Im20+Im21); S(2,1)=mean(mean(ImS10));
ImS13=-Im00+Im01-Im10+Im11+2.*(Im20-Im21); S(2,4)=mean(mean(ImS13));
ImS20=-Im00-Im01-Im10-Im11+2.*(Im30+Im31); S(3,1)=mean(mean(ImS20));
ImS23=-Im00+Im01-Im10+Im11+2.*(Im30-Im31); S(3,4)=mean(mean(ImS23));
ImS30=Im00+Im01-Im10-Im11; S(4,1)=mean(mean(ImS30));
ImS33=Im00-Im01-Im10+Im11; S(4,4)=mean(mean(ImS33));
%% Computing S elements for the MCA MBS (Pi2 converter)
ImS02=-Im00-Im01+2.*Im03-Im10-Im11+2.*Im13; S(1,3)=mean(mean(ImS02));
ImS12=Im00+Im01-2.*Im03+Im10+Im11-2.*(Im13+Im20+Im21-2.*Im23);
S(2,3)=mean(mean(ImS12));
ImS22=Im00+Im01-2.*Im03+Im10+Im11-2.*(Im13+Im30+Im31-2.*Im33);
S(3,3)=mean(mean(ImS22));
ImS32=-Im00-Im01+2.*Im03+Im10+Im11-2.*Im13; S(4,3)=mean(mean(ImS32));
%% Computing S elements for the MCB MBS
ImS01=-Im00-Im01+2.*Im02-Im10-Im11+2.*Im12; S(1,2)=mean(mean(ImS01));
ImS11=Im00+Im01-2.*Im02+Im10+Im11-2.*(Im12+Im20+Im21-2.*Im22); S(2,2)=
mean(mean(ImS11));
ImS21=Im00+Im01-2.*Im02+Im10+Im11-2.*(Im12+Im30+Im31-2.*Im32);
S(3,2)=mean(mean(ImS21));
ImS31=-Im00-Im01+2.*Im02+Im10+Im11-2.*Im12;   S(4,2)=mean(mean(ImS31));
%% Finding Mueller matrix for azimuthal polarization as probe beam
Sn=S./S(1,1);
M=[S(1,1), -S(1,2),-S(1,3),-S(1,4);...
   S(2,1), -S(2,2),-S(2,3),-S(2,4);...
   S(3,1), -S(3,2),-S(3,3),-S(3,4);...
   S(4,1), -S(4,2),-S(4,3),-S(4,4)];
```

```matlab
Mn=M./S(1,1);
%% Converting to optical convention
Q=[1 0 0 0;0 0 1 0;0 0 0 -1;0 1 0 0]; %Transformation matrix for
optical/Born-Wolf convention
Q1=[1 0 0 0; 0 0 0 1; 0 1 0 0; 0 0 -1 0]; %Defining inverse Q matrix
MnO=Q1*Mn*Q % Presenting Mueller optical normalized matrix
%% Showing normalized Mueller matrix as images (Optical convention)
norm=max(max(ImS00));
h=figure('Name','Optical normalized Mueller
matrix','units','normalized','outerposition',[0 0 1 1]);
h.PaperPositionMode = 'auto'; %for saving the image as it appears on
screen
set(h,'visible','off'); %hide the figure while we are changing its
properties
iptsetpref('ImshowBorder','tight'); %remove unnecessary white space
subplot(4,4,1); imagesc(ImS00/norm); colormap jet;  title('M00'); axis
image; caxis([-1 1]); axis off;
subplot(4,4,2); imagesc(-ImS03/norm); colormap jet;  title('M01'); axis
image; caxis([-1 1]); axis off;
subplot(4,4,3); imagesc(-ImS01/norm); colormap jet;  title('M02'); axis
image; caxis([-1 1]); axis off;
subplot(4,4,4); imagesc(ImS02/norm); colormap jet;  title('M03'); axis
image; caxis([-1 1]); axis off;
subplot(4,4,5); imagesc(ImS30/norm); colormap jet;  title('M10'); axis
image; caxis([-1 1]); axis off;
subplot(4,4,6); imagesc(-ImS33/norm); colormap jet;  title('M11'); axis
image; caxis([-1 1]); axis off;
subplot(4,4,7); imagesc(-ImS31/norm); colormap jet;  title('M12'); axis
image; caxis([-1 1]); axis off;
subplot(4,4,8); imagesc(ImS32/norm); colormap jet;  title('M13'); axis
image; caxis([-1 1]); axis off;
subplot(4,4,9); imagesc(ImS10/norm); colormap jet;  title('M20'); axis
image; caxis([-1 1]); axis off;
subplot(4,4,10); imagesc(-ImS13/norm); colormap jet;  title('M21'); axis
image; caxis([-1 1]); axis off;
subplot(4,4,11); imagesc(-ImS11/norm); colormap jet; title('M22'); axis
image; caxis([-1 1]); axis off;
subplot(4,4,12); imagesc(ImS12/norm); colormap jet; title('M23'); axis
image; caxis([-1 1]); axis off;
subplot(4,4,13); imagesc(-ImS20/norm); colormap jet;  title('M30'); axis
image; caxis([-1 1]); axis off;
subplot(4,4,14); imagesc(ImS23/norm); colormap jet; title('M31'); axis
image; caxis([-1 1]); axis off;
subplot(4,4,15); imagesc(ImS21/norm); colormap jet;  title('M32'); axis
image; caxis([-1 1]); axis off;
subplot(4,4,16); imagesc(-ImS22/norm); colormap jet;  title('M33'); axis
image; caxis([-1 1]); axis off;
% Just to modify figure properties:
f=0;%counter for the number of subfigure;
xant=0; l=0;%initial x and factor shift for subplots
for i=0:3 %two fors for easy labeling each subfigure
    for j=0:3
        l=l+1; %control of shifting of figure
        f=f+1; %updating subfigure counter
        sp_hand1 = subplot(4,4,f); %calling handle of subfigure
```

```matlab
        pos1 = get(sp_hand1, 'Position'); % obtaining the position of
current sub-plot
        new_pos1 = pos1 +[xant 0 0.04 0.04]; %defining new position
        set(sp_hand1, 'Position',new_pos1 ); % setting new position of
current sub - plot
        v = axis; %For the title position
        handle=title(['M',num2str(i), num2str(j)]); %Assigning the title
of the graphic
        set(handle,'Position',[v(2)/2 v(4)*0.12 0]); %Placing the title
        xant=(-new_pos1(3)/2+.003)*l; %defining new x coordinate
    end
    xant=0; l=0; %resetting values for new row
end
%Placing one color bar for all subfigures; taking as reference the
position of the last subfigure.
colorbar('Position', [new_pos1(1)+new_pos1(3)-0.04  new_pos1(2)  0.03
new_pos1(2)+new_pos1(3)*3.78],'fontsize',12)
drawnow
set(h,'visible','on'); %Showing Figure
saveas(h,'Optical Normalized Mueller Matrix.jpg') %Saving to disk
```

C.3. Algorithm to compute the spatial average symmetry (SAS) of an azimuthal beam of light

```matlab
%======================Program info====================================
%Program to compute the Stokes vector in images and numerical values from
%7 images using an unconventional polarized beam of light.
%The program uses 1 image of the unconventionally polarized beam (e.g.
%azimuthal) as a reference to obtain the size of the beam cross section
%(working area). The other 6 images are the corresponding when analyzing
%the beam for horizontal, vertical, +45, -45, R, L polarizations.
%The user specifies the center of the beam to crop the image.
%The program gives the images cropped, the Stokes parameters in images
%and in numerical values.
%Developed by Jacqueline Isamar Muro Ríos as a part of master's thesis at
%CIO, León, Gto. México.
%V1.4 June-7-2017
%V1.5 June-24-2017 A section for scale the images from pi/2 converter is
%added to have equal proportion and size.
%======================================================================
==
%Initialization
clc; close all; clear all;
%% Loading and cropping the images
AzRefg=imread('Reft5.jpg');
AzHg=imread('GT0t5.jpg');
AzVg=imread('GT90t5.jpg');
Az45g=imread('GT45t5.jpg');
Az_45g=imread('GT135t5.jpg');
AzRg=imread('Rt5.jpg');
AzLg=imread('Lt5.jpg');
%% cropping the images by hand
%rad=300; %half the size of the cropped image for MCC (Air)
%rad=474; %Value for MCA (Pi/2), air and lambda/4. This value was
%selected to have the same proportion intensity-image size according to
%the cropped image for MCC (Air).
%rad=496; %Value for MCA (Pi/2) lambda/2 WP. (The beam is bigger when
%passing through the MCA).
%rad=340; %Rad for MCB (Pi) Air.
rad=442; %Rad for MCB (Pi) lambda/4
%rad=371; %Rad for MCB (Pi) lambda/2
[AzRefgc,AzRefc]=ImageCrop2(AzRefg,rad);
[AzHgc,AzHc]=ImageCrop2(AzHg,rad);
[AzVgc,AzVc]=ImageCrop2(AzVg,rad);
[Az45gc,Az45c]=ImageCrop2(Az45g,rad);
[Az_45gc,Az_45c]=ImageCrop2(Az_45g,rad);
[AzRgc,AzRc]=ImageCrop2(AzRg,rad);
[AzLgc,AzLc]=ImageCrop2(AzLg,rad);
%% Scaling images (Optional if their size is different from the ones for
%MCC (Air)
%fact=0.633; %Scale factor for MCA, air and lambda/4 WP. The scale factor
%is computed according to the ratio of the cropped image in air and the
%cropped image to be resized.
%fact=0.6052; %Scale factor for lambda/2 images for MCA (Pi/2)
%fact=0.8825; %Scale factor for MCB(Pi) Air
fact=0.6783; %Scale factor MCB (Pi) lambda/4
%fact=0.8078; %Scale factor MCB (Pi) lambda/2
AzRefgc=imresize(AzRefgc,fact); AzRefc=imresize(AzRefc,fact); %The
process is done for all the cropped images
AzHgc=imresize(AzHgc,fact); AzHc=imresize(AzHc,fact);
AzVgc=imresize(AzVgc,fact); AzVc=imresize(AzVc,fact);
```

```matlab
Az45gc=imresize(Az45gc,fact); Az45c=imresize(Az45c,fact);
Az_45gc=imresize(Az_45gc,fact); Az_45c=imresize(Az_45c,fact);
AzRgc=imresize(AzRgc,fact); AzRc=imresize(AzRc,fact);
AzLgc=imresize(AzLgc,fact); AzLc=imresize(AzLc,fact);
%% Saving cropped images to disk
imwrite(uint8(AzRefc),'AzRefc.jpg','jpg');
imwrite(AzRefgc,'AzRefgc.jpg','jpg');
imwrite(uint8(AzHc),'AzHc.jpg','jpg'); imwrite(AzHgc,'AzHgc.jpg','jpg');
imwrite(uint8(AzVc),'AzVc.jpg','jpg'); imwrite(AzVgc,'AzVgc.jpg','jpg');
imwrite(uint8(Az45c),'Az45c.jpg','jpg');
imwrite(Az45gc,'Az45gc.jpg','jpg');
imwrite(uint8(Az_45c),'Az_45c.jpg','jpg');
imwrite(Az_45gc,'Az_45gc.jpg','jpg');
imwrite(uint8(AzRc),'AzRc.jpg','jpg'); imwrite(AzRgc,'AzRgc.jpg','jpg');
imwrite(uint8(AzLc),'AzLc.jpg','jpg'); imwrite(AzLgc,'AzLgc.jpg','jpg');
%% Presenting cropped images
figure('Name','HAND CUTTED
IMAGES','units','normalized','outerposition',[0 0 1 1]);
subplot(2,3,1); imagesc(AzHc); colormap gray; title('Cropped H image');
axis square %showing the original reference image (azimuthally polarized
beam)
subplot(2,3,4); imagesc(AzVc);colormap gray; title('Cropped V
image');axis square
subplot(2,3,2); imagesc(Az45c);colormap gray; title('Cropped 45°
image');axis square
subplot(2,3,5); imagesc(Az_45c);colormap gray; title('Cropped -45°
image');axis square
subplot(2,3,3); imagesc(AzRc);colormap gray; title('Cropped R
image');axis square
subplot(2,3,6); imagesc(AzLc);colormap gray; title('Cropped L
image');axis square
%% computing the Stokes parameters in images and numbers
S0=double(AzHc)+double(AzVc); norm=max(max(S0));
figure; imagesc(S0/norm); colormap jet; colorbar; title('S0'); axis off;
axis equal; caxis([-1 1]); Sm(1,1)=mean(mean(S0));
set(gca,'units','normalized','position',[0 0.02 0.98 0.93]) %[left bottom
width height]
print('S0','-djpeg','-r0') %to write the figure like a jpg image at
screen resolution
S1=double(AzHc)-double(AzVc); figure; imagesc(S1/norm); colormap jet;
colorbar; title('S1'); axis off; axis equal; caxis([-1 1]);
Sm(2,1)=mean(mean(S1));
set(gca,'units','normalized','position',[0 0.02 0.98 0.93]) %[left bottom
width height]
print('S1','-djpeg','-r0') %to write the figure like a jpg image at
screen resolution
S2=double(Az45c)-double(Az_45c); figure; imagesc(S2/norm); colormap jet;
colorbar; title('S2'); axis off; axis equal; caxis([-1 1]);
Sm(3,1)=mean(mean(S2));
set(gca,'units','normalized','position',[0 0.02 0.98 0.93]) %[left bottom
width height]
print('S2','-djpeg','-r0') %to write the figure like a jpg image at
screen resolution
S3=double(AzRc)-double(AzLc); figure; imagesc(S3/norm); colormap jet;
colorbar; title('S3'); axis off; axis equal; caxis([-1 1]);
Sm(4,1)=mean(mean(S3));
```

```matlab
set(gca,'units','normalized','position',[0 0.02 0.98 0.93]) %[left bottom
width height]
print('S3','-djpeg','-r0') %to write the figure like a jpg image at
screen resolution
% Normalized parameters
Smn=[1; Sm(2,1)/Sm(1,1); Sm(3,1)/Sm(1,1); Sm(4,1)/Sm(1,1)]
```

C.4.   Function to crop an image

```
function [Imgc,GrayImc]=ImageCrop2(Img,rad)
%Function to crop an image
%Entrance parameters:
%-Img=Image to be cropped in rgb format
%-rad= Half the size of the desired region
%By Jacqueline Muro
%V. 1.1 28/June/2017 The size of the cropped image is fixed to 2*rad by
2*rad independently if it gets out of bounds.
f=figure('units','normalized','outerposition',[0 0 1 1]); %for displaying
image at full screen
imagesc(Img);colormap gray; title('Select the center of the beam'); axis
image; %showing image
[a,b] = ginput(1); close(f); % Select a section of the image [col rows]
a=ceil(a); b=ceil(b); % Converting to integer
GrayIm= rgb2gray(Img); %Converting to grayscale
ub=size(GrayIm); %Obtaining upper bounds (size of original image)
lim=[a-rad a+rad b-rad b+rad]; %saving xmin xmax ymin ymax values of the
desired region
[lim2,limO]=OBCheck(ub,lim); %Calling function to check out of bounds
issue
rell=(GrayIm(limO(1),lim2(1))+GrayIm(limO(2),lim2(2))+GrayIm(lim2(3),limO
(3))+GrayIm(lim2(4),limO(4)))/4; %Averaging the intensity in the region
borders
GrayImc=ones(2*rad+1,2*rad+1); GrayImc(:,:)=rell; %Initializing and
uniformizing the minimum intensity (not to abrupt change as if was 0);
GrayImc(lim2(1):lim2(2),lim2(3):lim2(4))=GrayIm(limO(1):limO(2),limO(3):l
imO(4));%Moving data
Imgc=imcrop(Img,[1 1 2*rad 2*rad]); %Initializing color image
Imgc(:,:,:)=0; %Filling with zeros
Imgc(lim2(1):lim2(2),lim2(3):lim2(4),1)=Img(limO(1):limO(2),limO(3):limO(
4),1);%Moving data from red channel
Imgc(lim2(1):lim2(2),lim2(3):lim2(4),2)=Img(limO(1):limO(2),limO(3):limO(
4),2);%Moving data from green channel
Imgc(lim2(1):lim2(2),lim2(3):lim2(4),3)=Img(limO(1):limO(2),limO(3):limO(
4),3);%Moving data from blue channel
```

C.5.   Function to check for out of bounds problems

```matlab
function [lim2,limO]=OBCheck(ub,lim)
%For checking if a desired region is out of bounds of the original image
%Entrance parameters:
%    ub=row vector containing original image size [rows cols]
%    lim=row vector containing original desired bounds [ccmin ccmax crmin
%    crmax]
%Output parameters:
%    lim2=rows vector containing the beginning and end coordinates in
%    columns and row directions. lim2=[rowmin rowmax cmin cmax]
%    limO=rows vector containing the beginning and end coordinates in
%    columns and row directions in the original image. limO=[rowminO
rowmaxO cminO cmaxO]
% By Jacqueline Muro
% V1.0 05/03/2017
bc=lim(1); ec=lim(2); br=lim(3); er=lim(4); % initializing limits of the
bounding pixels original image. bc,ec=beginning and end in columns.
br,er=beginning and end in rows
m=ones(1,4); %m is a row matrix for saving distance out of bounds in all
directions
if (lim(1)<1) %If we are out of bounds in columns origin
    bc=1; %correcting bound
    m(1)=abs(lim(1)); % margin out of bounds
end
if lim(2)>ub(1,2) %If we are out of bounds in columns end
    ec=ub(1,2);%correcting bound
    m(2)=abs(lim(2)-ub(1,2)); % margin out of bounds
end
if lim(3)<1 %If we are out of bounds in rows origin
    br=1;%correcting bound
    m(3)=abs(lim(3)); %margin out of bounds
end
if lim(4)>ub(1,1) %if we are out of bounds in rows end
    er=ub(1,1);
    m(4)=abs(lim(4)-ub(1,1)); %margin out of bounds
end
marc=ceil((m(1)+m(2)-2)/2); %margin in columns to be compensated with 0's
marr=ceil((m(3)+m(4)-2)/2); %margin in rows to be compensated with 0's
lim2=[marr+1,(er-br)+marr+1,marc+1,(ec-bc)+marc+1]; %row vector with the
corrected limits in format (rmin rmax cmin cmax)
limO=[br,er,bc,ec]; %row vector with the corrected limits in the original
image. Format (rmin rmax cmin cmax)
```

References

AGUILAR, E. *Polarimetry employing classical entanglement of light*. Master thesis, Centro de Investigaciones en Óptica, A.C., 2017.

AIELLO, A. and WOERDMAN, J. Linear algebra for mueller calculus. *arXiv:math-ph/0412061v3*, 2006.

ALTECHNA. S-waveplate operation manual. Available at `http://wophotonics.com/wp-content/uploads/2015/09/Operation-Manual-_130701.pdf`.

ANDERSON, Z. Alignment of resonant optical cavities. *Applied Optics*, vol. 23, 2944-2949, 1984.

ATONDO-RUBIO, G., ESPINOSA-LUNA, R. and MENDOZA-SUÁREZ, A. Mueller matrix determination for one-dimensional rough surfaces with a reduced number of measurements. *Optics Communications*, vol. 244, 7-13, 2005. DOI: 10.1016/j.optcom.2004.09.027.

BEIJERSBEGEN, M., ALLEN, L., VAN DER VEEN, H. and WOERDMAN, J. Astigmatic laser mode converters and transfer of orbital angular momentum. *Optics Communications*, vol. 96, 123-132, 1992.

BERESNA, M. and KAZANSKY, P. Space variant polarization converter. Available at `https://www.google.com/patents/US20140153097`. US Patent App. 14/115,300.

COLLET, E. *Polarized Light*. Marcel Dekker, Inc., 1993.

CYWIAK, M. Notes from polarization course, CIO. 2016.

ESPINOSA-LUNA, R., LÓPEZ-MORALES, G., RICO-BOTERO, V. and AGUILAR-FERNÁNDEZ, E. Spatial average symmetry associated to unconventional polarization. *Revista Mexicana de Física*, vol. 63, 205-210, 2017.

ESPINOSA-LUNA, R. and ZHAN, Q. *Polarization and Polarizing Optical Devices, Ch. 9, Handbook of Optical Engineering*. Edited by Daniel Malacara, CRC Press, to be published in 2017.

GOLDSTEIN, D. *Polarized Light*. CRC Press, 2011.

LUDA, M., LAROTONDA, M., PAZ, J. and SCHMIEGELOW, C. Manipulating transverse modes of photons for quantum cryptography. *Physical Review A*, vol. 89, 042325, 2014.

MARCUSE, D. *Light Transmission Optics*. VNR, 1982.

PADGETT, M., ARLT, J. and SIMPSON, N. An experiment to observe the intensity and phase structure of Laguerre-Gaussian laser modes. *Am.J.Phys.*, vol. 64, 77-82, 1996.

SASADA, H. and OKAMOTO, M. Transverse-mode beam splitter of a light beam and its application to quantum cryptography. *Physical Review A*, vol. 68, 012323, 2003.

TÖPPEL, F., AIELLO, A. and MARQUARDT, C. Classical entanglement in polarization metrology. *New Journal of Physics*, vol. 16, 073019, 2014. DOI: 10.1088/1367-2630/16/7/073019.

ZHAN, Q. Cylindrical vector beams: from mathematical concepts to applications. *Advances in Optics and Photonics*, vol. 1,1-57, 2009. DOI: 10.1364/AOP.1.000001.

ZHAN, Q. *Vectorial Optical Fields, Fundamentals and Applications*. World Scientific, 2014.